university of groningen / faculty of science and engineering

Master Research Project Mechanical Engineering

Development and validation of an analytical flow model for the buried Ocean Battery

Author
W.J. Stegenga

Daily supervisor
R.M. Nienhuis

First examiner
Prof. dr. A. Vakis

Second examiner
Drs. W. Prins

August 24, 2021

OCEAN GRAZER

Abstract

This study presents the development and validation of an analytical MATLAB model to aid the design of the buried Ocean Battery based on the efficiency of different pipe configurations. It focuses on the hydrodynamic behaviour and the mechanics that influence the fluid flow through different pipe configurations. It focuses on the pipes that are used to transport water between the rigid and flexible reservoir in the Ocean Battery, and includes a literature study into the determination of minor loss coefficients, the development of the analytical MATLAB model and the validation of the model using computational fluid dynamic simulations in COMSOL. The analytical model is able to calculate losses of simple pipe configurations of the buried Ocean Battery, however, complex pipe configurations cannot be evaluated due to the lack of friction factors for these. One of the main findings of this thesis was that the head loss in the current design of the buried Ocean Battery using the MATLAB model was found to be only 1.4% of the total available hydrostatic head, whereas the head loss using the CFD simulations was only 0.266%. Overall, it is thus found that the current design shows great potential for energy storage, however, the differences can be mainly accounted to the simplicity of the MATLAB model. Besides, COMSOL is also used to perform a CFD analysis for the prototype of the deep water version of the Ocean Battery. The head loss was calculated to be 0.069 m, whereas the average head loss from experiments was found to be 0.064 m. This shows that CFD simulations can predict pipe flow losses and that COMSOL is a viable tool to analyse the losses before experiments are performed. Finally, it can be concluded that for a simple pipe geometry, the MATLAB model is able to quickly calculate the losses, whereas COMSOL provides the user with much more options to analyse pipe flow. Furthermore, experiments need to be conducted to validate the MATLAB and COMSOL results for the current design of the buried Ocean Battery.

Keywords: Energy Storage, buried Ocean Battery, Pipe Flow, CFD, MATLAB, COMSOL, Head Loss, Friction Factor, Efficiency

Contents

1 Introduction

The energy generation from renewable energy (RE) sources is rapidly growing, as the harmful effects of fossil fuels are acknowledged [1, 2]. To reduce greenhouse gas emissions, RE sources such as photovoltaic, wind and hydropower provide a sustainable solution to the ever-increasing energy demands. A major downside is that the supply from these RE sources is fluctuating and not as stable as fossil energy sources [3], and therefore not matches the energy demand from the grid. This intermittent nature originates from environmental factors such as solar irradiance and wind speed [2, 4, 5, 6], and affects the system's reliability. A viable solution is to incorporate an energy storage system to match the fluctuating power supply from REs with the demand from the market [1, 2, 3, 7]. The storage system is charged when the production of energy exceeds the demand and discharges when demands exceed the production to meet the deficit. Figure 1 shows that there exist many storage possibilities nowadays, above and below-ground. These energy storage technologies are categorised by the form of energy stored, generally classified into mechanical, electro-chemical, chemical, electrical, and thermal energy [8]. Among the mechanical storage systems, the pumped hydro storage (PHS) system is the most developed commercial storage technology and makes up about 94% of the world's energy storage capacity in 2020 [5, 8]. It is characterized by its long-life cycle, flexibility and low maintenance cost [9]. In PHS, low-cost electric power in off-peak times is used to pump water from a lower reservoir into a higher reservoir [2, 5, 10], storing energy in the form of gravitational potential energy. During high energy demand, this water is released through turbines to produce power again.

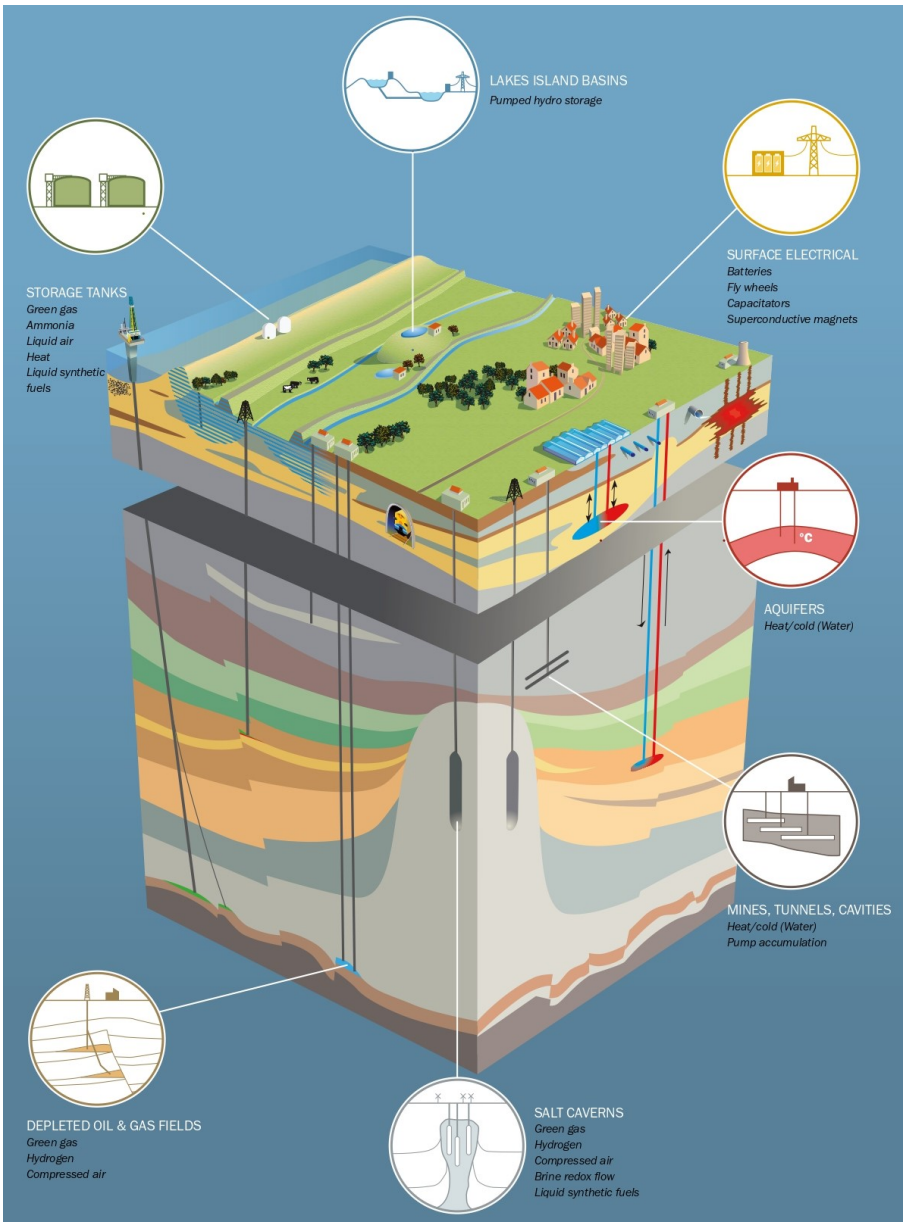

Figure 1: Schematic illustration of energy storage technologies above-ground and below-ground. Image adapted from Ref. [11].

The Ocean Grazer B.V. company uses an innovative approach to this storage technique by the development of the Ocean Battery [12]. The Ocean Battery is able to store energy produced by renewable energy sources such as wind turbines and floating solar farms at sea. When excess RE is routed to the Ocean Battery, it pumps water from the rigid lower reservoir into the flexible bladders located above. Now the energy is stored as potential energy in the form of water under high pressure. When there is a demand for power, water flows back from the flexible bladders to the low pressure rigid reservoirs driving hydro turbines to generate electricity. Currently, there are two designs incorporating this principle as shown in Figure 2, where the deep water design is located entirely on the seabed and in the buried design the rigid reservoir and the hydro turbines are buried into the seabed [13]. The head is the height difference between the surrounding sea water level and water level in the rigid reservoir.

This research project focuses on the transportation of water between the two reservoirs in the Ocean Battery, which is usually done using pipes. The efficiency with which the water gets transported between the reservoirs is not 100% as losses will be present within the pipes. The goal of this project is to give insight into these losses, and by developing a validated MATLAB model the design of the buried Ocean Battery is aided. An EXCEL file serves as input to the flow model, such that it will be user-friendly and versatile. The model remains therefore useful, even when the design of the Ocean Battery changes. It calculates the losses of each pipe section and this analysis gives the performance of a certain pipe configuration. The model is validated using simulations of pipe sections in COMSOL.

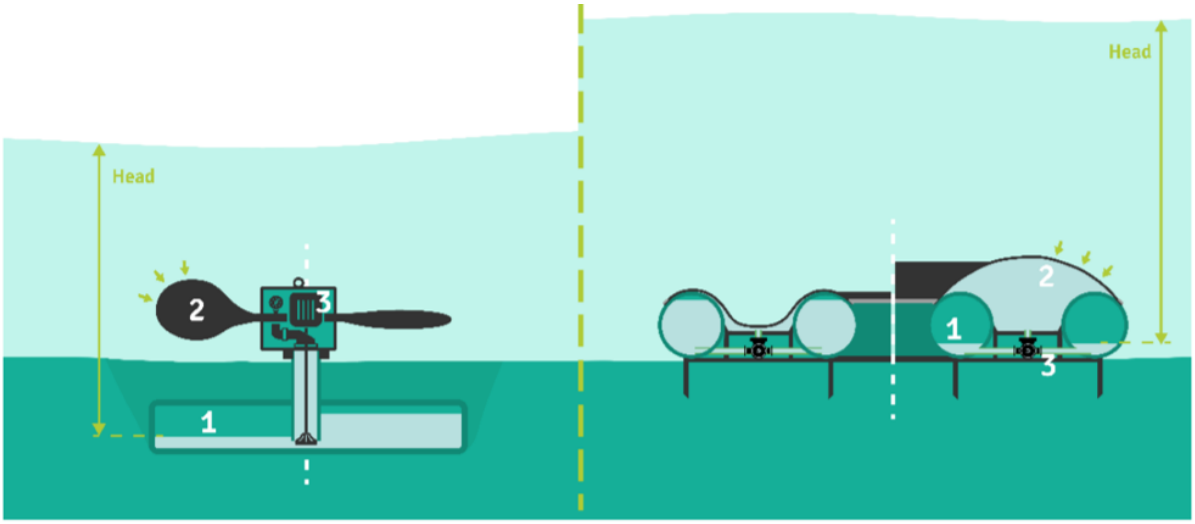

Figure 2: (left) Buried Ocean Battery with a charged state on the left, ready to deliver electricity and discharged state on the right, ready to store any surpluses of energy. (right) Deep water Ocean Battery with a charged state on the right and discharged state on the left. (1) Rigid reservoir (2) Flexible bladder (3) Pumps and turbines.

2 Problem context

Lots of research has been done into the working principle and feasibility of the Ocean Battery. Many studies have been conducted on the deep water design of the Ocean Battery. This has led to the building of a prototype, with which practical tests are being done. The current energy market is, however, mainly focused on shallow water wind farms. The deep water design is not suitable for these wind farms, because it is deployed directly on the seabed and the storage capacity is directly proportional to the hydrostatic head or deployment depth. Therefore, the maximum energy storage capacity remains rather low.

The shallow water or buried Ocean Battery is currently in its design phase. This project focuses on the hydrodynamic behaviour and the mechanics that influence the fluid flow through different pipe configurations of this version of the Ocean Battery as these are not yet studied in detail. Previous research [3, 7, 14] has covered losses in pipe configurations of the deep water version and the prototype, as discussed in Section 3. The unavoidable losses that are present within the pipes therefore still need to be analysed and if necessary, changes can be made to the initial design. It is therefore not yet possible to make an accurate estimation of the efficiency of different pipe configurations.

2.1 Stakeholders

- The problem owner of this project is **Marijn van Rooij**, who is the chief technical officer of the Ocean Grazer BV. The goal of Marijn is to develop the Ocean Battery using the outcome of academic studies. He takes an interest in the development of the buried version of the Ocean Battery, such that in the end a sellable product is created.
- **Prof. dr. Antonis Vakis** is another stakeholder, which is also the academic supervisor for this project. He is mainly focused on the technical side of the Ocean Battery and ensures that this project is of sufficient academic quality.
- **Drs. Wout Prins** is the inventor of the Ocean Grazer and manages the projects done by students and is, therefore, a stakeholder in this research. Besides, he is also supervisor of this project.

2.2 Problem definition

Based on the problem context and the stakeholders, it is concluded that the Ocean Grazer currently does not possess the knowledge to say with confidence what the effects of different pipe configurations are on the efficiency of the buried version of the Ocean Battery. M. Been [15] has initiated a model that describes and predicts the mechanics influencing the losses in each part of the Ocean Battery. This is, however, not yet enough to make an accurate estimation of the total losses in the current design. Information about losses in pipes and junctions is used from previous research. From this, we can formulate the following problem statement:

The Ocean Grazer B.V. lacks knowledge about the effects of different pipe configurations on the efficiency of the buried Ocean Battery.

2.3 Research Goal

The research scope of this project includes the pipes that are used within the buried Ocean Battery. The initial pipe configuration of the current design will be discussed, and in this research, a model is developed in which different pipe configurations can be analysed. The model gives an overview which parts have a large influence on the efficiency. At the end of this research project, a validated MATLAB model is presented that provides a basis to analyse different pipe configurations for the buried Ocean Battery and insights into the round trip efficiency are provided. The model can then be used to design a pipe system with high efficiency, or the design of the buried Ocean Battery can be modified according to the results from the model. Also, the working of the model is validated using computational fluid dynamics (CFD) simulations of pipe sections within COMSOL. The research goal of this project is therefore defined as follows:

"Developing a validated model that can aid the design of the buried Ocean Battery based on the efficiency of different pipe configurations."

This model is created using a set of equations in MATLAB, in which multiple parameters can be varied, such that different pipe configurations can be analysed. The input parameters are explained in Section 8.2. This is especially helpful when the design of the buried Ocean Battery changes over time, as the values of these parameters can be changed, such that the model still provides useful information.

2.4 Research questions

The research goal is achieved by answering the following research questions:

1. How to model fluid flow and losses in pipes?

   The mathematical model is based on a set of equations that calculates the major and minor losses, fluid flow rate and the Reynolds number, as explained in Sections 5 and 6. The model will be expanding upon two previous models made by J. Bromlewe [7] and M. Been [15].

2. To what extent are the major and minor loss coefficients comparable between the mathematical model, literature and simulations? Which mechanics are of influence on the major and minor losses?

   First, an extensive literature study into the available minor and major loss coefficients is given in Section 6 as no unambiguous values are given in previous research. A comparison of the results from the model, simulations and literature are given throughout this report. The mechanics influencing the losses are first explained in Section 5 and are further studied in Section 10.

3. What are the parameters that will affect the behaviour of the buried Ocean Battery, which can be changed in the MATLAB model?

   The mathematical model uses a set of parameters as input, which are discussed in Section 8. Different pipe configurations can be analysed by changing their values. The model includes the pipes between the rigid and flexible reservoirs and uses flow rates of the pumps and turbines for the charging and discharging mode, respectively, which are discussed in Section 7.

4. Which elements of the model require validation by using flow simulation software?

   Theory about how CFD in COMSOL *models fluid flow through pipes is given in Section 9, and the actual analysis of pipe sections is presented in Section 10.*

5. To what extent does the interaction between pipe junctions influence the efficiency of fluid transport through pipes?

   Analyses to if and when pipe junctions, which are placed close to each other, will be of influence on each other. Can these pipe junctions be treated separately or not? Study the separation distance for which they are treated separately. Two pipe bends that are placed close to each other are studied in Section 10.4.

6. How does the current conception of the losses in the Ocean Battery design compare to the outcomes of the CFD results in this research?

   It is expected that the losses in the current design of the buried Ocean Battery are low. The MATLAB *model and* COMSOL *simulations are used to investigate this expectation. The results are discussed in Section 11.*

3 Previous research

In this section, previous research performed by students on the topic of losses in pipe systems of the Ocean Battery is discussed.

3.1 S. van Rijn

Stijn van Rijn created a model to calculate the performance in terms of efficiency and capacity of the deep water Ocean Battery prototype. The research thesis contains information about major and minor losses in pipes, which is expanded upon in this work. In the paper, a model in EXCEL is proposed in which various parameters are varied to analyse the major and minor losses and finally an indication of the charging and discharging efficiency is given. Suggestions to validate the calculations in the model via experiments are also given.

3.2 J. Bromlewe

Jimme Bromlewe created a MATLAB model to study the flow and efficiency of the deep water Ocean Battery prototype. The proposed model calculates the efficiency of the prototype and models the system behaviour in the charging and discharging process. It recalculates the values in the model at a certain time step for these processes. The model, therefore, takes a substantial amount of computational time to run. This model is expanded upon in this work, however, in a way that the losses are calculated much quicker for which the volumes of the reservoirs are left out. The paper contains theory regarding the filling of the reservoirs and energy conversion of components (including efficiencies). Besides, the major and minor losses are also studied, of which this theory is equal to that mentioned in the thesis of van Rijn [14]. The model is then validated by doing measurements with a test setup of the prototype, which were found to be close to the analytical model.

3.3 M. Been

Margriet Been studied three design concepts of the Ocean Battery, namely the deep water version, the buried version and the deep water prototype. In the paper, a general analysis is given in which the power output, flow velocity, Reynolds and Froude number have been analysed as a function of the flow rate of the pump-turbine and the diameter of the intake pipe. An analytical analysis, using MATLAB, and a numerical analysis, using COMSOL, have been performed to predict the pressure loss in simple pipe sections. This approach is adopted in this thesis for more complex pipe configurations. Also, the critical submergence and vortex forming are studied.

3.4 Added value of this project

In this project, a MATLAB model is developed in which a certain pipe configuration of the buried Ocean Battery can quickly be analysed. The computation time should be low and in the order of tens of seconds at maximum. The model will be created in such a way that it can be modified afterwards to also incorporate the filling and emptying of the reservoirs, as previously done by J. Bromlewe [7].

Furthermore, the model needs to be as inclusive as possible. It should not contain too many approximations and assumptions. It includes every pipe section beginning at the rigid reservoir, where the water enters the pipes and ends at the inlet of the flexible reservoir. The model analyses the losses either in charging or discharging mode.

After the model is finalised in MATLAB, it will be validated using simulations in COMSOL. First, some simple pipe sections such as a bend with varying bend radius are studied. After that, the interaction of junctions is studied by simulating the fluid flow through two 90° bends separated by some distance. It then becomes clear if the results from simulations match with the theory. Finally, the pipes of the current design of the buried Ocean Battery are simulated.

4 System Description Buried Ocean Battery

The design of the buried Ocean Battery is not yet finalised, however, the current design (August 2021) is discussed in this section. This design is adopted from Marijn van Rooij and Wout Prins, both stakeholders of this project. Before the design itself is shown, first, the operation of the Ocean Battery is discussed.

4.1 System operation

Figure 3 gives a schematic overview of the buried Ocean Battery operation principle when it is either charging (energy supply) or discharging (energy demand). When a renewable energy source has a higher energy production than there is demand, the surplus energy is fed into the transformer of the Ocean Battery. This drives a motor, which is connected to a pump, which pumps water from the lower rigid reservoir into the upper flexible reservoir. The rigid reservoir, which is the low pressure side of the battery, is buried into the seabed and is constantly at atmospheric pressure as the umbilical cord transports air between this reservoir and the water surface [14]. Renewable energy is stored as potential energy in the form of water under high pressure in the flexible reservoir [6], which means that there is a pressure difference between both reservoirs. The hydrostatic pressure depends linearly on the sea depth, thus on the available hydrostatic head. The height difference between both reservoirs increases the pressure difference even more and this height difference is generally termed by head.

When there is a lower production of energy than there is demand, the energy stored in the Ocean Battery is used. A valve is opened after which water from the flexible reservoir flows back to the rigid reservoir via hydro turbines, which then recovers part of the energy from the fluid.

The storing of energy using the Ocean Battery is not 100% efficient but the roundtrip efficiency is estimated to be as high as 80% [6]. The roundtrip efficiency of the system is influenced by the efficiency of the transformer, motor, pump, turbine, generator and pipes. Also, start-up and shut-down effects play a role in determining its efficiency.

The design of the buried Ocean Battery is not yet finalised, but recent research [10, 16, 17, 18] has pointed out that a pump-turbine can replace a separate pump and turbine, maintaining a good efficiency in both charging and discharging modes. The pump-turbine saves on initial investment costs but has an expected lower efficiency than a separate pump and turbine.

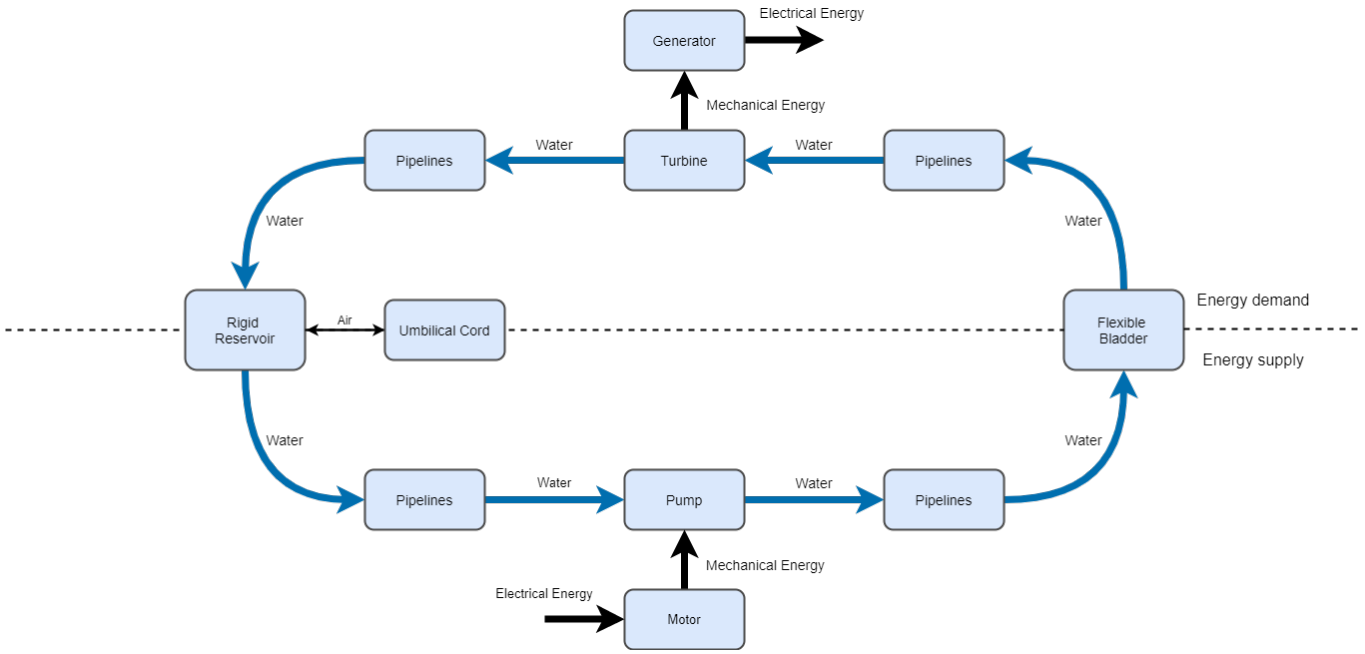

Figure 3: System operation of the buried Ocean Battery in either the charging state (energy supply) or discharging state (energy demand). The flows of either electrical or mechanical energy, water or air are denoted. The separate pump and turbine in this figure can be combined into a pump-turbine unit and the pipes can be used for both charging and discharging mode. The umbilical cord transports air between the rigid reservoirs and the water surface to keep the rigid reservoir at atmospheric pressure.

4.2 Current design

Figure 4 depicts a schematic overview of the current design of the buried Ocean Battery. The rigid reservoir (1) is buried in the seabed to increase the pressure difference between the flexible and rigid reservoir. The pump-turbines (2) are used to pump the water to the flexible bladder (3) and also serves as turbine. The umbilical cord is not shown in the figure. A collection container below the pump-turbines (4) is always filled with water and collects water from multiple rigid reservoirs. Figure 4 also shows the trajectory of the inner working fluid in charging mode with white triangles, where it flows from the rigid reservoir to the flexible reservoir by operating the pump. The trajectory in the discharging mode is shown by the black triangles.

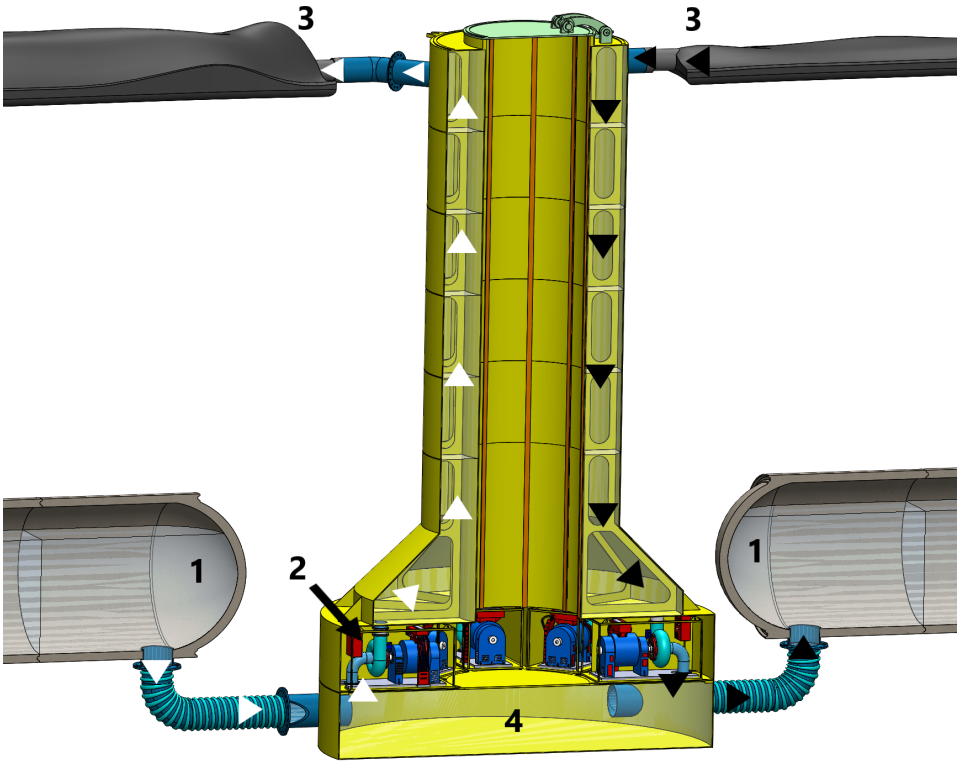

Figure 4: Schematic overview of the current design of the buried Ocean Battery. 1: Rigid Reservoir. 2: Pump-turbines. 3: Flexible Reservoir. 4: Collection container between the rigid reservoir and the pump-turbines. The trajectory of the working fluid is shown in charging mode (white triangles) and discharging mode (black triangles).

Based on this design, it is expected by the members of the Ocean Grazer and their researchers that the pressure losses in both charging and discharging modes are low. As the pipe diameters are very large, the fluid velocity remains low in all pipes. A low velocity means low frictional losses between the working fluid and the pipe walls. Only the pipes close to the pump-turbines are rather narrow and therefore the velocity is locally higher. These pipes are, however, kept short to mitigate this. This reasoning is based on expectations and conducted research. However, no attempt was made to simulate, measure or model the pressure losses for this design. The best way to verify the expectations is to conduct full-size experiments, however, it is impossible to do experiments on a full-size model of this design, as the design continually changes and the analysis should be reusable for every design iteration. Therefore, this study presents general mechanics of losses in pipe flow and an analysis of the roundtrip efficiency of the current design.

4.2.1 Rigid Reservoir

The rigid reservoir is a non-deformable reservoir buried into the seabed that stores water. When the system is charging, water from this reservoir is pumped to the flexible reservoir and this process is reversed when the system is discharging. The structures are connected to the collection container, located below the pump-turbines. There is also a connection for the umbilical cord, such that the reservoir stays at atmospheric pressure.

4.2.2 Flexible Bladder

The flexible bladder is a reservoir that is filled with water from the rigid reservoirs when energy needs to be stored. The bladder deforms easily when water is pumped in and it is constantly under hydrostatic pressure from the surrounding

seawater. The bladder makes sure that the working fluid inside the Ocean Battery cannot mix with the surrounding seawater, making it a closed system. The water stored in the flexible bladder has significantly more energy than the water in the rigid reservoir due to the height difference between both reservoirs and the pressure increase mentioned before [18]. It is connected to a large vertical shaft, which is always filled with water, which is connected to the pump-turbines.

4.2.3 Pump and motor

When the system is charging, a motor uses the electricity from a renewable energy source to power the pump, such that water is pumped from the rigid reservoir to the flexible bladder. The fluid is thereby elevated and also experiences hydrostatic pressure from the surrounding seawater. This process requires a certain amount of work [$\mathrm{N\,m^{-1}}$], which is its weight [N] times the height it is lifted [m] [19]. The energy needed for this process is expressed in units of [m], which is equal to the elevation gain. This is called the elevation or potential head.

It is assumed that the buried Ocean Battery as depicted in Figure 4 consists of eight pump-turbines, each with a power of 200 kW. Previous research by Pasqualini and Masclans [16, 18] has shown that for a system with a minimum head of 35 m and a power of 200 kW per pump-turbine, a Francis reversible pump-turbine is an appropriate choice.

4.2.4 Turbine and generator

Multiple Francis pump-turbines will be used in the buried Ocean Battery to convert kinetic energy into electrical energy. If the turbine's efficiency increases, it can extract more energy from the working fluid, increasing the roundtrip efficiency of the Ocean Battery. The pump-turbine works either as a pump or turbine depending on the rotation direction. The Francis turbine is a reaction turbine that uses a snail-shell shaped tube to direct the water around the rotor of the turbine. Figure 5 shows a schematic overview of a Francis turbine. The snail-shell tube decreases in size around the runner, such that the speed of the water is maintained. Guide vanes are used to direct the water onto the blades, where a low and high pressure side are formed when water flows over it, which results in a reaction force that causes the runner to spin. The water enters the turbine radially via the snail-shell tube but leaves the turbine axially. When it leaves the turbine, it hits the bucket shape blade at the outlet. Additionally to the reaction force, an impulse force is produced, contributing to the motion of the runner. In this way, high efficiencies can be obtained.

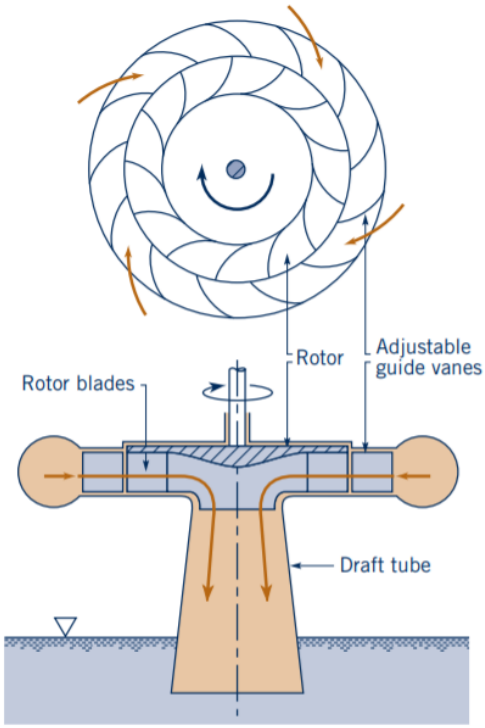

Figure 5: Schematic overview of a Francis turbine, where water enters radially and leaves axially. Figure adapted from Ref. [20].

5 Theory: Pipe Flow and Losses

In this section, general theory about fluid flow and pipe losses, classified as major and minor losses, are explained, which are used in the analytical MATLAB model.

5.1 Classification of flow

In general, fluid flow is classified as laminar, turbulent or critical and the type of flow determines which principles are applicable. In laminar flow, the fluid moves in laminar layers, whereas in turbulent flow, the fluid flows faster and this is accompanied by eddies and disturbances in the fluid [21]. A major difference between laminar and turbulent flow is the much greater energy loss in turbulent flow due to these disturbances [22]. The different flow types are mathematically defined by the Reynolds number, which is calculated by [21, 22, 23]:

$$Re = \frac{\rho v D}{\mu} = \frac{v D}{\nu}, \tag{1}$$

where ρ is the mass density of the liquid, which is $998.2\,\mathrm{kg\,m^{-3}}$ at room temperature (20 °C) [20], v the velocity of the fluid $[\mathrm{m\,s^{-1}}]$, D the pipe diameter $[m]$, μ the dynamic viscosity of the fluid with a value of $1 \times 10^{-3}\,\mathrm{Pa\,s}$ at room temperature and ν the kinematic viscosity of the fluid with a value of $1 \times 10^{-6}\,\mathrm{m^2\,s^{-1}}$ at room temperature [20]. The Reynolds number involves the definition of the kinematic and dynamic viscosity of the fluid. In general, viscosity is the resistance of a fluid to flow [24]. The kinematic viscosity is a measure of the rate at which momentum is transferred through the fluid, and the dynamic viscosity is a measure of the ratio of the stress on a region of a fluid to the rate of change of strain it undergoes, which is the kinematic viscosity multiplied by the density of the fluid, given by [23, 24]:

$$\mu = \nu\rho. \tag{2}$$

The flow types can then be classified according to:

$$\text{Laminar flow: } \mathrm{Re} \leq 2000$$

$$\text{Critical flow: } 2000 < \mathrm{Re} \leq 4000$$

$$\text{Turbulent flow: } \mathrm{Re} > 4000.$$

Generally, critical flow is avoided as it behaves differently than the other flow regimes and equations and principles for laminar nor turbulent flow apply to this flow regime. For the flow to stay either in the laminar or turbulent regime, there are some restrictions based on Equation 1. The fluid velocity and pipe diameter should be kept within a range of values for a particular fluid at a certain temperature. The velocity v of the fluid in a pipe is defined as:

$$v = \frac{Q}{A} = \frac{Q}{0.25\pi D^2}, \tag{3}$$

where Q is defined as the flow rate $[\mathrm{m^3\,s^{-1}}]$ and A the cross-sectional area of the pipe $[\mathrm{m^2}]$. From Equation 3 it becomes clear that the fluid velocity is inversely proportional to the diameter squared.

5.2 Conservation equations

5.2.1 Continuity

The continuity equation, shown in Equation 4, states that there is as much fluid flowing out of a pipe system as there is flowing into [19]. This is under the assumption that mass is conserved and that no fluid is stored in or released from the system. This means that the inlet flow rate is equal to the outlet flow rate, under the assumption that the mass density of the fluid ρ does not change from the inlet to the outlet. The flow rate Q is then calculated by multiplying the pipe cross-sectional area A with the fluid velocity v, see Equation 3.

$$(\rho A v)_{inlet} = (\rho A v)_{outlet} \tag{4}$$

5.2.2 Conservation of energy

The basic principle of the law of conservation of energy is expressed by the Bernoulli equation [21, 22]. The total energy of a fluid at any point in the pipe is calculated by taking into account its pressure, velocity and elevation combined with losses [19, 20, 21, 22, 23]. When a fluid flows through a pipe from point 1 to point 2, the Bernoulli equation is stated as:

$$Z_1 + \frac{P_1}{\rho g} + \frac{V_1^2}{2g} = Z_2 + \frac{P_2}{\rho g} + \frac{V_2^2}{2g} + h_L, \tag{5}$$

where the elevation of point 1 is Z_1 and the elevation of point 2 Z_2 above some common level, as depicted in Figure 6. The pressure at point 1 is P_1 and at point 2 P_2. The flow velocities at points 1 and 2 are represented by V_1 and V_2, respectively. If the pipe diameter is equal at point 1 and 2, and the inlet and outlet flow rate are equal from Equation 4, V_1 and V_2 will be equal. In Equation 5, g is the gravitational acceleration and h_L represents the total head loss [m] between points 1 and 2, which is determined by rewriting Equation 5 into:

$$h_L = Z_1 + \frac{P_1}{\rho g} + \frac{V_1^2}{2g} - Z_2 - \frac{P_2}{\rho g} - \frac{V_2^2}{2g}. \tag{6}$$

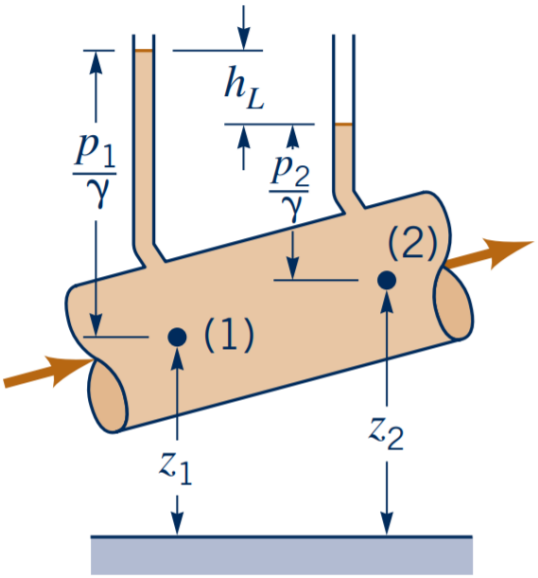

Figure 6: Schematic overview of Bernoulli's equation with the pressures at point 1 and 2, height variation Z and head loss h_L. Here, γ equals ρg. Figure adapted from Ref. [20].

The total head loss in the pipes is divided into losses due to friction in straight sections (major losses or $h_{L,maj}$) and losses at pipe junctions, such as entrances, bends, enlargements, contractions and tees, which are called minor losses ($h_{L,min}$). The head loss is a loss of useful mechanical energy by conversion of this energy into heat energy [19].

$$h_L = \sum h_{L,maj} + \sum h_{L,min} \tag{7}$$

5.3 Major losses

Effort is required to cause a fluid to flow through a pipe because there is relative motion between two bodies in contact which result in frictional resistance [19]. The Darcy-Weisbach equation is used to calculate the major head loss in pipes [21, 22, 23, 24, 25]:

$$h_{L,maj} = f\frac{L}{D}\frac{v^2}{2g} = K_{maj}\frac{v^2}{2g}, \tag{8}$$

where $h_{L,maj}$ is the frictional or major head loss $[m]$, f the Darcy friction factor [-], L the length of the pipe $[m]$, K_{maj} the major loss friction factor and the other symbols are the same as given before. When a fluid flows through a pipe of constant diameter, with a constant flow rate, and taking into account the height difference between two points, the head loss between those points results in a decrease in pressure. The head loss can therefore be converted to a pressure loss in Pa using:

$$p = \rho g h_L, \tag{9}$$

where p denotes the pressure loss $[Pa]$ and h_L the head loss $[m]$ from Equation 8.

5.3.1 Laminar flow

For laminar flow, the friction factor is given by f_{lam}, which only depends on the Reynolds number and has been determined by Hagen-Posseuille [21, 22, 23, 24, 25]:

$$f_{lam} = \frac{64}{Re} \tag{10}$$

5.3.2 Critical flow

For critical flow, the friction factor can have large uncertainties and is therefore essentially indeterminate. This flow type should therefore be avoided as much as possible, such that the equations for laminar or turbulent flow can be used instead. If a pipe were to be designed for flow in this range, the only safe procedure would be to assume that the flow is turbulent [22].

5.3.3 Turbulent flow

For turbulent flow, the friction factor is given by f_{turb}. The determination of this turbulent friction factor is not as straightforward as for laminar flow. It is a non-dimensional number that depends on the absolute roughness of the pipe ϵ, the pipe diameter D and the Reynolds number via the Colebrook-White equation [21, 22, 23, 24, 25]:

$$\frac{1}{\sqrt{f_{turb}}} = -2log_{10}\left(\frac{\epsilon}{3.7D} + \frac{2.51}{Re\sqrt{f_{turb}}}\right). \tag{11}$$

As can be seen from Equation 11, f_{turb} appears on both sides of the equation and can therefore not be determined directly. Figure 7 shows a graphical representation of the friction factor for all flow regimes, where it is plotted against the Reynolds number at various values of the relative roughness ϵ/D of a pipe. Section 5.4 provides more information about surface roughness. Here the straight line in the laminar flow regime corresponds to Equation 10 and in the turbulent regime, Equation 11 is plotted.

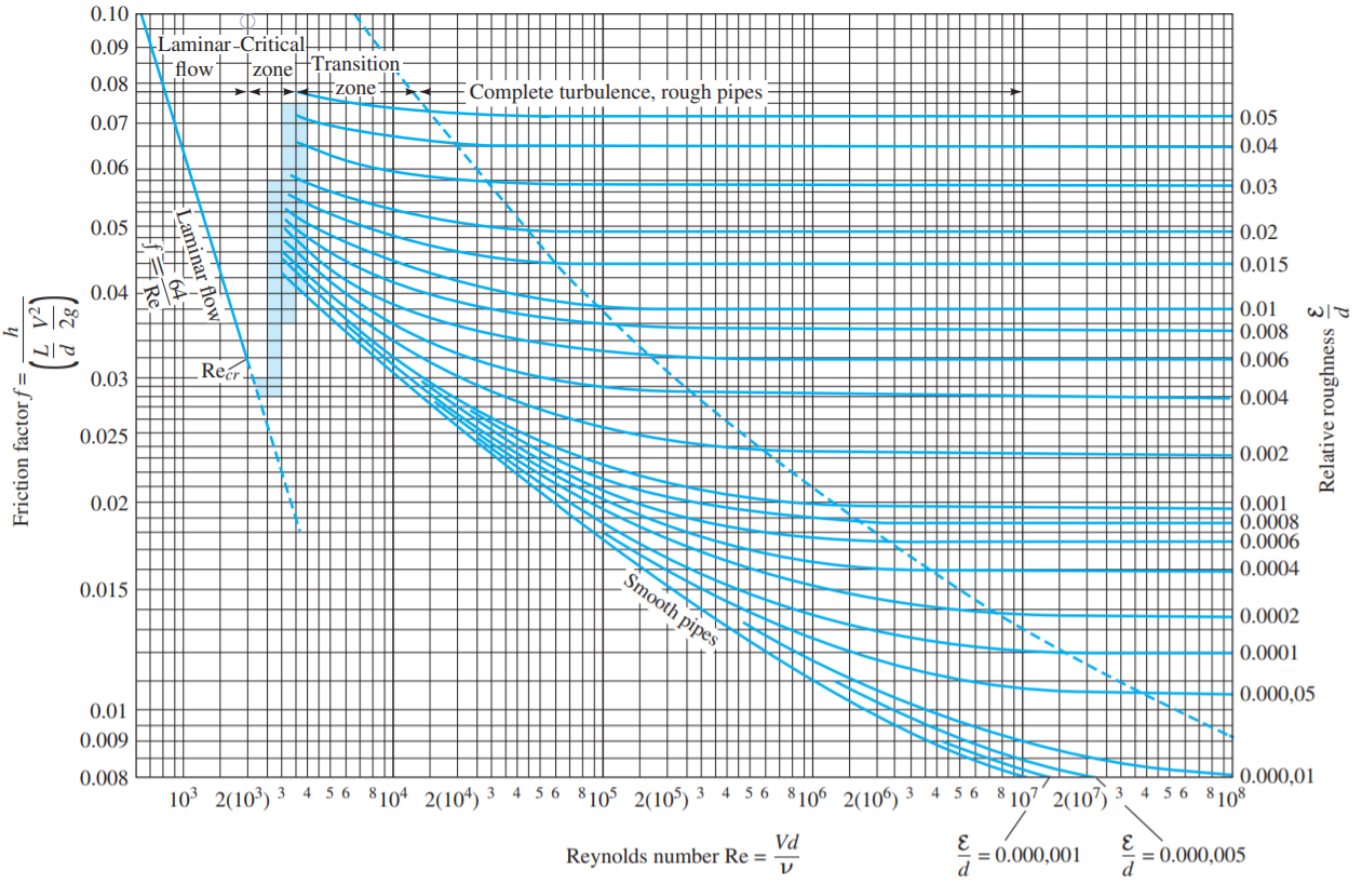

Figure 7: Moody chart for pipe friction with smooth and rough walls. This chart is identical to Equation 10 for laminar flow and to Equation 11 for turbulent flow. Figure adapted from Ref. [23].

Moody [19, 25, 26] has found an approximation to Equation 11 in the transitional and turbulent flow regimes:

$$f_{turb} = 0.0055\left[1 + \left(2 \times 10^4 \frac{\epsilon}{D} + \frac{10^6}{Re}\right)^{1/3}\right]. \tag{12}$$

Note that the transitional flow regime lies between critical and turbulent flow, as shown in Figure 7. Moody noted that the equation agrees with the Colebrook–White equation for the friction factor f within an error of ±5% for Reynolds

number in the range from 4000 - 1×10^7, and for values of the relative roughness ϵ/D up to 0.01 or for values of f up to 0.05 [19].

Another approximation to Equation 11 is made by Haaland [19, 27], as shown in Equation 13. It has relatively good accuracy with an error less than 1.2% for Reynolds numbers in the range of 4000 - 1×10^8 and relative roughness in the range of 1×10^{-6} - 0.05. It is recommended for practical use as an explicit alternative to the Colebrook-White equation [19].

$$f_{turb} = \left\{ -1.8 log_{10} \left[\left(\frac{\epsilon}{3.7D} \right)^{1.11} + \frac{6.9}{Re} \right] \right\}^{-2}. \tag{13}$$

Serghide provides another, explicit, approximation of the solution of the Colebrook-White equation. It is highly accurate over a wider range of values for both surface roughness and Reynolds number than mentioned for the Haaland equation [28]. This method will result in errors of less than 0.003% for Reynolds numbers in the range of 4000 - 1×10^{10} and relative roughness in the range of 1×10^{-7} – 1. Serghide's approximation is defined by the following equations [28], which are valid in the laminar and turbulent flow regime:

$$A = -2 log_{10} \left(\frac{\epsilon}{3.7D} + \frac{12}{Re} \right) \tag{14}$$

$$B = -2 log_{10} \left(\frac{\epsilon}{3.7D} + \frac{2.51A}{Re} \right) \tag{15}$$

$$C = -2 log_{10} \left(\frac{\epsilon}{3.7D} + \frac{2.51B}{Re} \right) \tag{16}$$

$$f = \left(A - \frac{(B-A)^2}{C - 2B + A} \right)^{-2}. \tag{17}$$

The Serghide approximation provides a very good explicit approximation for the Darcy friction factor and is therefore the most appropriate approximation. It is suitable for the mathematical model that is developed in this project as it is explicit and therefore does not require iterations [28]. The error that is present in this approximation is likely to be many orders of magnitude smaller than the error induced in other sources such as the uncertainty in pipe roughness.

5.4 Surface roughness

The major losses for laminar and turbulent flow both depend on the Darcy friction factor, which in turn depends on the Reynolds number and the surface roughness. The surface roughness is defined as irregularities in the surface texture of the pipe inner wall [19]. The degree of roughness is a function of the pipe material, its manufacturing process, and the environment to which it has been exposed. The smoother the surface, the lower the surface roughness, the easier it is for a fluid to flow through and the lower the losses. There are lookup tables available, which give an estimation of the roughness of the pipe material. These are provided by White (Table 6.1 therein) [23], King (Table 6.1 therein) [22], Menon (Table 4.1 therein) [21] and Rennels (Table 8.1 therein) [19]. In Comsol, an equivalent sand roughness height is used to specify the roughness of the walls, which was introduced by J. Nikuradse [29]. These values are mentioned in the CFD Users Guide (Table 3-4 therein) [30]. The surface roughnesses of some typical pipe materials are tabulated in Table 14, where the values provided by White, Menon, Rennels and the CFD Users Guide show many similarities.

5.5 Minor losses

When additional turbulence is present in a fluid due to the pipe shape, the energy that resides in the turbulence is usually not recovered as mechanical energy and is lost as heat [19]. These losses are classified as minor losses, however, minor does not indicate that these losses always will be low. These losses are calculated in a similar way as major losses, where the equation for minor loss of a junction is expressed as:

$$h_{L,min} = K_{min} \frac{v^2}{2g}, \tag{18}$$

where K_{min} denotes the loss coefficient or minor loss friction factor for that junction. This factor is different for every junction in a pipe system.

Minor losses in pipe junctions have been covered by previous theses [3, 7, 14, 15], but a general agreement of a K-value or head loss equation for a specific junction remains unclear. In the next sections, a short description of several junctions is given, after which a table is provided with an extensive list of ways to calculate the head loss h or the K-value for different pipe junctions.

5.5.1 Enlargement and contraction

A pipe can be expanded or reduced suddenly or gradually, as shown in Figure 8. In a sudden contraction, the flow accelerates towards the pipe axis. This high velocity causes the flow to contract and separate from the wall, as shown in Figure 8a [19]. The vena contracta is the point where the flow has a minimum cross-sectional area. After this point, the flow decelerates and reattaches to the wall. Rounding, tapering, or beveling the entrance section reduces the high radially inward velocity and substantially reduces the head loss, of which a conical contraction is shown in Figure 8c [19].

When a fluid flows through an enlargement, there is an increase in static pressure at the expense of a drop in kinetic energy [19]. If this happens very sudden, the velocity decreases abruptly, causing turbulence and, hence, energy loss [31]. In the expanded section, a core forms, which gradually spreads out. As the fluid is forced to change direction at the enlargement, eddies are produced. These eddies interfere with the main flow and cause fluctuations in pressure and velocity, which results in head loss. The eddies are situated in a recirculation region, as shown in Figure 8b [19]. The eddies gradually disappear and the core expands, till it attaches to the wall. This effect can be mitigated using a conical enlargement, also called a diffuser, of which the geometry is shown in Figure 8d. Here, the stall region and core are not shown. A diffuser converts the kinetic energy of the flow into static pressure with minimum head or pressure loss by increasing the cross-sectional area in a gradual manner, usually with a cone angle θ. Generally, the ratio of the smaller diameter pipe D_1 over the larger diameter pipe D_2 is denoted by β.

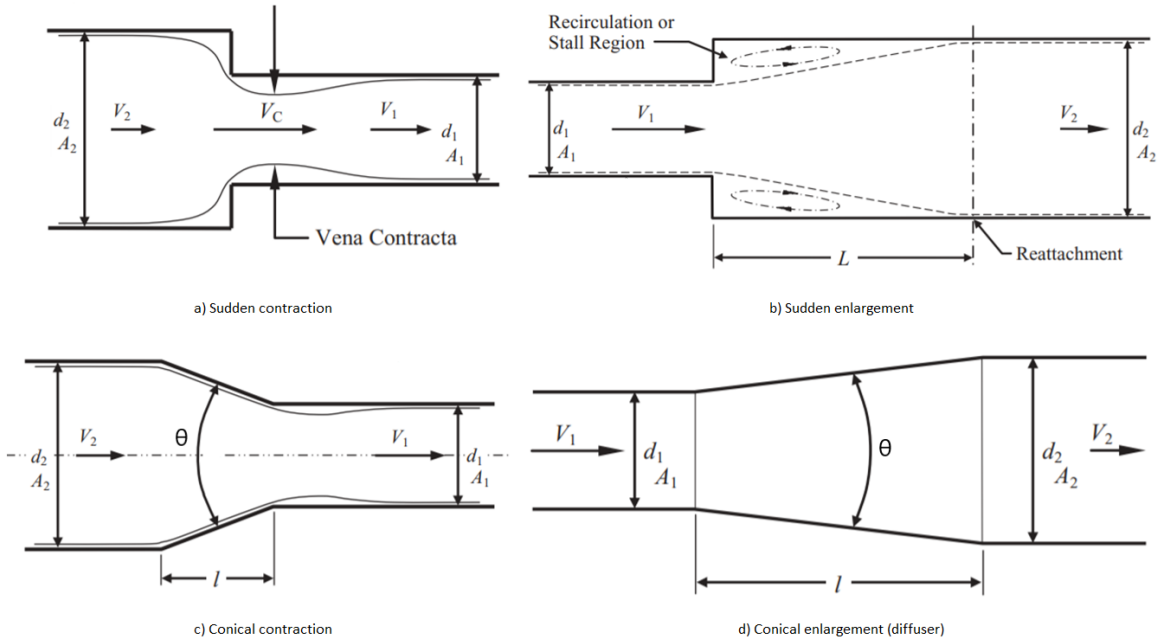

Figure 8: Sudden and gradual enlargements and contractions. d_1 is the diameter of the smaller pipe and d_2 is the diameter of the larger pipe, in accordance with Table 1. Figures adapted and modified from Ref. [19].

5.5.2 Inlet and exit

When a fluid flows from a large tank or reservoir into a pipe, it encounters an inlet. Figure 9 shows that there are several inlet types available. Any rounding or chamfering of the inlet makes the sudden contraction into the pipe smoother and results in a lower loss. Extending the pipe into the reservoir makes it more difficult for the fluid to flow into the pipe, increasing the loss. For an inlet, the flow direction is from left to right but is opposite in the case of a pipe exit.

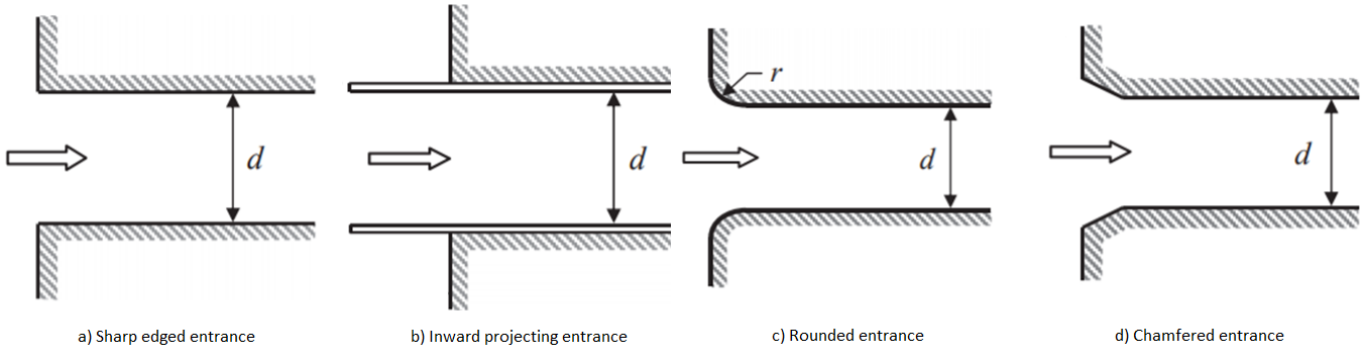

Figure 9: Four types of inlets, used to transport fluid from a reservoir (left side of each figure) into a pipe (right side of each figure). The loss factors corresponding to each inlet type are denoted in Table 1. Figures adapted and modified from Ref. [19].

5.5.3 Bends

When a fluid flows through a bend, its flow direction is altered, depending on the bend angle θ_b, as shown in Figure 10. Each bend has a certain radius of the centerline of the bend R, also called radius of curvature, and radius of the cross-sectional area of the pipe r, which is half the pipe diameter d. Losses in pipe bends are generally composed of three components. One is the surface friction with the pipe walls, as discussed in Section 5.3. This effect is dominant for bends with a large radius of curvature. A second component is due to the secondary flow, superimposed on the primary flow through the pipe due to a combination of centrifugal forces and frictional resistance of the pipe walls [19]. This topic is covered in more detail in Section 10.4.3. The third component is due to the separation of the flow from the inner and outer walls of the pipe. This effect is dominant for bends with a small radius of curvature. A well-cited paper by Ito [32] provides a benchmark for pressure losses within pipe bends. Several authors have reproduced these results with experimental data.

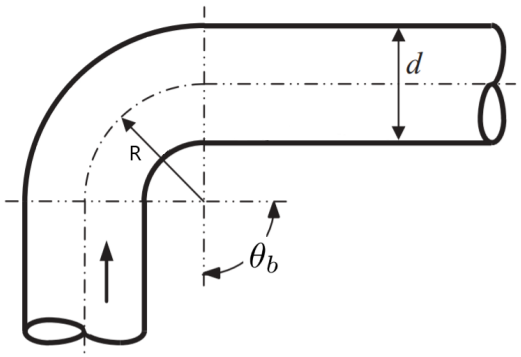

Figure 10: Pipe flow through a bend with bend angle θ_b, radius of curvature R and pipe diameter d. Figure adapted and modified from Ref. [19].

5.5.4 Tees

Tee junctions can be used to divide or combine flows and the losses depend on several factors, such as curvature of the joining edge, direction of flow and proportion of flow division. The governing equations to determine the head loss or K-value are quite extensive and are therefore not mentioned here, as the focus lies on other pipe junctions in this project. Benedict [25] provides equations for separating and joining flow (Equations 10.11 - 10.15 therein). Rennels et al. [19] provides equations and compares these with results from papers in graphical format. Figure 11 shows four different types of fluid flow through tee junctions.

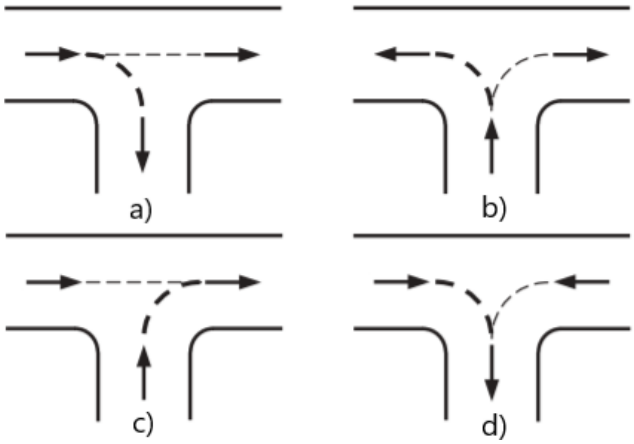

Figure 11: Different types of fluid flow through tee junctions. a) Outbranching b) Separating c) Inbranching d) Combining. Figure adapted and modified from Ref. [19].

5.5.5 Valves

Valves are another source of minor losses within pipes, as the direction of the fluid is often altered by a valve. Also, when the valve is partially closed, this forms an obstruction to the fluid trajectory. Literature reports different K-values for each of the valve types. There exist many valve types and a few are depicted in Figure 12. Tabulated K-values for valves are commonly given for its connecting pipe in inches. Tabulated K-values are given by Menon [21] (Table 1.6 therein), Menon et al. [31] (Table 4.3 therein), White [23] (Table 6.5 therein) and Rennels et al. [19] (Table 18.1 therein).

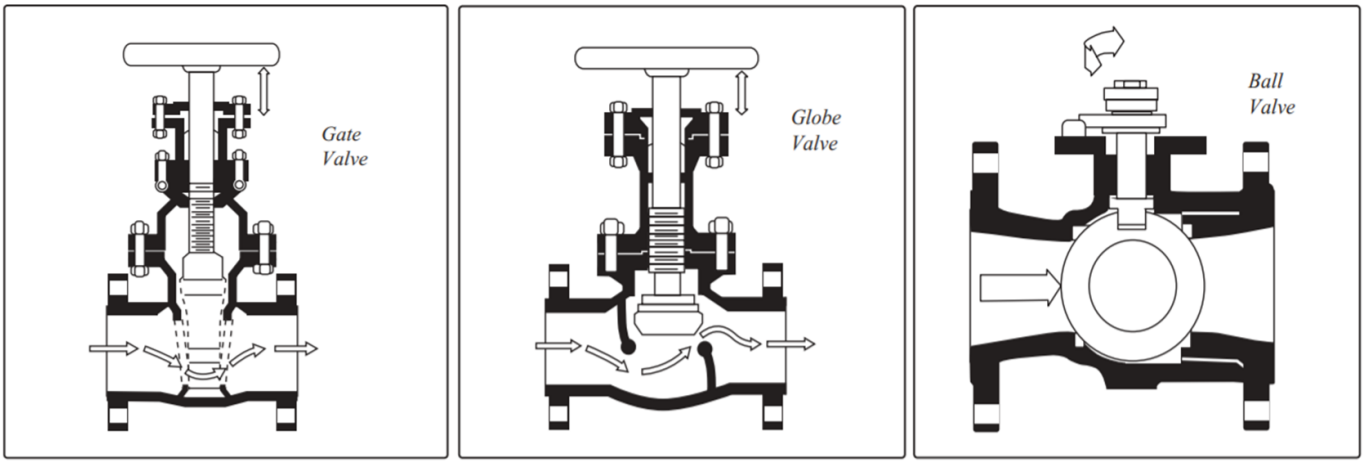

Figure 12: Three different valve types that are commonly used in pipe flow. Figure adapted and modified from Ref. [19].

6 Literature review: Head loss and K-value calculations for minor losses

Table 1 provides an overview with values or equations to determine the induced head loss (h) or the minor friction factor (K-value) for different pipe junctions, such as inlets, enlargements, contractions and bends. Also, the equation, table or figure in the corresponding literature is denoted. Besides, some values or equations have constraints, which are also mentioned. As can be seen from Table 1, for most junctions, there is no unambiguous calculation or value for the head loss h or minor loss coefficient K. To be able to assess which value or equation should be used for a junction, a comparison should be made between simulations, experiments and reported theoretical values.

In Table 1, D_1 denotes the diameter of the smaller pipe and D_2 the diameter of the larger pipe. The ratio of these is expressed by β and is given as $\beta = D_1/D_2 = \sqrt{A_1/A_2}$, where A_1 (A_2) is the pipe cross-sectional area of section 1 (2). v_1 (v_2) is the velocity of the liquid in the smaller (larger) pipe section 1 (2). R gives the radius of the center line of the bend and r gives the radius of the cross-sectional area of the pipe, which is half its diameter as was previously shown in Figure 10. C_c is the jet contraction coefficient for gradual and sudden contractions. f_i denotes the Darcy friction factor in section i, where f_{avg} denotes the average friction factor and f_c denotes the friction coefficient used for bends. Re is the Reynolds number and θ denotes the cone angle, which is twice the angle between the cone axis and its side. L is the length of the gradual enlargement and d_{avg} is the average diameter of the pipe. θ_b is the bend angle, and for values of 45°, 90° or 180°, equations are given. α is the numerical factor for bends. g is again the gravitational acceleration.

Table 1: Minor loss coefficients (K-value) or head loss (h) for different junctions, such as inlets, enlargements, contractions and bends in pipes. All relevant values and equations from literature are denoted, where in most cases no unambiguous value or calculation for either K or h is given in literature.

Minor loss	*K-value (k) or head loss (h)*	*Equation, table, figure or constraint*	*Reference*
Inlet			
Sharp edged	k = 0.5		[21, 22]
			[23, 25]
			[20]
	k = 0.57		[19]
Inward projecting	k = 0.8 - 0.9	Eq. 6.31	[22]
	k = 0.78		[21]
	k = 0.5 - 1.0	Fig. 6.21a	[23]
	k = 0.57 - 1.1	Eq. 9.1, Diagram 9.1	[19]
Rounded	k = 0.04 - 0.5	Fig. 6.21b, bottom line	[23]
	k = 0.04 - 0.5	Fig. 4.3	[31]
	k = 0.04 - 0.2	Eq. 6.31	[22]
	k = 0.03 - 0.57	Eq. 9.2, Diagram 9.2	[19]
Chamfered	k = 0.25	Fig. 4.3	[31]
	k = 0.1 - 0.25	Fig. 6.21b, top lines	[23]
	k = 0.13 - 0.57	Eq. 9.4, Diagram 9.3	[19]
Exit			
All types	k = 1	Sharp edged, outward projecting rounded and chamfered	[21, 23]
			[19, 25]
			[31]

Table 1 continued from previous page

Minor loss	*K-value (k) or head loss (h)*	*Notes*		*Reference*
Sudden enlargement (SE)				
	$h = \frac{(v_1 - v_2)^2}{2g}$	Eq. 6.32[a,b]		[22]
		Eq. 1.40[a,b]		[21]
	$k = \left(1 - \frac{A_1}{A_2}\right)^2 = \left(1 - \left(\frac{D_1}{D_2}\right)^2\right)^2$ $= \left(1 - \beta^2\right)^2 \quad = DEQ$	Eq. 6.77, Fig. 6.22, top line[b]		[23]
		Eq. 7.13, Fig. 10.4[b]		[25]
		Eq. 1.41[b]		[21]
		Eq. 4.31[b]		[31]
		Eq. 2.9[b]		[33]
		Eq. 11.6[b], Diagram 11.1		[19]
		Figure 8.27[b]		[20]
	$h = K\frac{v_1^2}{2g}$	Table 6.5 for K-values. About equal to Fig. 6.22 from Ref. [23].[b]		[22]
Gradual enlargement (GE)				
	$h = K\frac{v_1^2}{2g}$	Table 6.6 for K-values[c]		[22]
		Table 4.7 for K-values[c]		[31]
	$h = \frac{C_c(v_1 - v_2)^2}{2g}$	Eq. 1.43 with Cc from Fig. 1.6[c]		[21]
	$k = 8.30[\tan(\frac{\theta}{2})]^{1.75}(1 - \beta^2)^2 + \frac{f_1(1-\beta^4)}{8\sin(\frac{\theta}{2})}$	$\theta \leq 20°$, Eq. 11.8[d]		[19]
	$k = 2.6\, sin(\frac{\theta}{2})DEQ + f_{avg}\frac{L}{d_{avg}}$	$\theta < 45°$	Eq. 6.79[d]	[23]
			Eq. 2.12[d]	[33]
Sudden contraction (SC)				
	$h = K\frac{v_1^2}{2g}$	Table 6.7 for K-values		[22]
		Table 4.6 for K-values		[31]
	$h = \left(\frac{1}{C_c} - 1\right)\frac{v_1^2}{2g}$	Eq. 1.42, with Cc from Fig. 1.4		[21]
	$k = 0.42DEQ$	$D_1/D_2 \leq 0.76$	Eq. 6.78	[23]
			Fig. 6.22	
	$k = DEQ$	$D_1/D_2 > 0.76$	Eq. 6.78	[23]
			Fig. 6.22	
	$k = 0.0696(1 - \beta^5)\lambda^2 + (\lambda - 1)^2$ $\lambda = 1 + 0.622(1 - 0.215\beta^2 - 0.785\beta^5)$	Equation 10.3 and 10.4 λ is the jet velocity ratio		[19]
Gradual contraction (GC)				
	$k = 0.0696\,\sin(\frac{\theta}{2})(1 - \beta^5)\lambda^2 + (\lambda - 1)^2$ $\lambda = 1 + [0.622\,\sin(\frac{\theta}{180})^{4/5}$ ... $(1 - 0.215\beta^2 - 0.785\beta^5)]$	Equation 10.17 and 10.18 λ is the jet contraction ratio		[19]
	$k = \sqrt{sin(\frac{\theta}{2})}\; 0.5\left(1 - \left(\frac{D_1}{D_2}\right)^2\right)$ $k = 1.6\, sin(\frac{\theta}{2})\; 0.5\left(1 - \left(\frac{D_1}{D_2}\right)^2\right)$	$45° < \theta < 180°$, Eq. 2.13.1 $\theta < 45°$, Eq. 2.13		[33]

Table 1 continued from previous page

Minor loss	*K-value (k) or head loss (h)*	*Notes*	*Reference*
Bends			
$Re(\frac{r}{R})^2 < 91$	$k = 0.00873\alpha_{\theta_b} f_c \theta_b \frac{R}{r}$ $f_c = \left(\frac{r}{R}\right)^{1/2}\left(0.029 + \frac{0.304}{\left[Re(\frac{r}{R})^2\right]^{1/4}}\right)$	Eq. 4	
$Re(\frac{r}{R})^2 > 91$	$k = 0.00241\alpha_{\theta_b}\theta_b\left(\frac{R}{r}\right)^{0.84} Re^{-0.17}$	Eq. 5	
Both regimes	$\alpha_{\theta_b=45^\circ} = 1 + 14.2\left(\frac{R}{r}\right)^{-1.47}$	Eq. 6	[32]
	$\alpha_{\theta_b=90^\circ} = 0.95 + 17.2\left(\frac{R}{r}\right)^{-1.96}$	Eq. 7, for R/r < 19.7	
	$\alpha_{\theta_b=90^\circ} = 1$	Eq. 7, for R/r > 19.7	
	$\alpha_{\theta_b=180^\circ} = 1 + 116\left(\frac{R}{r}\right)^{-4.52}$	Eq. 8	
All regimes	$k = f\theta_b\frac{R}{2r} + (0.10 + 2.4f)\sin(\frac{\theta_b}{2}) + ...$ $\frac{6.6f\left(\sqrt{\sin(\frac{\theta_b}{2})} + \sin(\frac{\theta_b}{2})\right)}{\frac{R}{2r}\frac{4\theta_b}{\pi}}$	Eq. 15.1	[19]

[a] From Equation 5, where it can be rewritten into the K-value equation DEQ.

[b] The limit when $D_2 >> D_1$ is 1. The head loss can be calculated by using the velocity in the smaller pipe.

[c] Both tables and the figure give the same K and C_c values.

[d] Only equations for a cone angle $\theta < 45°$ are denoted as the minimum loss is obtained somewhere in the region $2° < \theta < 20°$ [19, 23].

6.1 Pressure losses from experiments or simulations

Losses in pipes are generally described by three values. One being the pressure loss $[Pa]$ within a pipe section, which is directly linked to the head loss via Equation 9. The second is the head loss h_L $[m]$, which is calculated by rewriting the Bernoulli equation into Equation 6. The third way to describe losses in pipes is the friction factor, or K-value, which is linked to the head loss via Equation 8 for major losses and Equation 18 for minor losses and is defined by:

$$K = \frac{2gh_L}{v^2} = \frac{2g}{v^2}\left(Z_1 + \frac{P_1}{\rho g} + \frac{V_1^2}{2g} - Z_2 - \frac{P_2}{\rho g} - \frac{V_2^2}{2g}\right). \tag{19}$$

When a pipe section has a constant diameter, the inlet and outlet flow rate and thus the velocity in both sections are equal, and thus the velocity terms V_1 and V_2 in Equation 19 cancel out. v then denotes the velocity in the pipe section. However, when these are not equal, which is true for a pipe contraction or enlargement, v denotes the velocity of the fluid in the smaller pipe [21, 22, 31]. When there is no elevation change within a pipe section, Z_1 and Z_2 also cancel out.

7 Theory: Pump-turbine

7.1 Pump, motor and transformer

The behaviour of a pump is generally modelled using a pump performance curve in combination with a set of governing equations. A general pump performance curve and system curve are shown in Figure 13. The system curve or system equation shows how the actual head gained by the fluid from the pump, H_p, is related to the system parameters [20]. It is the sum of the static head H_s, which is defined as the vertical distance between the water surface of the surrounding sea and the water surface in the lower rigid reservoir, and the head losses in the pipes h_L. The system curve increases as the head losses increase with increasing flow rate. There is also a unique relationship between the actual pump head gained by the fluid and the flow rate, as indicated by the pump performance curve (governed by the pump design) [20]. The intersection point of both graphs (point A) represents the operating point for the system and thus gives the head and flow rate that satisfies both the system equation and the pump equation. The efficiency of the pump is also plotted and, ideally, the intersection point is near the best efficiency point (BEP).

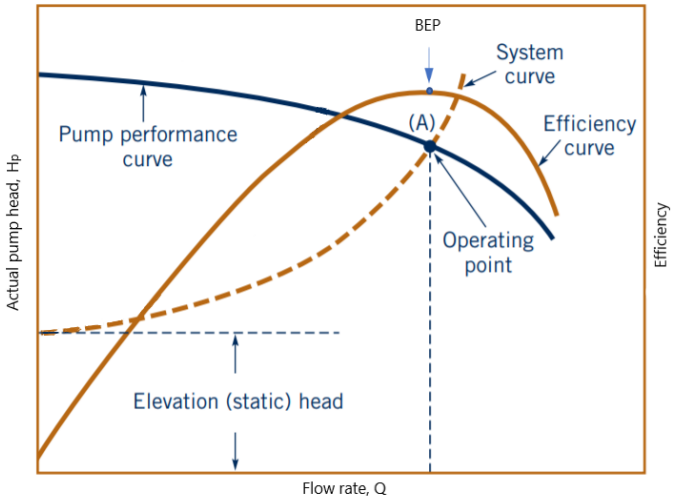

Figure 13: General pump characteristic graphs. The system curve is the sum of the static head H_s and the head losses H_L. The pump performance curve is given by the pump manufacturer and is specific for each pump. The best efficiency point (BEP) indicates for which flow rate the highest efficiency is obtained. No hard numbers are given as it gives a general overview of pump characteristics and no specific pump is determined yet. Figure adapted and modified from Ref. [20].

The flow rate of the pump is thus a function of the power of the pump, which is incorporated into the pump performance curve in Figure 13, its efficiency and the actual head on the pump. The flow rate can then be calculated by [2, 3, 7, 34]:

$$Q_{pump} = \frac{P_p \eta_p}{\rho g H_p}, \tag{20}$$

where P_p is the rated power of the pump [W], η_p is the pump efficiency, dependent on the flow rate itself (Figure 13). The electrical energy from e.g. a wind farm is first fed into a transformer and then into a motor, which converts electrical energy into mechanical energy with a certain efficiency. The motor then drives the pump. The efficiency of the motor is a function of the input power and is generally expressed by an efficiency-power curve. The power of the pump P_p can thus be written as:

$$P_p = P_{motor}\eta_{motor} = P_{trans}\eta_{trans}\eta_{motor}, \tag{21}$$

where P_{trans} indicated the input power into the pump unit that consists of a transformer, motor and pump.

As the energy delivered by the pump is used to elevate the fluid and overcome the head losses, H_p can be written as:

$$H_p = H_s + h_L, \tag{22}$$

where H_s is the static head and h_L the losses in pump mode. The static head is expressed by:

$$H_s = h - H_{water,RR} \tag{23}$$

$$h = H_{sea} + H_{buried} \tag{24}$$

Here, h is the sum of the sea depth H_{sea} and the buried depth H_{buried}, both contributing to the static head, which is the available pressure due to a column of water acting under gravity. The pressure of the water acting at the inlet of the pump lowers the static head, which is the height of the water in the rigid reservoir $H_{water,RR}$.

Losses depend on the fluid velocity, as shown in Section 5, where the fluid velocity again depends on the flow rate and the pipe cross-sectional area, as shown in Equation 3. As a result, Equation 20 depends on the flow rate itself and cannot be directly computed. Therefore, to be able to model the pump behaviour, there are two possibilities: 1) start with a predefined flow rate and calculate the losses for that flow rate or, 2) start with a certain static head and initiate the calculations with zero losses, [2], after which the flow rate is determined and the losses are calculated. These losses can now be incorporated into the calculation of a new flow rate, for which, again, losses are determined. This process is repeated till the flow rate reaches a steady-state value. The latter option takes some iterations and is therefore not as quick as the first and is further explained by Mousavi et al. The first, however, is an approximation to the real flow rate and the real losses can therefore be slightly different from the calculated values.

7.2 Turbine, generator and transformer

To model the behaviour of the turbine, it should be taken into account that the efficiency of the turbine is dependent on the available head, which is the static head H_s minus the head loss in the pipes H_L, as the losses decrease the pressure that is available at the turbine:

$$H_t = H_s - H_L, \tag{25}$$

where H_s and H_L are the same as defined before. The flow rate of the turbine is calculated using [2, 34]:

$$Q_t = \frac{P_t}{\rho g H_t \eta_{t,tot}}, \tag{26}$$

where P_t denotes the designed output power of the turbine. A turbine unit includes a transformer and a generator which converts mechanical energy from the turbine into electrical energy with a certain efficiency. The turbine itself also operates with some efficiency. These efficiencies are combined in $\eta_{t,tot}$. $\eta_{t,tot}$ is therefore given by:

$$\eta_{t,tot} = \eta_{trans}\eta_{gen}\eta_t, \tag{27}$$

where η_{trans} denotes the efficiency of the transformer, η_{gen} the efficiency of the generator and η_t the efficiency of the turbine itself, which is generally given by an efficiency-flow rate curve. Figure 14 shows a general efficiency-flow rate curve for three different turbine types. Here the efficiency depends on the flow rate of the fluid, as a fraction of the maximum flow rate for which the turbine was designed. As it is not yet known what the exact specifications of the turbine are, constant efficiencies for the transformer, generator and turbine are assumed.

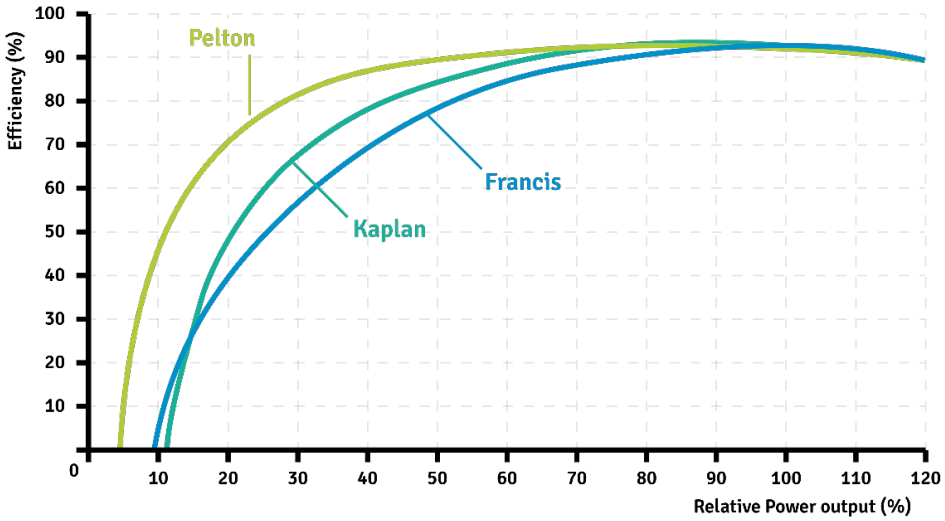

Figure 14: Efficiency - flow rate curve of different turbine types. The efficiency of a turbine is dependent on the flow rate of the fluid, as a fraction of the maximum flow rate. Figure adapted from Ref. [35].

7.3 Assumptions for the pump and turbine operation

When the Ocean Battery is implemented in e.g. an off-shore wind farm, multiple batteries will be present. For each battery, multiple pumps and turbines are available. If there is a certain energy surplus, several pumps will be powered, such that they all perform at or around their BEP. When more energy becomes available, an algorithm decides if an additional pump is powered, or that the running pumps all will operate at a slightly higher flow rate (which can lead to a lower efficiency). As such, for the MATLAB model, it is assumed that a pump always runs at, or at least very close to, its BEP.

Also, when water is pumped from the rigid to the flexible reservoir, the static head H_s increases as the water level in the rigid reservoir goes down. As a result, the flow rate decreases when the same amount of energy is used as input, according to Equation 20. To fully model the losses for each flow rate, the flow rate should be recalculated at certain time steps when emptying the rigid reservoir. J. Bromlewe constructed a MATLAB model which incorporates this for a prototype of the Ocean Battery. This process, however, requires a larger computation time as the flow rate, losses and volumes of the reservoirs need to be updated for each time step. Instead, in this project, the minimum, average and maximum head of the buried Ocean Battery is used to calculate the flow rate of the pump and the accompanying losses, as described in Section 11.1.

For the turbine mode, the same assumptions are used for the efficiencies. Dependent on the required output energy, it is decided how many valves in front of the turbines are opened. In this way, the turbines that are in operation always perform at or at least close to their BEP. It should be noted that increasing the energy input into the pumps or increasing the energy output from the turbines always leads to an increase in flow rate and thus an increase in losses. The fractional increase in losses between different energy inputs/outputs is important as it determined the time scale on which the system can be charged/discharged. If the losses only increase by a small percentage when increasing the energy supply/demand, storing energy using the Ocean Battery is still a viable solution.

8 Matlab model

In this section, the theory from Sections 5, 6 and 7 are implemented in an analytical MATLAB model to analyse the obtainable efficiency for different pipe configurations of the buried Ocean Battery. The model requires some input parameters that are then used in a set of equations, from which the losses are calculated. The final model is shown in Appendix E.

8.1 Requirements

The model should meet several requirements, where the first ensures that the computation time is kept low, in the order of seconds. Compared to the analytical model of Bromlewe for the deep water Ocean Battery prototype, this model will be simplified, such that this requirement is met. Also, the model should be easy to use in terms of input of different pipe configurations and interpretation of results. The input of values for the pipe sections is therefore done using an EXCEL file and the results are also exported to the same file. Besides, the model should be usable for different pipe configurations, such that it can be applied to future designs of the buried Ocean Battery. Also, the model should be able to work for different pipe materials and water temperatures.

8.2 Input

The model that is developed and validated in this project is able to analyse different pipe configurations by changing a set of parameters directly related to the pipes but also related to other factors such as water temperature. For each straight pipe, for which the major loss is calculated, its length, diameter and roughness need to be specified. For each bend, this includes its angle (either 45, 90 or 180°), radius over diameter and the pipe diameter. Also, the number of inlets and exits and their pipe diameter are used as input. For a sudden enlargement, only the pipe diameters of the smaller and larger pipe need to be specified. For gradual enlargements, this also includes the cone angle and roughness. For sudden contractions, again both pipe diameters are included, whereas for gradual contractions also the cone angle is important.

Besides, parameters such as the water temperature, efficiencies of the pump, turbine, motor, generator and transformers and the hydrostatic head need to be specified. Also, the operation mode, either charging or discharging is used as input.

8.3 Calculations

In this section, the general structure of the analytical model, as well as the equations, are discussed. The majority of the equations mentioned in this section are also mentioned in Section 5 or in Table 1.

Before anything is calculated, the density, kinematic and dynamic viscosity of the working fluid, in this case assumed to be water, is extracted from a lookup table after specifying the water temperature. Then, based on either the charging or discharging mode, the flow rate for which the losses are calculated is determined. It is assumed that the efficiencies of the pump, turbine, motor, generator and transformers are all constant. Equations 20 and 21 for the flow rate of the pump are therefore rewritten as:

$$Q_p = \frac{P_{trans}\eta_{trans}\eta_{motor}\eta_p}{\rho g H_p}. \tag{28}$$

Equations 26 and 27 for the flow rate of the turbine are rewritten as:

$$Q_t = \frac{P_t}{\rho g H_t \eta_{trans}\eta_{gen}\eta_t}. \tag{29}$$

8.3.1 Major losses

For the major losses, first, the flow is first classified as laminar or turbulent. For the laminar region, Equations 8 and 10 are rewritten into:

$$h_{L,maj} = \frac{64}{Re}\frac{L}{D}\frac{v^2}{2g}. \tag{30}$$

For the turbulent region, the explicit Serghide approximation as shown in Equation 14 is used to calculate the friction factor.

8.3.2 Bends

For the bends either the equations provided by Ito [32] or Rennels [19] can be used. The work of Ito is widely considered as a pioneering study into losses in pipe bends and the set of equations provided by Ito, also shown in Table 1, is therefore used.

8.3.3 Inlets and exits

For inlets and exits, the minor loss coefficients are used in combination with Equation 18. For some inlet types, different K-values are specified, where one of these values is used. Further simulations can be done using different values. The K-value that is used for a sharp or squared edged inlet is 0.5, for an inward projecting inlet it is 0.8, for a chamfered entrance 0.25 and for an exit it is 1. For a rounded entrance, the K-value depends on the radius over diameter of that entrance. This is different when multiple entrances are present and, therefore, the following equation, specified by Rennels is used [19]:

$$K_{RO} = 0.0696(1 - 0.569\frac{r}{d})\lambda^2 + (\lambda - 1)^2, \text{where} \tag{31}$$

$$\lambda = 1 + 0.622(1 - 0.3\sqrt{\frac{r}{d}} - 0.7\frac{r}{d})^4 \tag{32}$$

8.3.4 Enlargements

For a sudden enlargement, the following equation is used for the minor loss coefficient:

$$k = \left(1 - \frac{A_1}{A_2}\right)^2 = \left(1 - \left(\frac{D_1}{D_2}\right)^2\right)^2. \tag{33}$$

For gradual enlargements, the following equation, specified by Rennels and shown in Table 1, is used:

$$k = 8.30[\tan(\frac{\theta}{2})]^{1.75}(1 - \beta^2)^2 + \frac{f_1(1 - \beta^4)}{8\sin(\frac{\theta}{2})}. \tag{34}$$

8.3.5 Contractions

For sudden contractions, the K-value is calculated using [19]:

$$k = 0.0696(1 - \beta^5)\lambda^2 + (\lambda - 1)^2 \tag{35}$$

$$\lambda = 1 + 0.622(1 - 0.215\beta^2 - 0.785\beta^5). \tag{36}$$

For a gradual contraction, the K-value is calculated using [19]:

$$k = 0.0696\sin(\frac{\theta}{2})(1 - \beta^5)\lambda^2 + (\lambda - 1)^2 \tag{37}$$

$$\lambda = 1 + [0.622\sin(\frac{\theta}{180})^{4/5}(1 - 0.215\beta^2 - 0.785\beta^5)] \tag{38}$$

8.3.6 Structure of the model

For each part mentioned above, a for loop is created in MATLAB such that the equations are solved and the losses are calculated. If, for example, the piping system consists of 3 straight pipes, the losses are calculated separately for each pipe and summed, resulting in the total major loss. It should be noted that the model does not need to know which part is connected to which, as the losses for each part are calculated separately. In the model output, the contribution of each part to the total loss can be seen as a percentage.

8.4 Output

The model calculates the head loss for a certain pipe configuration, fluid flow rate and water temperature. The output of the model includes this head loss, divided into separate sections to which the loss belongs. These sections include the major losses, bend losses, input and output losses, and enlargement and contraction losses. This output with calculated losses is then exported to a separate sheet on the input EXCEL file, such that further processing of the numbers is done easily.

8.5 Assumptions

As the model is based on a set of equations, there are some limitations to which geometries can be analysed and which not. It is hard to include every possible geometry using only a certain set of equations and therefore assumptions are present in the model. The equations used in the model can analyse the losses that are present in general pipes, i.e. straight pipes with bends, enlargements, contractions, different inlets and exits. The pipe material is implemented by using the pipe roughness.

9 Theoretical Background Comsol

For the numerical analysis of losses in a pipe system, computation fluid dynamics simulations are performed using the finite element method based commercial software Comsol Multiphysics [36]. First, some information regarding the equations and models that describe the behaviour of fluid flow in Comsol is given, after which the boundary conditions of the physics interfaces are discussed. Then, some small validation studies are performed with separate pipe sections after which the interaction between two 90° bends is studied.

9.1 Modelling Single-Phase Flow

A distinction is made between single-phase and multi-phase flow and this project focuses on water flowing through pipes, which are always filled and can therefore be described by single-phase flow. Multi-phase flow consists of two or more distinct phases of a gas, liquid or solid within a common interface. Within Comsol, turbulent single-phase fluid (SPF) flow problems are solved using different models. Before going into these models, some background information on turbulence modelling is discussed.

9.1.1 Turbulence Modelling

Figure 15 shows that when a fluid with a uniform velocity profile flows over a flat plate, which can be seen as the wall of a pipe, a laminar boundary layer develops. In the laminar regime, the fluid flow is completely predicted by solving Navier-Stokes equations, which gives the velocity and the pressure fields [37]. Initially, the velocity field is invariant with time, but as the flow begins to transition to turbulence, oscillations appear in the flow. It is therefore necessary to solve the time-dependent Navier-Stokes equations. The domain is discretized into small elements, called meshing. The mesh, or the finite elements of the geometry, must be fine enough to resolve the size of the smallest oscillations or eddies in the flow. As the flow rate increases, the flow exhibits very small oscillations, which are so small that it is computationally unfeasible to resolve them using the Navier-Stokes equations. Therefore, a Reynolds-averaged Navier-Stokes (RANS) formulation is used, which is based on the observation that the flow field (u) over time contains small, local oscillations (u') and can be treated in a time-averaged sense (U). However, the solutions of the RANS equations are problematic, as the number of unknowns exceeds the number of equations [38]. To solve this, recourse is made to a turbulence model, which supplies the additional equations. For the one- and two-equation turbulence models, which are described in Section 9.1.3, additional transport equations are introduced for turbulence variables, such as the turbulence kinetic energy (k in k-ϵ and k-ω), rate of dissipation of turbulence kinetic energy ϵ or the specific dissipation rate ω [30, 38]. For more information about RANS and other equations regarding the modelling of turbulent flow, the CFD Module User's Guide of Comsol provides a section that describes the 'Theory for the Turbulent Flow Interfaces'.

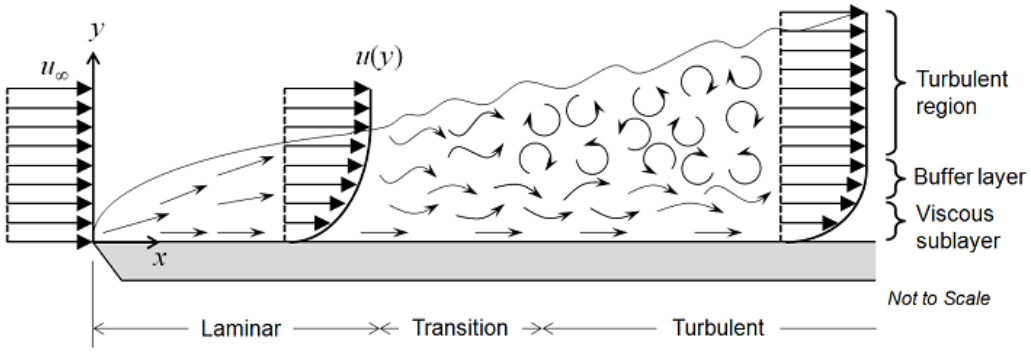

Figure 15: The incoming fluid exhibits a uniform velocity profile and when it flows over the plate, a viscous sublayer and a buffer layer develop. At the wall, the fluid velocity is zero, and in the viscous sublayer, the flow velocity is linear with distance from the wall. The buffer layer connects to a region where the flow is fully turbulent. Figure adapted from Ref. [37].

9.1.2 Wall functions

As previously described, a RANS model is used to compute the flow field and is applied to all layers as shown in Figure 16. At the wall, the fluid velocity is zero and in the viscous sublayer the flow velocity is linear with distance from the wall. The buffer region is a transitional region between the viscous sublayer and the turbulent region. The turbulent region can be divided into two regions, where the log-law region is directly situated above the buffer layer,

and free-stream velocity region is situated at a distance of about 100 times the thickness of the bottom two layers from the wall. In the log-law region, the flow is fully turbulent and the average flow velocity is related to the logarithm of the distance to the wall.

The thickness of the buffer layer and the viscous sublayer is very small and it can therefore be advantageous to use an approximation in this region. Wall functions ignore the flow field in these regions and analytically compute a nonzero fluid velocity at the wall [30, 37]. The idea is that the mesh is not resolved all the way to the wall, which saves on computation time as the mesh is coarser. Instead of modelling with the mesh and solve the problem, we come up with some analytical solution to what needs to be calculated (e.g. velocity). So wall functions model the flow closest to the wall rather than resolving it. This is a very useful approach for many practical engineering applications.

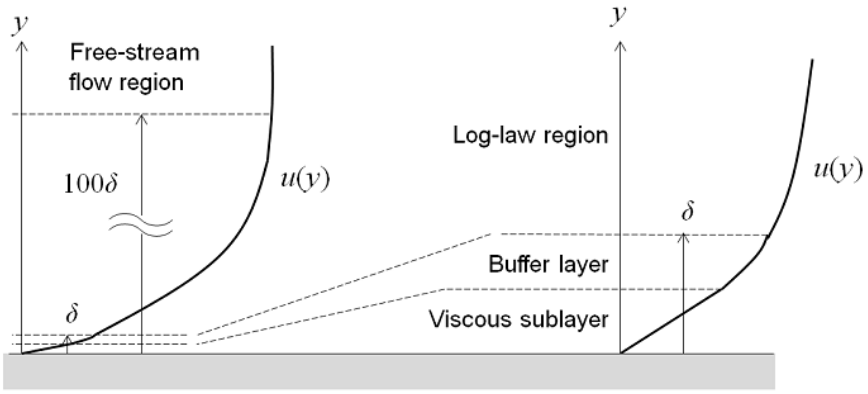

Figure 16: Flow near a wall can be divided into four regions. At the wall, the velocity is zero, but in the viscous sublayer it is linear with distance from the wall. The average flow velocity is related to the log of the distance to the wall in the log-law region. The buffer layer is between these layers. The free-stream velocity region is situated at a distance of about 100 times the thickness of the bottom two layers from the wall. Figure adapted from Ref. [37].

Walls in Comsol have either a slip or no slip boundary condition. A no slip wall is used to model solid walls, where the fluid velocity relative to the wall velocity is zero [30]. A slip wall indicates a no-penetration condition and it is assumed that there are no viscous effects at the slip wall and hence, no boundary layer develops.

Walls can also have a certain roughness, but by default, smooth walls are assumed. Only when a turbulence model uses wall functions, a wall roughness can be applied. Another important term within a study that uses wall functions is wall resolution, which makes sure that the walls within the geometry are well resolved. When using wall functions in Comsol, a theoretical lift-off from the physical wall is assumed as shown in Figure 17. The wall lift-off δ_w is expressed in viscous units by δ_w^+ as:

$$\delta_w^+ = \max(\frac{h}{2}\frac{\rho C_\mu^{1/4}\sqrt{k}}{\mu}, 11.06), \tag{39}$$

where h denotes the mesh cell size [m], ρ the fluid's density [$\mathrm{kg\,m^{-3}}$], $C_\mu^{1/4}$ a model constant, μ the fluid's dynamic viscosity [Pa s] and k is the turbulent kinetic energy [$\mathrm{m^2\,s^{-2}}$]. More information about how the wall lift-off δ_w is calculated can be found on page 180-183 of Ref. [30].

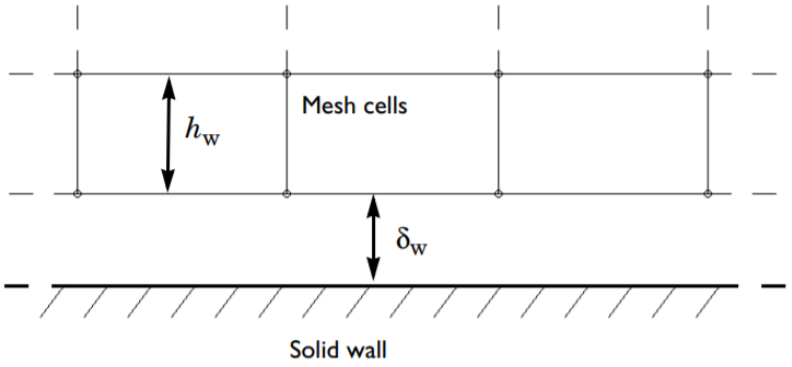

Figure 17: The computational domain is located a distance δ_w from the wall. Figure adapted from Ref. [30].

9.1.3 Turbulence models

The available turbulence models are discussed in Table 2. It includes two algebraic turbulence models; L-VEL and yPlus, and seven transport-equation models, including a standard k-ϵ model, the realizable k-ϵ model, a k-ω model, a shear stress transport (SST) model, a Low Reynolds number k-ϵ model, the Spalart-Allmaras model, and the v2-f model [30]. k is the turbulence kinetic energy, ϵ the rate of dissipation of turbulence kinetic energy and ω the specific dissipation rate.

Each model has its advantages and weaknesses, as tabulated in Table 2. It should be noted that if the fluid is laminar, the turbulent models are still applicable. It does not work the other way around for turbulent flow and laminar flow models. Therefore, only turbulent SPF models are discussed here. For a more in-depth analysis of each turbulent flow model, Chapter 3 of the CFD Module User's Guide of Comsol provides more information about the Single-Phase Flow Interfaces [30].

In general, when a low Reynolds number model is used, it resolves the velocity profile all the way to the wall. A combination can be made from the robustness of wall functions with the accuracy of low Reynolds number models by adapting the formulation to the mesh available in the model, using Automatic Wall Treatment [39]. If the boundary layer mesh is coarse, a robust wall function formulation is used. If the boundary layer mesh is dense, a low Reynolds number formulation is used. All turbulence models in Comsol, except the (realizable) k-ϵ model, support Automatic Wall Treatment.

The two algebraic turbulence models L-VEL and yPlus and the Spalart-Allmaras model are not suitable to simulate the fluid flow in pipes for this project, as they cannot accurately compute the turbulent flows. The k-ϵ could be a usable turbulent flow model as its computation time is classified as medium and it is the most widely used model in industry. The low Re number k-ϵ model could also be useful for this project, however, the mesh needs to be very fine in the boundary layer and therefore the computation time increases. The best k-ϵ model from Table 2 is the realizable k-ϵ model as it is an improvement to the other k-ϵ models.

The k-ω turbulent flow model is also a suitable choice for the simulations in this project, as it is an improvement on the standard k-ϵ model and its theoretical computation time is still medium. The SST model is the most accurate turbulent flow model and should therefore be considered a viable option, however, the major downside of this model is its high theoretical computation time. The v2-f turbulence model adds two equations to the k-ϵ model and therefore has higher accuracy. However, the computational cost is hard to predict beforehand. For both the SST and v2-f models, practice will learn what the computation times are, but both are viable options as turbulence models in this project.

The four suitable turbulence models to model fluid flow through pipes are therefore the k-ω, realizable k-ϵ, SST and v2-f model. These are applied to a fixed geometry in Comsol as discussed in Section 10.1.

Table 2: Information on each turbulence model in Comsol, acquired from Ref. [30, 37, 40]

Turbulence model	Theoretical computation cost	Wall treatment	Advantages	Disadvantages	Notes
L-VEL & yPlus	Very low	Automatic or low Re	Robust, computationally cheap, resolve wall layer	Low accuracy, no turbulent transport, no wake interference, no inflow or outflow of turbulence	Get fast results
Spalart-Allmaras	Low	Automatic or low Re	Stable, does not use wall functions	Does not accurately compute flow which exhibits either separated flow or decaying turbulence	Developed for aerodynamic applications
k-ϵ	Medium	Wall functions	Stable, can use coarser mesh near walls (wall function), performs well for external flow problems	Solution at wall is less accurate, does not accurately compute flow fields which exhibit either adverse pressure gradients, strong curvature of flow or jets	Most widely used turbulence model in industry.
Low Re Number k-ϵ	Above Medium	Automatic or low Re	Computes more accurately forces and flux	Requires finer mesh in boundary layer, requires good inlet/initial conditions for convergence. At higher Re numbers the boundary layer mesh must be very fine, solves all the way to the wall	Almost identical to k-ϵ model, uses either low Re or automatic wall function
Realizable k-ϵ	N/A	Wall functions	Improved standard k-ϵ for separated and swirling flows, boundary flows, strong streamline curvature, and round jets	Not as stable as k-ϵ model. Unknown computational cost indication	Applies realizability by allowing the coefficients in the turbulence transport equations to vary with respect to the mean flow deformation rate as well as k and ϵ
k-ω	Medium	Automatic, wall function or low Re	More accurate for flow with high curvature (e.g. bends), separated flow, adverse pressure gradients and jets, performs well for internal flow problems	Solution at wall is less accurate, sensitive to free stream values for ω for external flows, difficult to get convergence	Improvement to k-ϵ model
SST	High	Automatic or low Re	Tends to be most accurate for solving to the wall, combines k-ϵ in free stream and k-ω near the wall	Requires selecting good initial conditions. At higher Re numbers, boundary layer mesh must be very fine, uses more memory than k-ϵ or k-ω	Most accurate, but computationally intensive
v2-f	N/A	Automatic or low Re	Include cases that require anisotropic turbulence modelling, as robust as standard two-equation models and higher accuracy	Hard to converge and unknown computational cost indication	Adds two equations to the k-ϵ model, describing the transport of turbulent velocity fluctuations normal to the streamlines and the non-local effects such as the wall-induced damping of the redistribution of turbulence kinetic energy between the normal and parallel directions

9.2 Boundary conditions

Besides a turbulence model that defines the physics of the fluid flow, also appropriate boundary conditions and other settings need to be carefully selected.

9.2.1 Inlet/Outlet

The available boundary conditions for an inlet are velocity, fully developed flow, mass flow, and pressure. The exact details for these options are discussed in the documentation of Comsol [30]. The main difference between an inflow velocity and a fully developed flow is that the fully developed flow option adds a virtual extrusion channel in front of the pipe in which the flow fully develops. Under fully developed flow, a flow rate Q and average velocity or pressure can be specified. The mass flow is specified by a flow rate and the pressure option specifies the normal stress on the fluid.

For the outlet, the available boundary condition options are pressure, velocity and fully developed flow. The pressure again specifies the normal stress on the fluid. The fully developed flow is applicable when the flow exits the domain into a long pipe or channel [30]. The velocity denotes a normal outflow velocity from a boundary.

Throughout the system, the flow rate Q will be constant according to the continuity equation, Equation 4. A flow rate can thus be specified for the inlet and outlet for all pipe diameters. If the cross-sectional area does not change along the pipe, the fluid velocity v will also stay constant. For the inlet and outlet boundary, a value for the velocity is then also a viable boundary condition.

9.2.2 Pressure

When the boundary conditions of a pipe inlet and outlet are only specified through a velocity, the RANS equations have an infinite number of solutions. The Navier Stokes equation involves the pressure only through its derivatives, so the pressure should be defined at least at one point with a pressure point constraint [41]. Also, Comsol solves CFD problems using relative pressure instead of absolute pressure [42]. The reference pressure level (zero level) is defined in the physics node of the turbulence model and is kept at atmospheric pressure for this project.

9.2.3 Mesh

Comsol is based on finite elements, and the mesh determines the size of these elements. Mesh is either physics-controlled, where Comsol determines the size of each element or it is user-controlled, where additional settings can be modified. The mesh cannot be infinitesimally small as the computational time then becomes too long, but it also cannot be too coarse, otherwise the results will not accurately represent real behaviour.

10 Validation using Comsol

In this chapter, several simulations will be performed to study the effects of using different turbulence models on a fixed geometry. After this, one turbulence model is picked, which is then used for the remainder of this project. Then, several independent pipe sections, such as a single 90° bend or an enlargement are studied. Finally, the effects of varying the separation distance between two 90° bends, also called an S-bend configuration, is studied to see if they can be treated as isolated bends for all separation distances. Table 3 provides and overview of the geometries and turbulence models that are used per section.

Table 3: Overview which pipe geometry and turbulence model are used per section.

Section	Geometry	Turbulence model
10.1	S-bend configuration, with two 90 degree bends at a distance of 0.5 m from each other, including an inlet and outlet pipe, each of L = 1 m	k-ω, Realizable k-ϵ, SST, v2-f
10.2	Single 90 degree bend with an inlet and outlet pipe, each of L = 1 m	Realizable k-ϵ
10.3	Enlargment of straigth pipe from d1 = 0.2 m to d2 = 0.4 m	Realizable k-ϵ
10.4	S-bend with varying separation distance between bends	Realizable k-ϵ

10.1 Turbulence models

As described in Section 9.1.1, four turbulence models are suitable for modelling fluid flow through pipes of the Ocean Battery. These are the k-ω, realizable k-ϵ, SST and v2-f models, of which information regarding wall treatment and (dis)advantages are tabulated in Table 2. For every turbulence model, an S-bend configuration is created using two 90° bends at a distance of 0.5 m from each other, as shown in Figure 18. This geometry is chosen, as in Chapter 10.4 a proximity study is done using the same geometry, in which the distance between the bends is varied. Fully developed flow with an average velocity of 0.2 m s^{-1} flows into pipe 1 at the top left, which has a length of 1 m. It then flows through bend 1, which is a 90° bend with a radius over diameter (R/d) of 1, followed by pipe 2 with a length of 0.5 m. Bend 2 has the same R/d as bend 1. Finally, it flows through pipe 3, with a length of 1 m. The same inlet condition is applied to the outlet, and as the pipe diameter does not change, this is a valid condition from the conservation of mass. All pipes have a diameter of 0.1 m.

For every turbulence model, Comsol models a steady flow of a viscous, incompressible (i.e. constant density), and isothermal liquid, with the working liquid being water. The temperature is T= 20 °C, for which the density is ρ = 998.2 kg m^{-3}, see Table 13 [20]. A physics-controlled coarse mesh is applied on the full geometry to obtain faster results, of which a part is shown in Figure 19. The full mesh consists of 95 912 domain elements, 9944 boundary elements, and 940 edge elements. This can, however, lead to underestimation or negation of local effects, which would be simulated if a finer mesh would be applied. For now, it is assumed that this coarse mesh can sufficiently calculate the local effects. Furthermore, the applied study is stationary. A zero relative static pressure point constraint is applied to the exit of the S-bend geometry for convergence. On the walls, a no-slip boundary condition was applied, and the roughness of the pipe is set to 50 µm, which is the standard for a steel pipe [19, 23, 30].

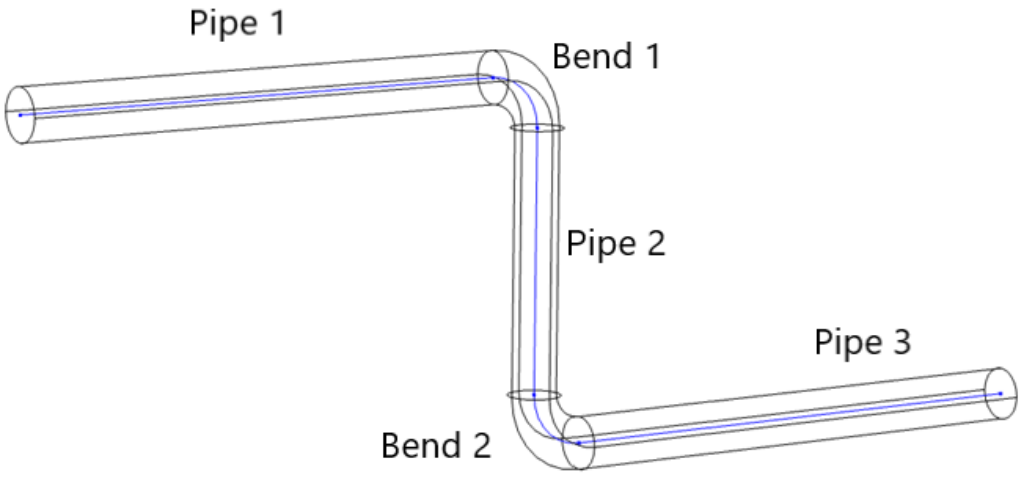

Figure 18: S-bend geometry with the pipe and bend number indications. The blue line indicates the pipe axis line, which runs exactly through the middle of the pipes and bends.

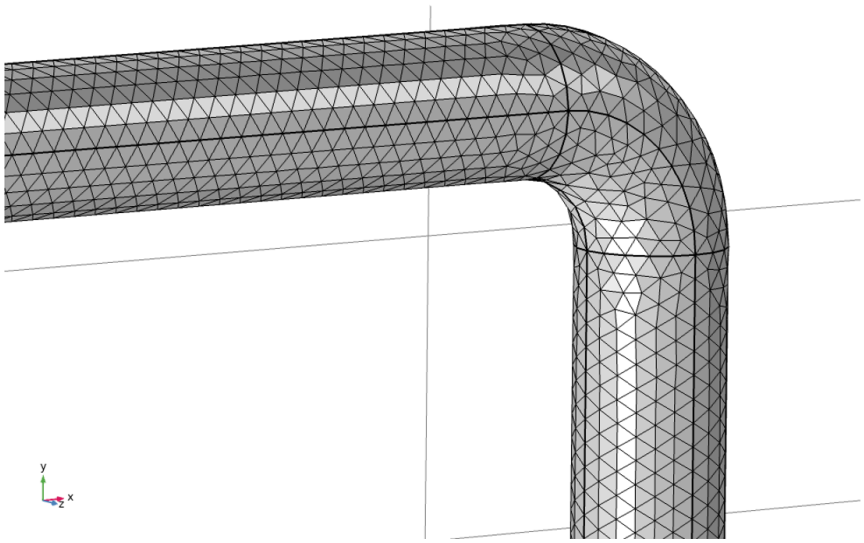

Figure 19: View of part of the generated mesh of a single corner and the connecting pipes. The mesh is equal for all four turbulence model studies.

After each simulation has run, the first thing that pops out is the computation time of each simulation. The simulation with the realizable k-ϵ model takes only 13 min, where the k-ω model takes 27 min. The v2-f model finishes in 44 min and the one with the SST model takes up 78 min. The computation time of the realizable k-ϵ model is therefore only 50% of the computation time of the $k-\omega$ model and 33% of the v2-f model, and only 17% of the SST model.

All four simulations show similar pressure plots with roughly the same minimum and maximum values as shown in Table 15 in Appendix B. The plots with the velocity streamlines are shown in Figure 20. These show great resemblance among the different simulations, only the SST model shows a really low velocity profile at the walls, extending up to 1.5 cm into the pipe. Then there is a sudden transition into the free stream with a much higher velocity. The wall resolution at that pipe section can be of influence on the results. The wall resolution plot for the SST model is shown in Figure 21 and shows that it only takes a value between 1 and 3, which is rather low. A higher wall resolution means that the walls are well resolved and the mesh is fine enough. For the v2-f turbulence model, only small parts of the pipe walls show very low wall resolution, but the majority shows a wall resolution of at least 6. Increasing the mesh probably fixes these problems with these models, however, this results in an even higher computation time.

To quantify these results, the overall pressure drop in all pipes is analysed. As was shown in Table 15 in Appendix B, some differences are present in the total pressure drop between the simulations with the turbulence models. The $k-\omega$ model shows a pressure drop of 26.5 Pa, and the realizable k-ϵ model 26.1 Pa. The SST model shows only a pressure drop of 15.5 Pa, which is a difference of 41% compared to the average of the first two models (26.3 Pa). The v2-f model gives a pressure drop of 27.4 Pa, which differs only by 4.1% from the average of the first two models. It is therefore concluded that, for this geometry and settings, the SST model cannot accurately compute the pressure drop in the pipes, as the other models can, as these numbers lie within 4.1% of each other.

Based on these simulations, it is concluded that the realizable k-ϵ model shows a low computation time for this geometry and settings, it shows similar results as the other turbulence models and has the option to use wall roughness. Therefore, the realizable k-ϵ model is found to be the best option as a turbulence model for pipe flow simulations in Comsol. This turbulence model will therefore be used in all upcoming simulations, and because its computation time is already short, the mesh can be made finer, if preferred.

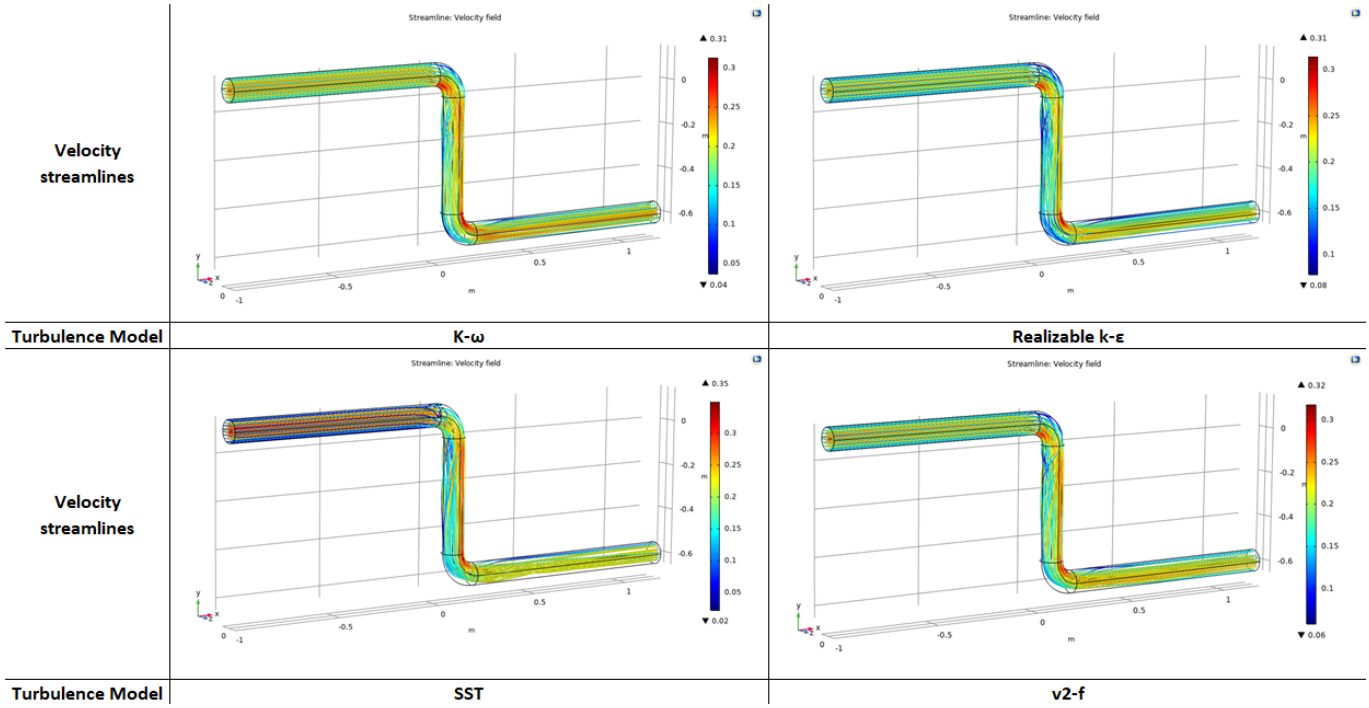

Figure 20: Simulated velocity profiles for different turbulence models applied to the S-bend geometry. All show great resemblance, except for the SST turbulence model.

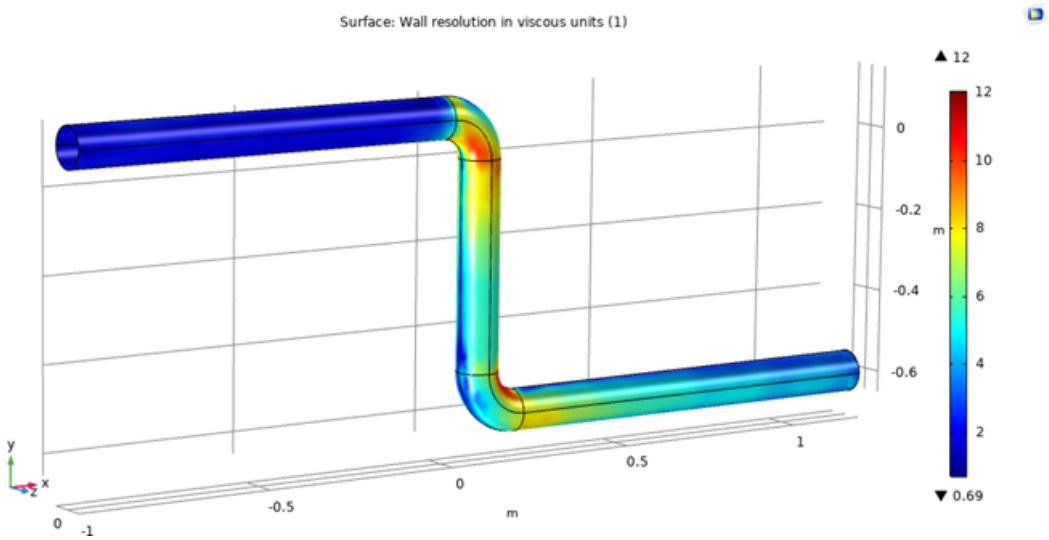

Figure 21: Wall resolution in viscous units for the SST turbulence model applied to the S-bend geometry.

10.2 Varying bend radius of a single 90° bend

If a liquid needs to be transported from point A to point B, this usually is not possible using only straight pipes and often a 90° bend is used. A single pipe bend of 90° is expressed by the parameters discussed in Section 5.5.3. A parameter that is of interest is the bend radius over diameter R/d. Varying R/d has an effect on the losses that are induced in the bends, as sharper bends (low R/d) usually show more flow separation from the walls, but larger bends show more frictional losses.

To simulate this behaviour, a geometry that includes two straight pipe sections with a length of 1 m and a bend with variable R/d is created in Comsol, as shown in Figure 22. The flow needs to be transported from the top left to the bottom right. All pipes have a diameter of 0.1 m.

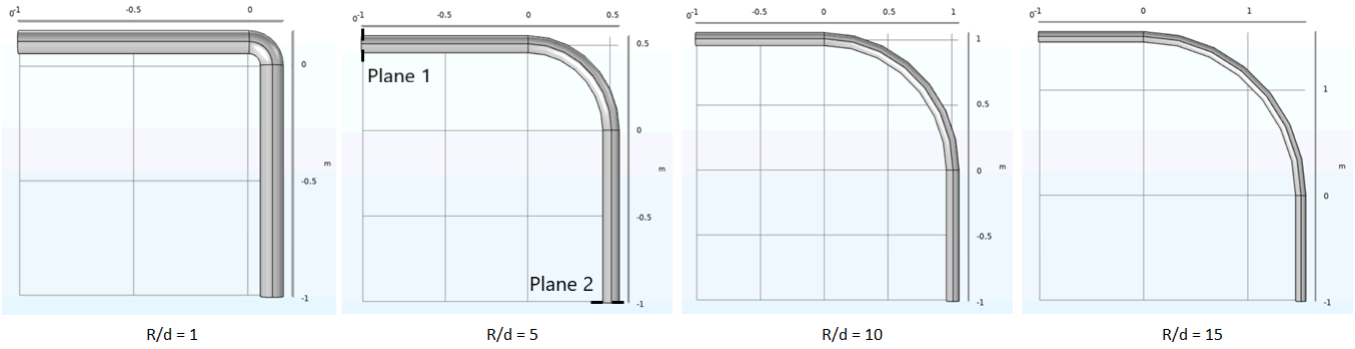

Figure 22: Single 90° pipe bend with different R/d, such that flow gets transported from the top left to the bottom right. The pipe diameter is 0.1 m and the average flow velocity is $0.2\,\mathrm{m\,s^{-1}}$.

A fully developed flow with an average velocity of $0.2\,\mathrm{m\,s^{-1}}$ is imposed on both the inlet and outlet as a boundary condition, and as the pipe diameter does not change, these are valid boundary conditions to use. The Reynolds number is calculated to be 20 000 using Equation 1 and therefore the flow is turbulent. The losses within these different bends can be analysed by calculating its K-value using Equation 19. To do so, the pressure and the velocity of the fluid needs to be measured at two points, in front and after the bend. From experience within the Ocean Grazer B.V. this is done at 10 pipe diameters in front and after the bend, as the bend influences the fluid even after the bend. As the pipe diameter is 0.1 m, the pressure and velocity of the fluid are measured at a point within the cross-sectional planes 1 m before and after the bend, as indicated for an R/d value of 5 in Figure 22. One could also measure the pressure and velocity directly in front and after the bend, however, the fluid is not able to restore, yet, and the losses will thus be higher. This results thus in higher K-values. In reality, the position of these measurement points can vary within these cross-sectional planes.

Before calculating the K-value, the exact measurement location should be know. To show the effects of measuring the velocity and pressure at different points within the pipe, five different measurement points are taken within cross-sectional plane 2, after the bend. The cross-sectional view of the fluid velocity profile, including the five measurement points, at plane 2, for an R/d value of 5 can be seen in Figure 23. The same cross-sectional view with the pressure profile can be seen in Figure 24. The velocities and pressures are extracted and tabulated in Table 4. Here, it can be seen that measuring these values at a single point, which is done in reality, can alter the outcome a lot. The pressure and velocity can, in Comsol, also be measured using a surface average of that cross-sectional plane. The results from the point measurements are compared to a surface average, as shown in Table 4. This shows that measuring at a different point within the cross-sectional plane results in a pressure that differs at maximum 85% and a velocity that differs at maximum 21% from the surface average values. Measurements of the pressure and/or velocity therefore should be taken with cause and always at the same position. To negate the effect of obtaining different results when measuring at different points in a plane, measurements of pressure and velocity are done using a surface average at planes 1 and 2.

Table 4: Pressure and velocity measurements in a cross-sectional plane (plane 2 in Figure 22) for an R/d value of 5. Also, the differences (in %) between the measurements at a point and the surface average are given. Negative pressure means that the measured pressure is below atmospheric pressure, which is set to 0 Pa in Comsol.

Plane 2	Coordinates	Pressure [Pa]	Difference [%]	Velocity [m/s]	Difference [%]
Surface average	Plane	-3.218	-	0.200	-
Point 1	(0.5, 0)	-5.953	84.98	0.242	21.10
Point 2	(0.54, 0)	-1.060	-67.05	0.1997	-0.18
Point 3	(0.46, 0)	-3.864	20.07	0.161	-19.64
Point 4	(0.5, 0.04)	-1.585	-50.74	0.190	-5.07
Point 5	(0.5, -0.04)	-1.518	-52.84	0.192	-4.07

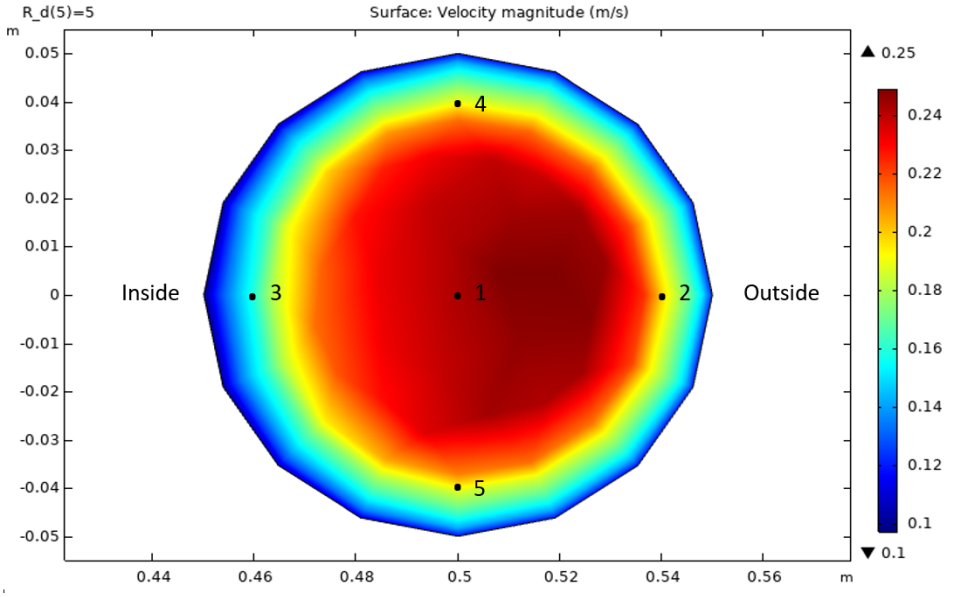

Figure 23: Velocity profile in a cross-sectional plane (plane 2 in Figure 22) for an R/d value of 5. Coordinates of the measurement points: 1: (2,0), 2: (2.04,0), 3: (1.96,0), 4: (2,0.04) and 5: (2,-0.04). Point 3 lies at the inside of the bend and point 2 at the outside of the bend. The inside and outside of the bend are indicated.

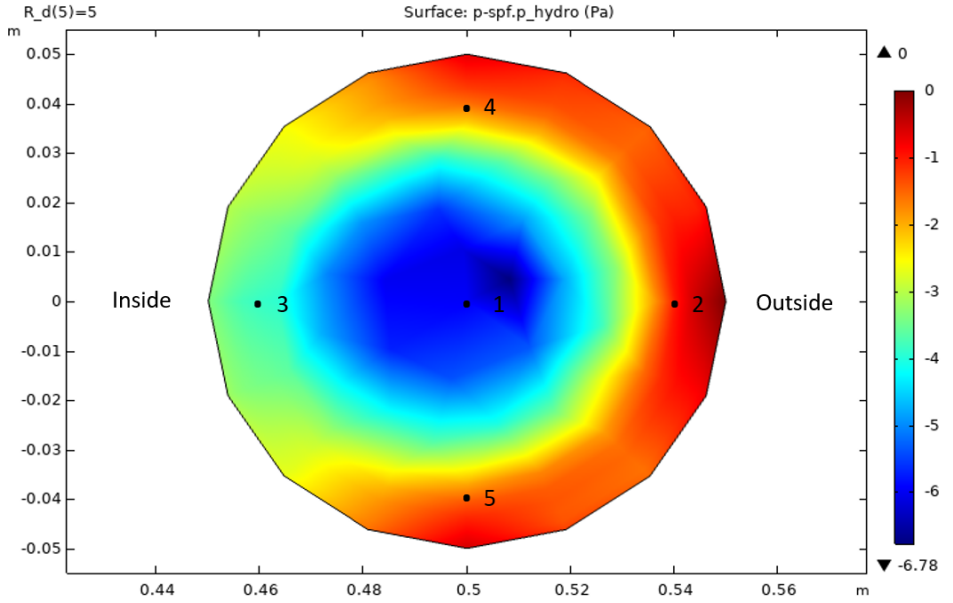

Figure 24: Pressure profile in a cross-sectional plane (plane 2 in Figure 22) for an R/d value of 5. Coordinates of the measurement points: 1: (2,0), 2: (2.04,0), 3: (1.96,0), 4: (2,0.04) and 5: (2,-0.04). Point 3 lies at the inside of the bend and point 2 at the outside of the bend. The inside and outside of the bend are indicated.

Now the K-values are determined, where the height difference is accounted for by measuring the pressure minus the hydrostatic pressure. The pressures and velocities at planes 1 and 2 for different values of R/d are tabulated in Table 16 in Appendix C. From these values, K-values are calculated using Equation 19. To calculate a K-value only for the bend, the frictional losses in the straight pipes between the cross-sectional planes and the bend itself should be subtracted from the results. These losses are calculated using Equation 8 with f being 0.026, from Figure 7 for Re = 20 000. The K-values are also tabulated in Table 16 and graphically shown with the yellow line in Figure 25 (Comsol). Also, the theoretical values from Ito [32] and Rennels [19], for which the equations are shown in Table 1 in the Bend section, are plotted.

As shown in Figure 25, the K-values calculated using the simulations in Comsol follow the trends of the theoretical values from both Ito and Rennels. It increases as the bend R/d increases, resulting in an increase in frictional losses. This holds up to a R/d value of 3, where it shows a minimum K-value. Ito shows a minimum K-value around R/d

= 2.5 and Rennels around $R/d = 1.5$. The K-values mentioned in literature are a result of several experiments [19, 32]. The overall K-values from the simulations are lower than the theoretical values and the losses are therefore underestimated. At $R/d = 6$, there is a small bump in the graph, but this is only minor and could occur due to small deviations in the calculations of velocity, pressure and dissipation of (kinetic) energy in the simulations. No further investigation is done into these small deviations as the overall trend is comparable to what is found in literature.

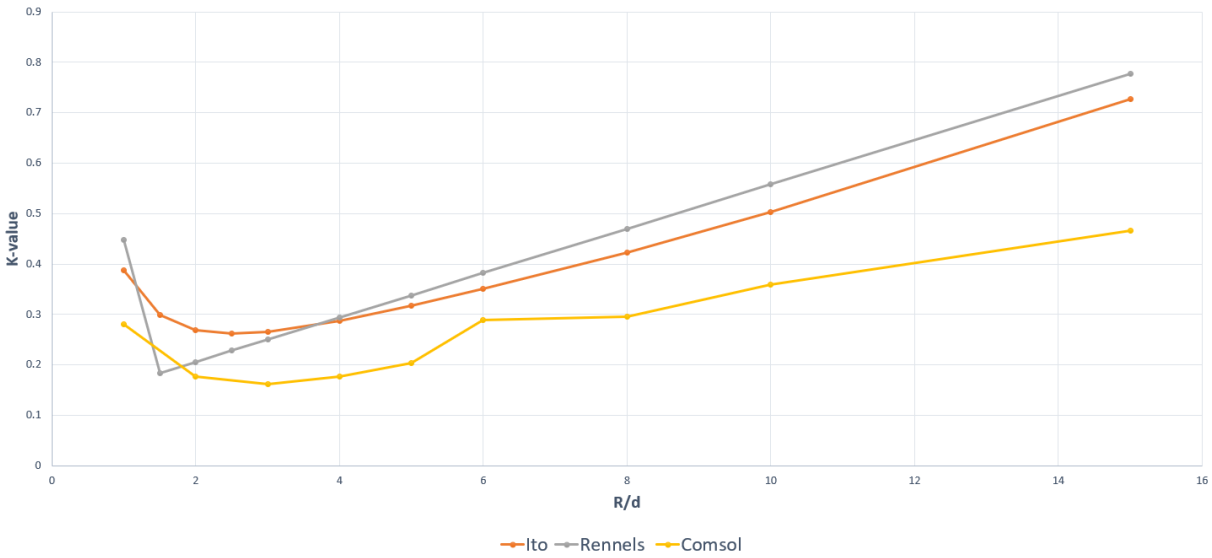

Figure 25: Variation of total bend-loss coefficient K with a radius over diameter R/d at Reynolds number = 20 000 for fluid flow through a single pipe bend.

As briefly mentioned in Section 5.5.3, losses in pipes are composed of three components, surface friction, secondary flow and flow separation. The shape of the lines in Figure 25 resembles these distinct effects, which can be seen in Figure 26. The lower region represents ordinary surface friction loss as in a straight pipe. The mid- and upper regions can be attributed to secondary flow loss and flow separation loss, respectively [19]. As a bend R/d increases, the bend becomes longer, increasing the frictional losses. Secondary flow of the fluid is present in all bends, causing additional turbulence and thus losses. Only for short bends, with small R/d values, the flow has to make a very sudden turn, resulting in flow separation from the pipe walls.

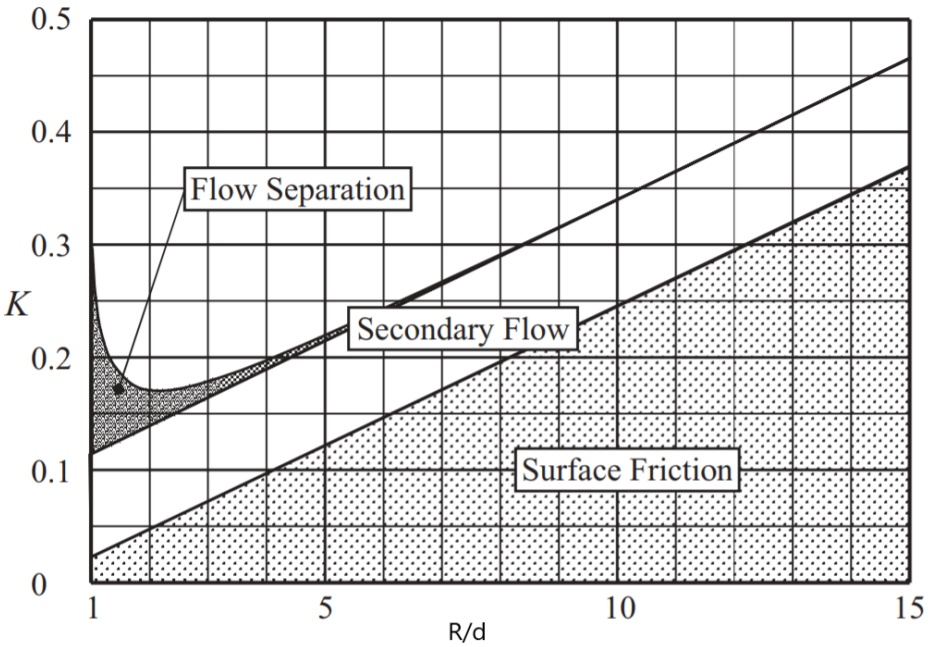

Figure 26: The distinct effects of surface friction, secondary flow, and flow separation in a pipe bend. Figure adapted from Ref. [19].

10.3 Pipe enlargement

Pipe enlargement can be sudden or gradual, as explained in Section 5.5.1, however, there are also more complex configurations possible, as mentioned by Rennels et al. (Chapter 11 therein) [19], which will not be discussed here. This chapter focuses on the configuration of a conical enlargement, which is expected to have a lower pressure loss than the sudden enlargement. As mentioned in literature [19, 23], the range of angles between 2° and 20° is of greatest interest in pipe flow applications, as this indicates the region where a minimum loss is obtained. A large cone angle θ shows the same behaviour as a sudden enlargement and for very small cone angles, the diffuser is very long and shows too much frictional losses [23].

A conical enlargement is symmetrical around its pipe axis, therefore a 2D axisymmetric model is built in Comsol to study the pressure losses. Figure 27 shows a schematic overview of the conical enlargement, also called a diffuser. The diameter of the smaller pipe d_1 is taken to be 0.2 m and d_2 is 0.4 m. The cone angle θ is varied between 4 and 30°. A flow rate Q of 0.2 $\mathrm{m^3\,s^{-1}}$ is imposed on the inlet and also on the outlet ($Q_{in} = Q_{out}$), according to the continuity equation (Equation 4).

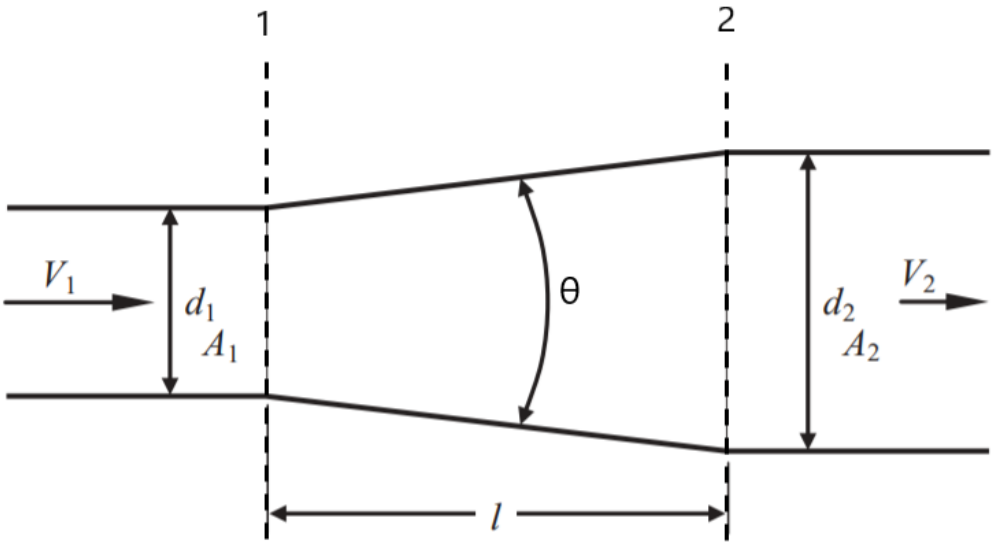

Figure 27: Conical diffuser geometry where $d_1 = 0.2\,\mathrm{m}$, $d_2 = 0.4\,\mathrm{m}$ and the flow rate $Q_{in} = Q_{out} = 0.2\,\mathrm{m^3\,s^{-1}}$. (1) and (2) indicate the planes at which the pressure and velocity are measured using a surface average. θ indicates the cone angle.

The pressure and flow velocity are measured using a surface average at planes 1 and 2. As the cone angle increases, the diffuser length l decreases and plane 1 shifts towards plane 2. Plane 2 will be stationary at the end of the enlargement. As the cross-sectional area of the pipe increases across the diffuser, the pressure increases from plane 1 to plane 2 and the velocity decreases. The theoretical pressure increase for the pipe configuration given in Figure 27 is calculated using Equation 5:

$$Z_1 + \frac{P_1}{\rho g} + \frac{V_1^2}{2g} = Z_2 + \frac{P_2}{\rho g} + \frac{V_2^2}{2g} + h_L.$$

As there is no change in elevation, Z_1 and Z_2 are set to zero, and as this is a theoretical pressure increase, no losses are present yet ($h_L = 0$):

$$\frac{P_1}{\rho g} + \frac{V_1^2}{2g} = \frac{P_2}{\rho g} + \frac{V_2^2}{2g}, \tag{40}$$

resulting in a theoretical pressure increase across the diffuser of:

$$\begin{aligned} P_2 - P_1 &= \frac{\rho}{2}\left(V_1^2 - V_2^2\right) \\ &= \frac{\rho}{2}\left(\left(\frac{Q_{in}}{A_1}\right)^2 - \left(\frac{Q_{out}}{A_2}\right)^2\right) \\ &= \frac{\rho}{2}\left(\left(\frac{Q}{0.25\pi d_1^2}\right)^2 - \left(\frac{Q}{0.25\pi d_2^2}\right)^2\right) \\ &= \frac{998.2}{2}\left(\left(\frac{0.2}{0.25\pi 0.2^2}\right)^2 - \left(\frac{0.2}{0.25\pi 0.4^2}\right)^2\right) = 18\,964\,\text{Pa}. \end{aligned} \tag{41}$$

The pressure and velocity, measured at planes 1 and 2, for different cone angles θ are tabulated in Table 5. Also, the simulated pressure increase over the diffuser is shown in Table 5. As can be seen, the theoretical pressure increase is never reached, but as the conical angle decreases, the simulated pressure increase approaches the theoretical value. From these results, a loss coefficient, or K-value, is calculated using Equation 19. Besides the simulated results, also K-values from theory can be calculated for this diffuser using the equations shown in the Gradual Enlargement section in Table 1. These results are shown in Appendix C, Table 17.

Table 5: Measured pressure and velocity at planes 1 and 2, as indicated by Figure 27. The pressure increase from Comsol is the pressure at plane 2 minus the pressure at plane 1. A negative pressure at plane 1 indicates that the pressure is below atmospheric pressure, which is the zero pressure level. The K-value can be calculated using Equation 19.

	Plane 1		Plane 2		Comsol	Eq. 19
θ [°]	Pressure [Pa]	Velocity [m s^{-1}]	Pressure [Pa]	Velocity [m s^{-1}]	$P_{increase}$ [Pa]	K-value [-]
4	-164.6	6.17	17578	1.47	17742.6	0.010
6	-1065.7	6.18	15942	1.33	17007.7	0.060
8	-1518	6.18	14787	1.25	16305	0.105
10	-1792.2	6.19	13771	1.18	15563.2	0.150
15	-2169.1	6.21	11766	1.07	13935.1	0.246
20	-2369.5	6.22	10272	1.10	12641.5	0.315
30	-2606	6.25	8997.5	1.15	11603.5	0.371

The simulated and theoretical K-values for a diffuser from 0.2 to 0.4 m for varying cone angles is shown in Figure 28. As can be seen, all K-values increase as the cone angle is increased, indicating that a more sudden enlargement from 4 to 30° is unfavourable in terms of losses. Both White [23] and Rennels [19] show a minimum in the K-value for a cone angle between 5 and 8°. This behaviour is not seen with the Comsol simulations, however, for cone angles above 15°, it follows somewhat the theoretical values as predicted by White and Crane [33].

For cone angles smaller than 15°, the Comsol simulations show a steep drop towards lower K-values. It does not show exactly the same behaviour as theory suggests, namely a minimum K-value somewhere between 2 and 20°, however, it shows that low K-values can be obtained for small cone angles, which is useful in the design of the buried Ocean Battery. A possible explanation for this is that it depends on where the pressure and velocity of the fluid is measured along the pipe. For the simulations done here, plane 1 is exactly at the entrance of the diffuser and moves towards plane 2 when the cone angle increases, as shown in Figure 27. Plane 2 always stays at the exit of the diffuser. The pressure not only increases along the diffuser, but also within the pipe after it [19]. Measuring the pressure and velocity some distance behind the exit of the diffuser would probably give in different results. The equations given by Rennels [19] are based on experiments done by Gibson [43], in which the pressures were measured shortly before the expansion and at some downstream length after it. This distance downstream increased as the cone angle increased. The measurement positions for the pressure and velocity are not given in the corresponding literature for the other graphs.

For the Comsol simulations, it can be seen that the curve flattens towards higher cone angles, indicating a maximum K-value for a certain cone angle. This behaviour is not yet seen for the theoretical curves, however, it is expected from literature that all curves flatten and reach a maximum K-value for a certain cone angle above 30°. For these cone angles, the flow is separated from the diffuser walls over the whole perimeter and the resulting turbulence produces losses greater than for a sudden enlargement, as can be seen in Figure 29 [19]. The maximum K-value could be obtained for a smaller cone angle in the Comsol simulations than literature suggest, however, no further investigations are done as the focus lies at the angles for which the minimum K-value is obtained.

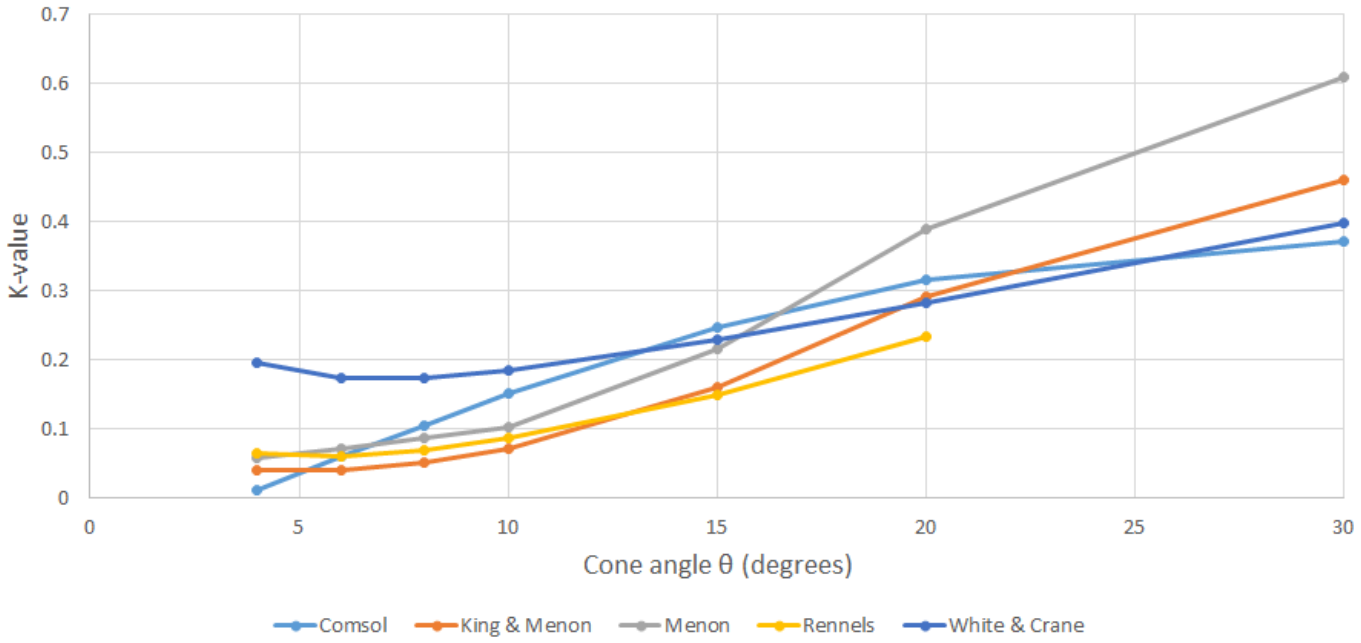

Figure 28: Simulated and theoretical K-values for a conical pipe enlargement (diffuser) from 0.2 to 0.4 m for varying cone angles θ. The geometry can be seen in Figure 27. The equation given by Rennels [19] is valid for $\theta < 20°$.

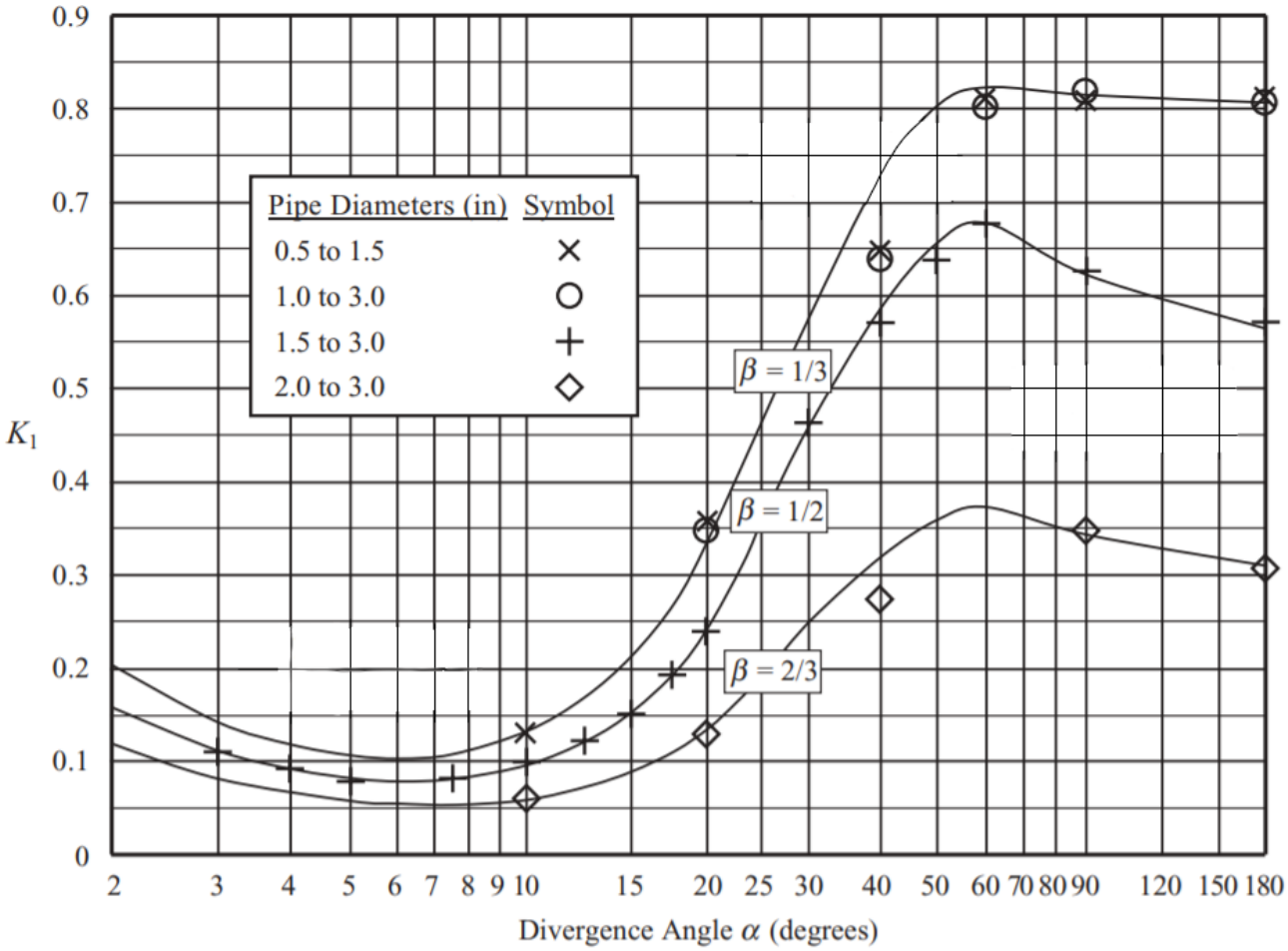

Figure 29: Loss coefficients for conical pipe enlargement (diffuser) for varying cone angle and β. Figure adapted and modified from Ref. [19].

In reality, other factors influencing the loss coefficient K are the boundary layer thickness at the entrance, the shape of the incoming velocity profile, and the degree of flow turbulence at the entrance [19]. In the Ocean Battery, also rotating machinery such as a pump or turbine are present, which can cause swirls in the fluid. This swirl can have a beneficial effect on the performance of diffusers as it helps to spread the core flow to the walls of the diffuser [19]. However, in general, swirls cause energy losses due to the shearing of layers. No further simulations are done using swirls within pipe expansions due to the time limitations of this project and the complexity of these simulations.

A gradual pipe enlargement has been discussed above, where low K-values are obtained for small cone angles. For a sudden enlargement with a cone angle of 180°, the expected K-value from Table 1 is either 0.5625 [19, 20, 21, 23, 25, 31, 33] or 0.60 [22]. If the same measurement strategy with planes 1 and 2 is used for a sudden enlargement, plane 1 would coincide with plane 2 and no information about the pressure increase can be deducted. Therefore, the pressure and velocity are measured 0.1 m before the enlargement and 5 m after the enlargement using again a surface average in COMSOL. The values are presented in Table 6. Again, a K-value is calculated, which takes a value of 0.561. This comes close to the theoretical values mentioned previously.

Table 6: Measured pressure and velocity at 0.1 m in front of the enlargement and 5 m after it. The pressure loss is the difference between the theoretical and simulated pressure increase across the diffuser. The K-value are calculated using Equation 19.

	0.1 m before enlargement		5 m after enlargement		Comsol	Eq. 19
θ [°]	Pressure [Pa]	Velocity [$\mathrm{m\,s^{-1}}$]	Pressure [Pa]	Velocity [$\mathrm{m\,s^{-1}}$]	$P_{increase}$ [Pa]	K-value [-]
90	-2688	6.15	4428.5	1.53	7116	0.561

10.4 S-bend proximity study

10.4.1 Single separation distance of 1 m

For this proximity study, the same geometry as in Figure 18 is used, also adapting the same boundary conditions and coarse mesh size. Only the outlet boundary condition is changed from a fully developed flow of $0.2\,\mathrm{m\,s^{-1}}$ to a pressure of 0 Pa. This was done after analysing the results with the original boundary condition, which showed a steep incline in losses close to the outlet boundary, indicating some issues there. The distance between the two bends (i.e. the length of pipe 2) is kept constant at 1 m for now, but is varied in the next section. This distance is also called the separation distance, as shown in Figure 18. The realizable k-ϵ turbulence model is again used.

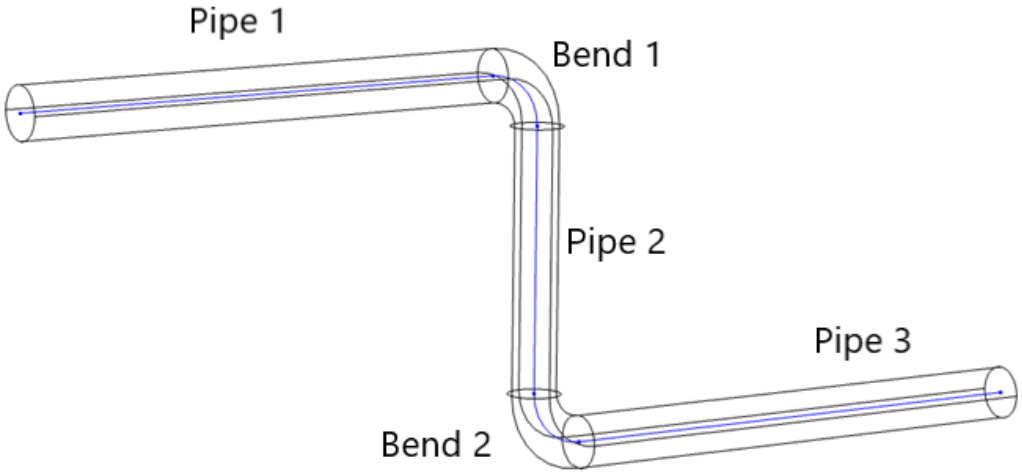

Figure 18: S-bend geometry with the pipe and bend number indications. The blue line indicates the pipe axis line, which runs exactly through the middle of the pipes and bends.

The pressure drop along the pipes is analysed and in this way, the losses that are induced in each pipe section can be studied. To plot the pressure drop, first, a line is drawn exactly at the center of each pipe section along the full pipe length, thus on the pipe axis, as indicated with the blue line in Figure 18. Next, the hydrostatic pressure is subtracted from the total pressure along the pipe axis line, such that the height difference is accounted for. Besides, no visible differences can be identified in velocity and pressure plots when placing the geometry in a horizontal position, i.e. changing the axis of the acceleration of gravity.

Now that the pressure loss can be plotted along the axis line, it is set to 0 Pa loss at the entrance of pipe 1, such that the losses along the pipe length are expressed as negative pressures. For an S-bend with a separation distance of 1 m, the pressure loss in [Pa] is plotted in Figure 30. Here the pipe sections are indicated at the top of the figure, referring back to the geometry as in Figure 18 and the beginning (0°) and end (90°) of each bend is indicated with a red vertical dotted line. The x-axis indicates the distance along the pipe axis line (arc length). As can be seen, the pressure declines linearly in the first pipe, as can be expected due to the friction between the fluid and the pipe walls from Equation 8. When the fluid enters the first bend, the pressure shortly increases because the bend acts as a constriction [44]. After the pressure increase in the bend, it drops rather fast, even after the bend due to the redirection of the flow. After the bend, the pressure recovers and again, there is a linear pressure drop along the straight pipe section (pipe 2) with a slope equal to that in pipes 1 and 3. In bend 2, the same behaviour is observed as in bend 1.

Within the bends, the pressure increases in the outer regions of the bend as the velocity decreases. Contrary, in the inner region of the bend, the velocity increases, and the pressure thus decreases. Figure 31 depicts this pressure increase at the outside and pressure decrease at the inside of the bend, which is in line with the results from a pioneering study by Ito [32]. These pressure differences are of influence on the pressure at the pipe axis.

Overall, the pressure drops to −29.4 Pa as calculated on the pipe axis, which means a head loss of 3.0 mm, as calculated using Equation 9. This head loss is very small for such a geometry, because the flow velocity is only $0.2\,\mathrm{m\,s^{-1}}$ and the roughness of the pipe is only 50 µm. In this case, no pressure point constraint was used anymore, as the pressure was defined by the outlet boundary condition. If a Comsol model uses this pressure point constraint, all values for pressure would be scaled with this value. Therefore, the graph of the pressure drop would be scaled up, if this value was greater than zero. However, the total pressure drop remains the same along the pipe geometry.

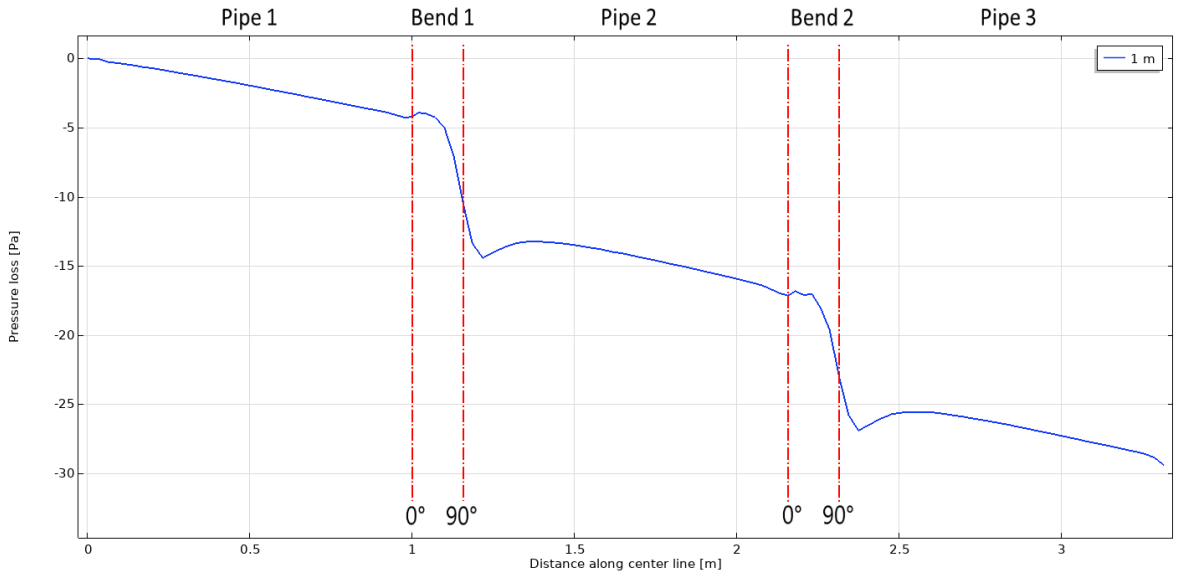

Figure 30: Pressure drop in an S-bend configuration with a separation distance of 1 m. The pressure loss is displayed as negative pressure. The beginning and end of bend 1 and 2 are indicated using 0° and 90°, respectively. The total pressure drop in this pipe configuration and for these settings is 29.4 Pa.

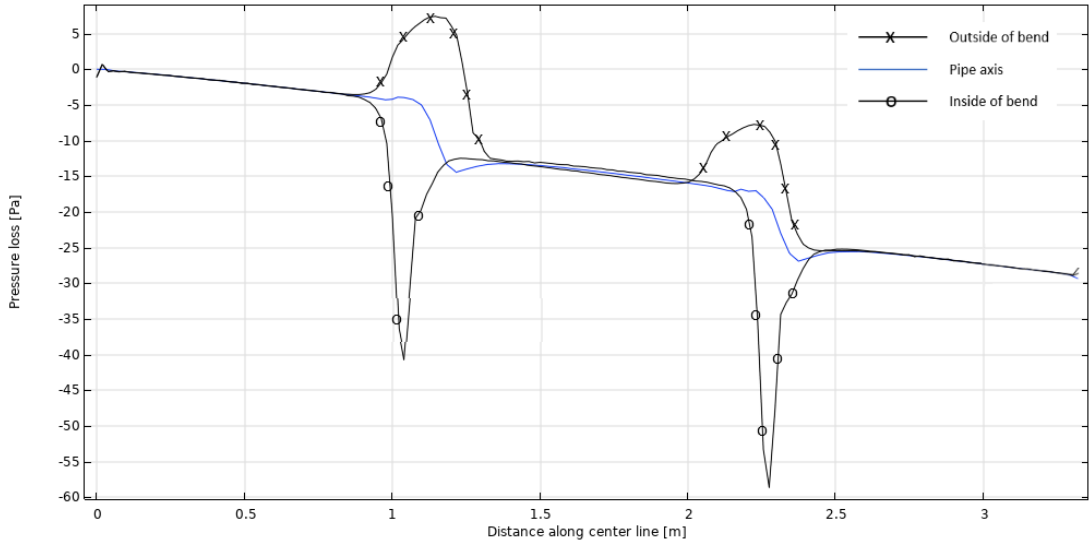

Figure 31: Pressure drop [Pa] along the inside, outside and pipe axis of the bends of an S-bend configuration with a separation distance of 1 m. Within the bends, the pressure increases on the outside and decreases on the inside.

The pressure drop in each pipe section can be analysed separately by measuring the pressure and velocity at the beginning and end of each section using a surface average. The end of one pipe section is the beginning of the next section. The results for several pipe sections of an S-bend with a separation distance of 1 m, inlet and outlet pipes of the same length and bends with an R/d of 1 are presented in Table 7, where the pipe sections are identified as previously shown in Figure 18. The K-value for each section can then be calculated using Equation 19. In Table 7, the K-value of each section is shown, where the values of the two bends are quite similar. The K-values of the straight sections are very different, even though the pipes have the same diameter, length and roughness value of 50 µm. The velocities differ a bit, but the main difference is observed in the pressure drop along these pipe sections, 5.042, 7.279 and 5.747 Pa for pipes 1, 2 and 3, respectively.

The average velocity in all pipe sections of the COMSOL simulation is $0.20\,\mathrm{m\,s^{-1}}$ and to be able to compare the results, this velocity is used for all pipe sections in the MATLAB model. The values from the MATLAB model are also tabulated in Table 7, where first, the head loss is given in [mm] and the K-value is calculated using Equation 19. It can be seen that the computed K-value in the bends is much higher as computed for the COMSOL model (0.390 vs. 0.236 and 0.198). The K-value for pipe 1 is also higher, but for pipes 2 and 3 the value is again lower. The total

K-value of the COMSOL simulation is 1.41 and that of the MATLAB model is 1.60. A difference in K-values of 0.19 is observed, which can be attributed to the influence of the first bend on the flow in second bend, as will be explained in the next section. The MATLAB model thus overestimates the losses for this separation distance.

Table 7: Determination of K-values using COMSOL and MATLAB for different pipe sections of an S-bend configuration with a separation distance of 1 m, of which the pressure drop can be seen in Figure 30. The total K-value of all pipe sections is calculated to be 1.41 for the COMSOL simulations and 1.60 for the MATLAB model.

	Comsol						Matlab	
Pipe section	P_{begin}[Pa]	P_{end}[Pa]	ΔP [Pa]	V_{begin}[m s^{-1}]	V_{end}[m s^{-1}]	K-value	Head loss [mm]	K-value
Pipe 1	29.098	24.056	5.042	0.200	0.200	0.255	0.556	0.273
Bend 1	24.056	18.206	5.850	0.200	0.205	0.237	0.796	0.390
Pipe 2	18.206	10.927	7.279	0.205	0.200	0.401	0.556	0.273
Bend 2	10.927	6.098	4.829	0.200	0.204	0.198	0.796	0.390
Pipe 3	6.098	0.352	5.747	0.204	0.200	0.315	0.556	0.273

10.4.2 Varying separation distance

In this proximity study, it will be concluded if and to what extend the separating distance influences the pressure loss. In parallel, conclusions will be drawn up to which separating distance the two bends can be treated as isolated, such that the pressure loss caused by the bend combination will be equal to twice that of an isolated bend [45]. A parametric sweep is performed in COMSOL, where the separation distance was varied across: 0.1, 0.25, 0.5, 0.75, 1.0, 2.0, 3.0, 4.0, 5.0, 7.5 and 10 m. To further understand the relationship between the pressure loss caused by the S-bend and separation length, additional simulations were run with separation distances of: 1.2, 1.4, 1.6 and 1.8 m. Figure 32 shows the pressure loss as a function of the distance along the pipe axis for every option, and the shape of each line is the same as in Figure 30. As can be seen, when the separation distance is between 2 and 10 m, the additional pressure loss within pipe 2 due to the increasing length lies on a straight line, as expected from Equation 8. The trend line in Figure 30 shows this linear behaviour and is drawn at the pressure dip after the second bend for visibility (instead of directly at the line of pressure drop in pipe 2). From this figure, it can be seen that if the separation distance becomes less than 2 m, this is no longer valid and the graphs don't follow the behaviour from the trend line anymore. The pressure loss is less after the first bend and in pipe 2 for these separation distances.

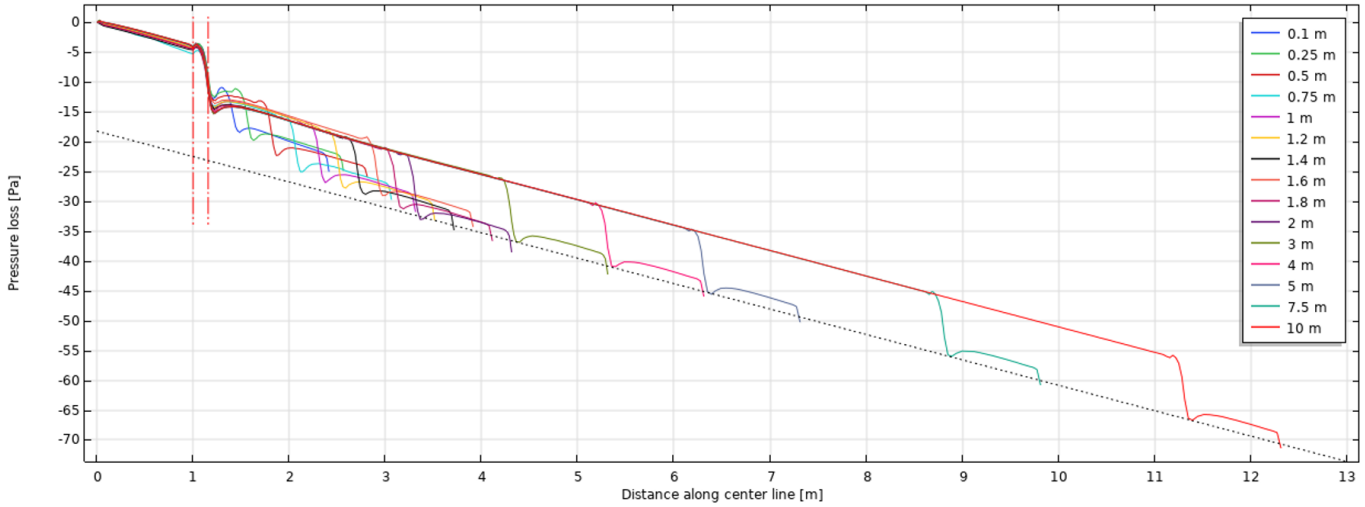

Figure 32: Pressure drop along S-bend with varying separation distances. The beginning and end of the first bend are indicated with the red dotted lines. A linear trend line is drawn.

Figure 33 shows a zoomed-in version of Figure 32 where the pressure drop can be observed better for separation distances smaller than 2 m. Again, the trend line is drawn. Here, it can be clearly seen that the pressure drop of these S-bend configurations is less than twice that caused by an isolated bend with a separating pipe, as the trend line indicates. As indicated in the figure with the arrows, the behaviour of the S-bends follows more of a curve when the separating distance is less than 2 m.

For a bend to be considered isolated, it must receive a fully developed flow and there must be sufficient downstream length to let the flow return to a fully developed state [45]. For bend 1, the first criterion is satisfied, however, it should be studied if there is indeed sufficient downstream length, i.e. length of pipe 2, to let the flow return to a fully

developed state before it reaches bend 2. In the next chapter, the fluid phenomena that are present in a single bend are discussed, after which it is linked to the interaction of two bends which are separated by some distance.

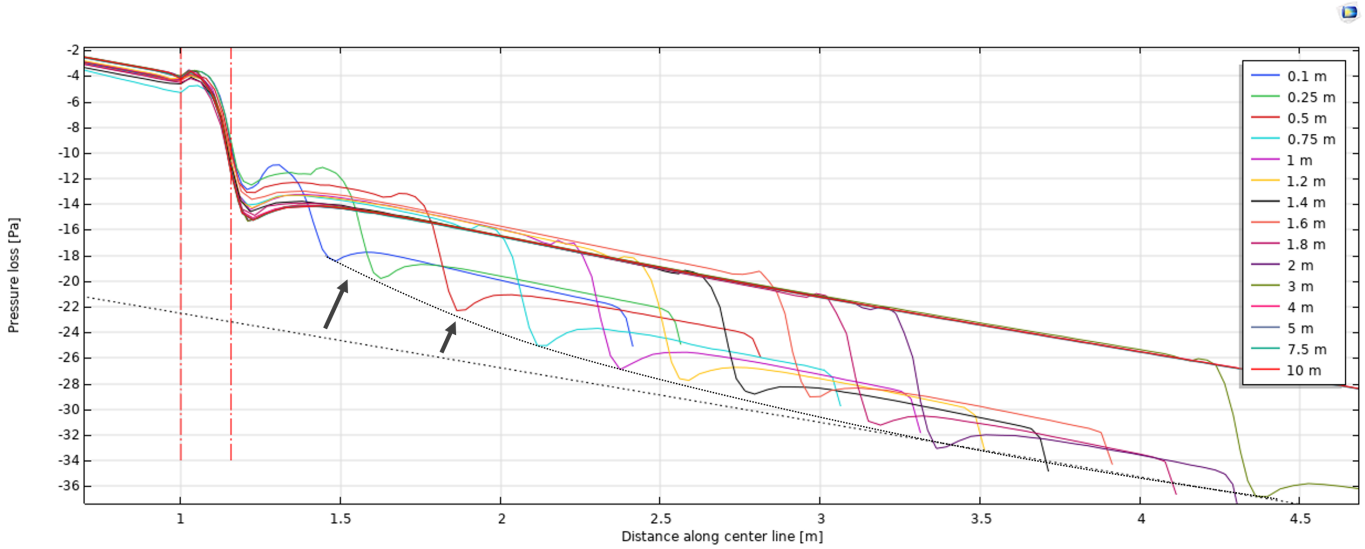

Figure 33: Zoomed-in version of Figure 32, where the behaviour of the S-bends follows more of a curve when the separating distance is smaller than 2 m

If the same geometry, flow velocity and wall roughness are inserted into the MATLAB model, for which the governing equations are discussed in Section 8, the results can be compared. The MATLAB model uses a flow rate as input, which can be calculated using Equation 3 using a flow velocity of $0.2\,\mathrm{m\,s^{-1}}$ and a pipe diameter of 0.1 m. The pressure loss for each separation distance can be converted to head loss using Equation 9. Figure 34 shows the head loss from the COMSOL simulations, as well as the head loss calculated with the MATLAB model. Overall, good agreement is found between the results, however, the head loss calculated with the COMSOL simulations are all slightly below the results from the MATLAB model. The graph from the MATLAB model shows a straight line for all separation distances. In this graph, it becomes also clear that above a separation distance of 2 m, the head loss shows linear behaviour for the COMSOL simulations. Below this distance, this behaviour is not visible.

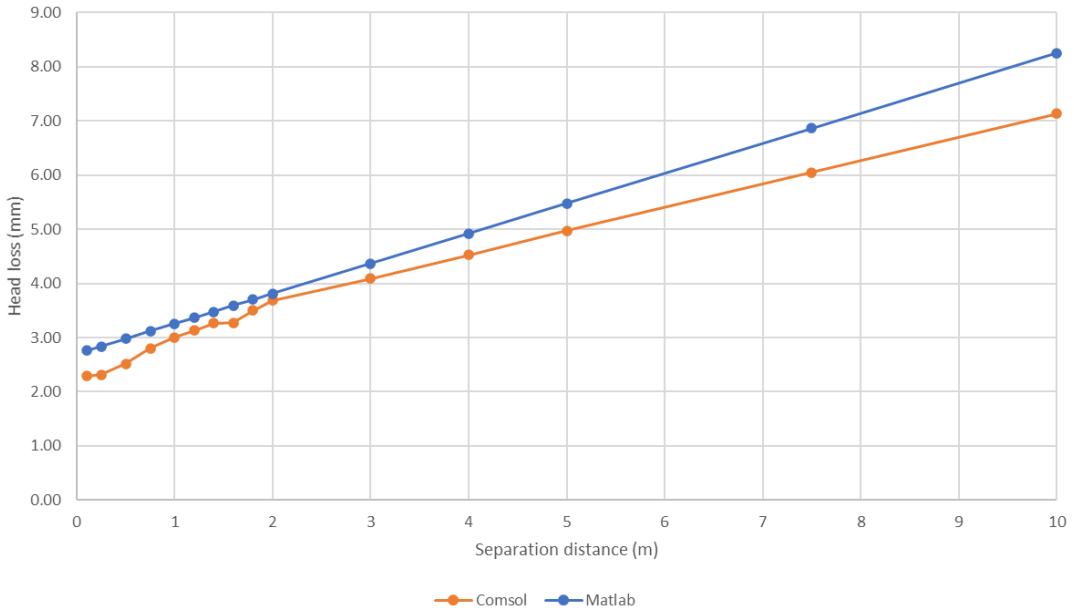

Figure 34: Head loss (mm) from the COMSOL simulations and MATLAB model for the S-bend configuration for different separation distances (m). The MATLAB model shows linear behaviour over the full range of separation distances. The COMSOL simulations show linear behaviour above a separation distance of 2 m.

10.4.3 Single-bend phenomena

To explain the pressure loss trends as observed in Figures 32 and 33, first, the flow phenomena caused by a single isolated bend will be presented and discussed. Next, an attempt is made to explain the interaction between two bends separated by some distance. For simplicity, only 90° bends will be taken into consideration.

As a fluid flows through a single 90° bend, there will be a localized deceleration of the flow at the outer wall resulting in a pressure increase since the flow is steady and incompressible [32, 45, 46, 47] as can be seen in Figure 35a, where the flow direction is from the bottom of the pipe to the top left (reversed direction compared to the simulations). At the inner wall, the fluid is accelerated resulting in a pressure decrease. This behaviour was also shown previously in Figure 31. This region of high axial velocity, or velocity of the primary flow, moves from the inner wall at the bend entrance to the outer wall at the bend exit [38]. In this process, a secondary flow, consisting of two counter-rotating vortices that are symmetric about the bend plane, in which fluid near the bend plane moves toward the outer wall and fluid away from the bend plane moves toward the inner wall, is generated at roughly 30° into the bend [45, 46, 47]. This secondary flow is perpendicular to the main flow direction [38, 44, 48], and is superimposed on the primary flow due to the combined action of centrifugal force and frictional resistance of the pipe walls [19]. These vortices are also called Dean vortices and can be seen in Figure 35b. A fluid particle in this flow moves downstream along a helical path [46]. This distortion of the flow results in a pressure loss in the bend and downstream of the bend as viscous forces restore the flow to a fully developed state.

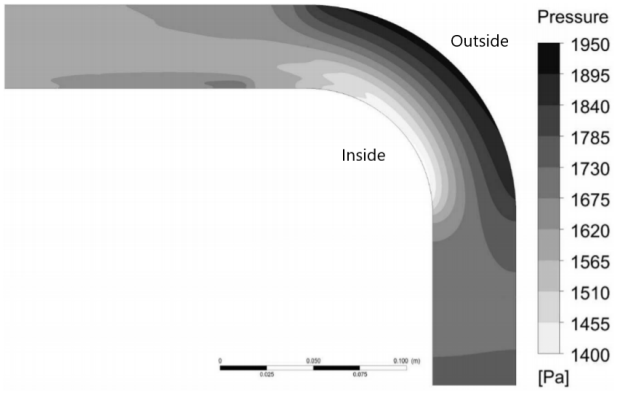

(a) Pressure contours shown in the bend symmetry plane (bend plane) of an isolated bend for Re = 5×10^4 where fluid flows from the bottom right to the top left. Figure adapted from Ref. [45].

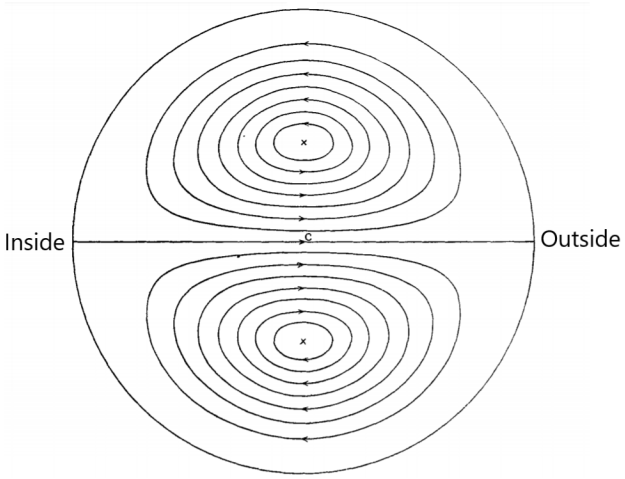

(b) Schematic overview of Dean vortices as sectional streamlines in the cross-sectional plane of the bend. The middle line is the bend symmetry plane. Figure adapted and modified from Ref. [49].

Figure 35

To further examine the behaviour of a fluid flowing through a bend, the axial velocity, or velocity of the primary flow, and velocity vectors of secondary flow at successive longitudinal cross-sections upstream, within and downstream of a 90° bend can be plotted. Figure 36 shows only part of the S-bend configuration, indicating the cross-sectional locations at which the primary and secondary velocity profiles will be analysed. The longitudinal distance is denoted by z and a negative fraction of z/D indicates a cross-sectional plane upstream of the bend and a positive fraction indicates a plane downstream of the bend. ϕ indicates the angle of the cross-sectional plane within the bend. Figure 38 shows the axial velocity and velocity vectors of secondary flow at these cross-sectional planes.

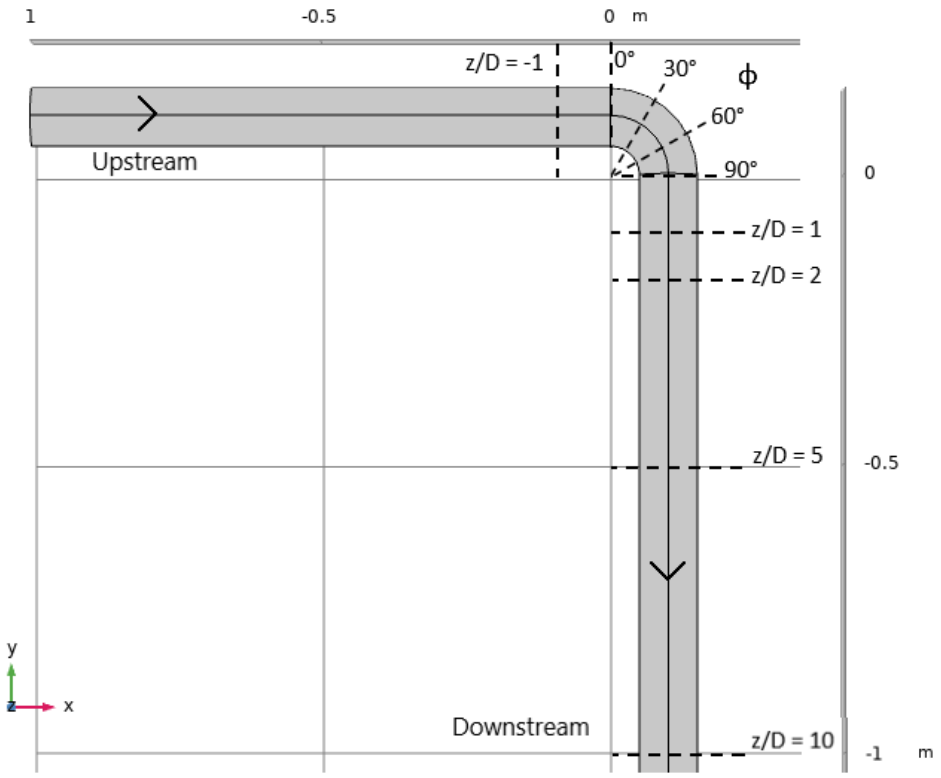

Figure 36: Locations on the upstream straight section (negative z/D, where d is the pipe diameter), in the bend at different bend angles ϕ and at the downstream straight section (positive z/D), which are used for the results in Figure 38.

In Figure 38, the axial velocity in all plots share the same legend as shown in the figure and the arrows indicate the secondary flow, of which the size is proportional to the velocity vectors. The plots are generated for the same S-bend configuration as in the S-bend proximity study, with a separation distance of 2 m and adapting all the other settings. Only the first bend of this configuration is analysed. From the figure, at z/D = -1, it becomes clear that the flow is not yet influenced by the bend, even though the velocity profile is not fully circular. This is due to the coarse mesh that is applied in this study to decrease the computation time. No secondary flow is visible yet. Figure 37 shows the mean flow velocity contours at z/D = -1 when the mesh would be changed to fine, increasing the computation time of the simulation from 9 minutes to 50 minutes. As shown, the velocity profile is more circular, even showing a slightly higher velocity at the center. The mesh thus influences the results slightly, however, a single simulation takes much longer. If the same mesh was used for all fifteen simulations in Section 10.4, the computation time would increase from just over 2 hours to 12.5 hours.

In Figure 38, at the inlet plane of the bend, at $\phi = 0°$, the fluid is accelerated to the inside of the bend and the flow at the outside of the bend is decelerated, this behaviour is also seen in the secondary flow profile. At $\phi = 30°$, the secondary flow profile as shown in Figure 35b appears in the cross-section and it forms two counter-rotating vortices. Its strength is, however, not high and the fluid with fast axial velocity still moves near the inner wall of the bend, which is also observed by Sudo et al. [47]. At $\phi = 60°$, the faster fluid near the inner wall is transported towards the outer wall through the central region of the cross-section by the secondary flow. Also, the slower fluid near the outside wall is convected towards the inner wall side along the wall by the secondary flow and creates a very distinct region. At $\phi = 90°$, the fast fluid conveyed to the outer wall is carried towards the inner wall by the secondary flow moving inwards along the wall. This results in greatly distorted velocity contours which have the shape of a crescent moon at $z/d = 1$ and enclose the low-velocity region near the inner wall. The low-velocity fluid moves towards the central region of the pipe. The velocity of the fluid near the inner wall increases as the secondary flow convects fluid towards that region. From $z/D = 2$ to 10, the secondary flow weakens, and the longitudinal velocity starts returning to a smoother profile by frictional effects. However, a further longitudinal distance is required for the flow to exhibit a fully developed flow profile, as it was before the bend. Overall, the conclusions drawn from Figure 38 are in agreement with the conclusions drawn by Sudo et al. [47], which concluded that in the inlet region of the bend, the primary flow accelerates near the inner wall and a secondary flow moving from the outer to the inner wall of the bend occurs in the bend cross-section. Also, at $\phi = 30°$ in the bend, the secondary flow develops into a pair of vortices, as seen in fully developed curved pipe flows, but the primary flow remains deflected toward the inner wall. Between $\phi = 75°$

and 90°, the velocity contours of primary flow are greatly distorted and a depression in the contour plot is formed in the inner part of the bend cross-section. At successive downstream stations, the distribution of primary flow velocity gradually becomes smooth. The secondary flow weakens and vortices break down. They concluded that the influence of the bend on the flow, however, remains even at $z/D = 10$.

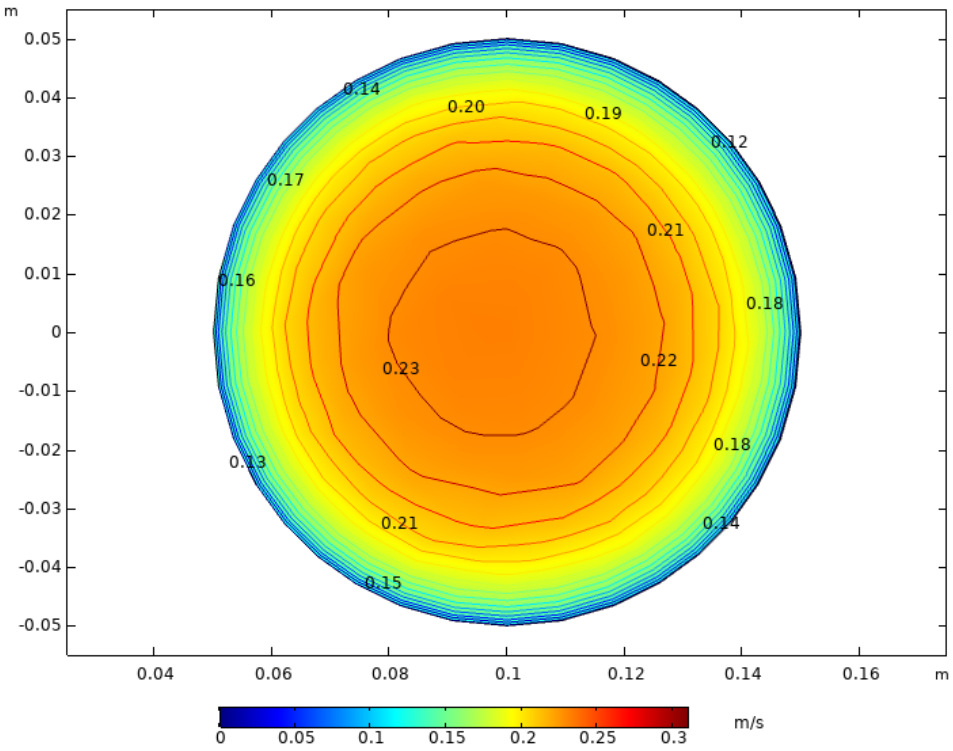

Figure 37: Mean flow velocity contours at z/D = -1 for a fine mesh.

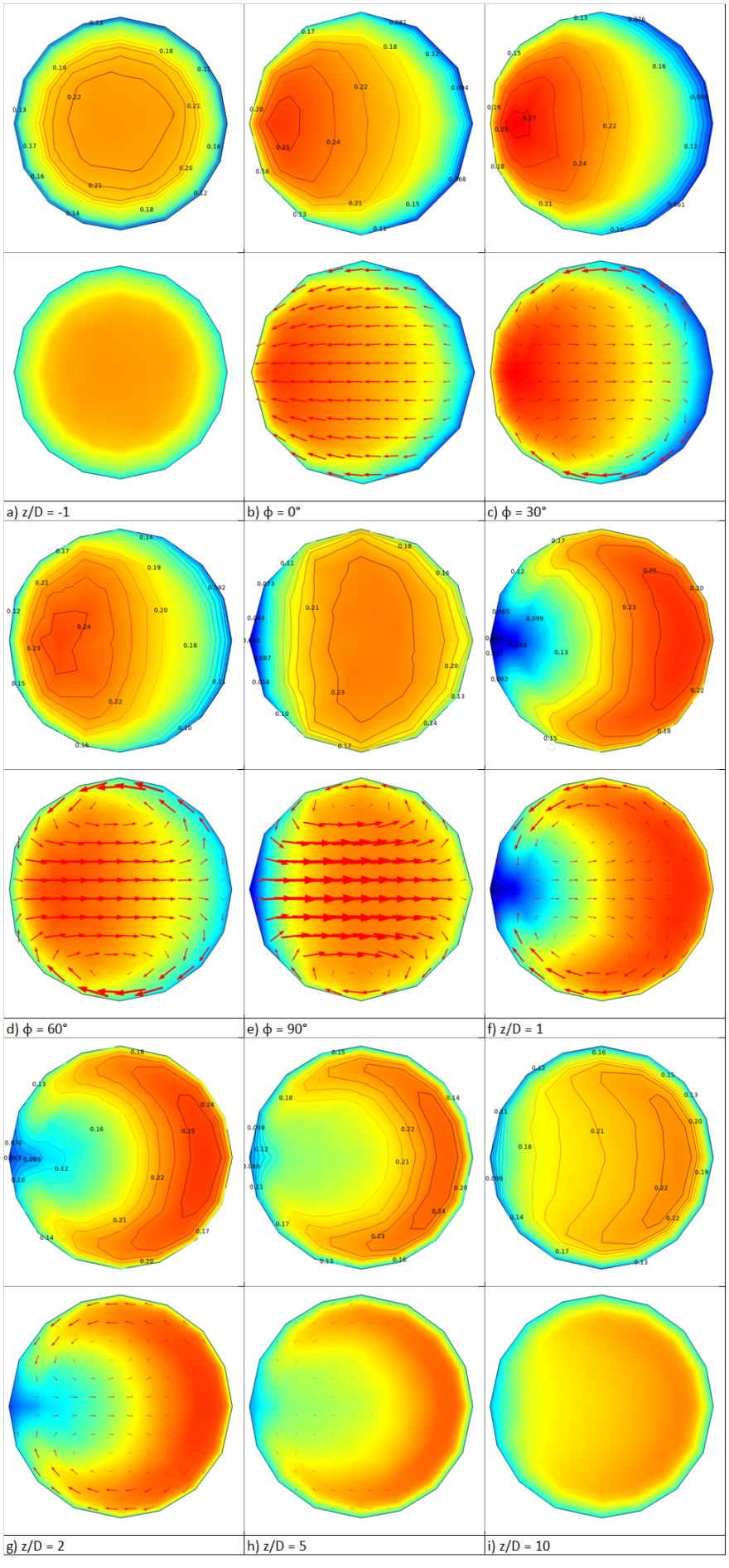

Figure 38: Mean flow velocity contours for locations on the upstream straight section (negative z/D, where d is the pipe diameter), in the bend at different bend angles ϕ and in the downstream straight section (positive z/D). Streamwise velocity contours (top) and secondary flow velocity vectors (bottom). The left and right sides of each figure show the inside and outside walls in the bend, respectively.

10.4.4 S-bend combination phenomena

Previous results showed that a separation distance less than 20 pipe diameters between the bends resulted in a pressure loss that was lower than the equivalent uncoupled bends, whereas separation distances greater than 20 diameters yielded the same pressure loss as for uncoupled bends. Petersen et al. [45] state that for separation distances slightly smaller than the transition point, in our case 2 m, the pair of secondary vortices generated by the first bend continue to exist along the outer wall of the downstream tangent of the second bend. The outer wall is thus the wall connected to the outside of the second bend and the inner wall is connected to the inside of the second bend, as shown in Figure 39. The figure also shows the new vortices that are generated in the second bend. As the region of high axial velocity moves from the inner wall at the entrance of the second bend toward the outer wall at the exit of the second bend, these vortices exist along the inner wall. As the two pairs of vortices from both bends move downstream of the second bend, the vortices along the inner wall, in which fluid near the bend plane moves toward the outer wall, absorb the smaller vortices along the outer wall. They also show that for decreasing separation distances, the vortices near the outer wall (generated in bend 1) start dominating those near the inner wall (generated in bend 2), until only the vortices on the outer wall exist. In this case the fluid near the bend plane moves toward the inner wall, contrary to what has been shown before for a single bend, where the fluid moves from the inner to the outer wall. This is due to the increased strength of the incoming secondary flow, and the favourable pressure gradient for fluid near the bend. It should be noted that the preceding explanation of the pressure losses is proposed by Petersen et al. [45] as no prior investigation [47, 50, 51] has proposed an explanation for the observed differences in pressure losses caused by varying the intermediate length. Their research is fairly recent and has not been cited much and therefore a widely accepted explanation of the previously described behaviour still awaits.

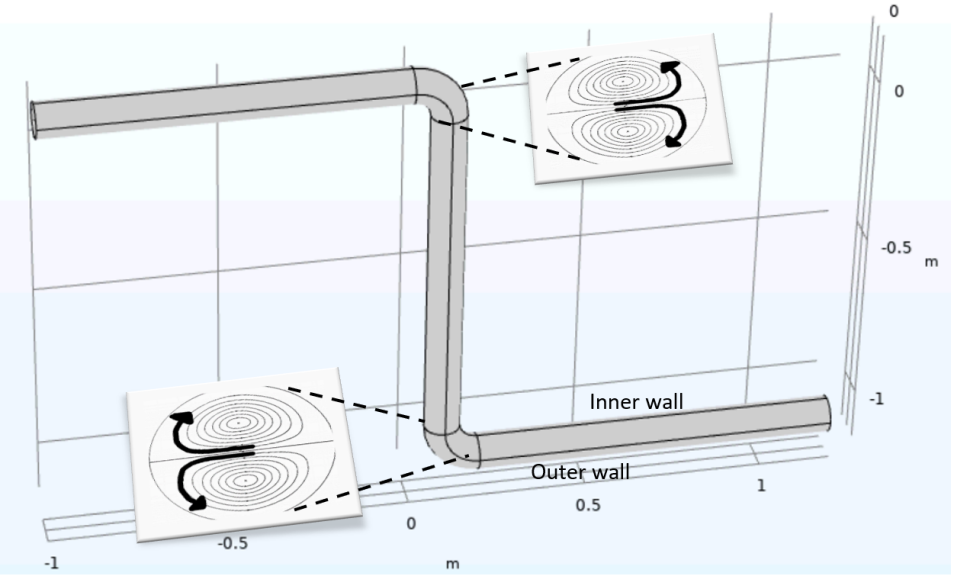

Figure 39: Overview of the S-bend configuration with the generation of pairs of vortices in each bend. The two pairs rotate in opposite directions. The inner wall indicates the wall connected to the inside of bend 2, and the outer wall is connected to the outside of bend 2, at the bottom.

Sami and Cui [50] developed a numerical method in ANSYS to calculate the pressure loss coefficients from multiple pipe elbows arranged in different close-coupled configurations and spaced apart at different distances. A flow of water at room temperature through pipes with a diameter of 5.08 cm and bends with a radius over diameter ratio of 1 are used. Their numerical results confirmed the conclusion from the experimental observations by Rahmeyer [51]: the loss coefficient for bends at a large separation distance (20 pipe diameters) is approximately equal to the loss coefficient of the same number of uncoupled bends, while the loss coefficient for fittings with small separation distance (less than 20 pipe diameters) is less. For small separation distances, the acceleration created by the first bend does not have enough space to adjust itself before it encounters the second bend and changes further in the downstream pipe.

A very extensive and well-cited study by Sudo et al. [47] showed the same plots as was shown in Figure 38 at $\mathrm{Re} = 6 \times 10^4$, using pipes with a diameter of 10.4 mm, a bend radius over diameter of 2 and an airflow with a mean velocity of $8.7\,\mathrm{m\,s^{-1}}$. Petersen et al. [45] performed numerical simulations using ANSYS to investigate the pressure losses caused by two-bend combinations. Two in-plane bend combinations, having a "U" and "S" shape, and an out-of-plane bend combination were examined. A flow of water through pipes with a diameter of 4.47 cm, a bend radius over diameter of 2 for Reynolds numbers of 2×10^5, 5×10^4, and 1×10^4 was studied. They concluded that for the "U" combination, the two-bend pressure loss decreased monotonically as the separating distance decreased. For the "S"

and out-of-plane configurations, the pressure loss was at a minimum when the separating length was between three and five pipe diameters.

The results presented here are obtained using Comsol simulations of water flowing through pipes with a diameter of 10 cm, a bend radius over diameter of 1. Both Sudo et al. [47] and Petersen et al. [45] found a minimum pressure loss for the S-bend configuration when the intermediate length is between three and five diameters, an effect which was not strongly present in the results presented here. The observed trends from the Comsol simulations follow the conclusions of Sami and Cui and Rahmeyer well, where the loss coefficient for bends at a large separation distance is approximately equal to the loss coefficient of the same number of uncoupled bends, while the loss coefficient for fittings with small separation distance (less than 20 pipe diameters) is less.

Overall, similar pressure loss trends would be observed for different bend combination parameters such as Reynolds number and radius over diameter of the bends. The results presented here can be used to qualitatively predict the behaviour in bends and bend combinations.

11 Loss analysis current design buried Ocean Battery

The current design of the buried Ocean Battery is made by the Ocean Grazer B.V. in late June 2021. It is expected by the stakeholders of this project, as mentioned in Section 2.1, that the losses within the pipes will be low. This would mean that the major and minor losses have a low effect on the overall roundtrip efficiency of the battery. This is, however, not yet verified using experiments, simulations or analytical models.

In previous chapters, several pipe junctions were studied under conditions that may or may not represent real operating conditions of the Ocean Battery. In this chapter, real operating conditions will be applied to the current design, where a 3D Comsol model and the Matlab model will be used to study the losses. First, the operating conditions, i.e. flow rates in both charging and discharging mode, are discussed. Next, the 3D Comsol with its boundary conditions is explained. Finally, the pressure loss analysis using both Comsol and Matlab is performed and compared.

11.1 Operating conditions

Firstly, it should be determined for which flow rates the pressure loss will be analysed. As explained in Sections 7.1 and 7.2, the flow rates of the pump and the turbine are interconnected with the losses in the pipes. To save time, we start with a predefined flow rate that comes close to the real flow rate and calculate the parameters that are needed to model the flow and losses.

For the current design of the buried Ocean Battery no pump-turbine, motor, generator and transformers are selected yet. As a result, no information can be deducted from a pump-performance curve or turbine efficiency-flow rate curve. However, it is estimated that each pump-turbine will have a rated power of 200 kW. The pump efficiency η_p and the turbine efficiency η_t are taken to be 95%. It is estimated that this value resembles the BEP of both the pump and turbine, as both can be optimised for the operable head. The efficiencies of the transformer and motor are also taken to be constant, with values of 99% and 98%, respectively. The generator has a constant efficiency of 98%.

In the current design of the buried Ocean Battery, the average hydrostatic head is somewhere between 50 and 100 m, based on the buried depth and the sea height. The rigid reservoir has a height of 10 m, so if the average hydrostatic head is for example 75 m, the available hydrostatic head fluctuates between 70 and 80 m. This is because the water level in the rigid reservoir changes due to charging and discharging of the system and therefore the height difference between the sea water level and the water level in the rigid reservoir changes.

Table 8 gives the flow rates of the pump, in charging mode, and the turbine, in discharging mode, for three values of the average hydrostatic head of 50, 75 and 100 m by using the corresponding maximum and minimum hydrostatic head for each case. One or more pump-turbines can be turned on in operation, but here only the case where the maximum number of 8 pump-turbines are in operation is considered due to time restrictions. The design of the buried Ocean Battery implies that the flow is split into multiple flows when multiple pump-turbines are in operation. If 8 pump-turbines are in operation, the total flow rate is eight times the flow rate of a single pump-turbine.

The water temperature is taken to be 20°, which sets the value of ρ to $998.2\,\mathrm{kg\,m^{-3}}$ [20]. The flow rates of the pump are calculated using Equation 28 and the flow rates of the turbine are calculated using Equation 29, both for the minimum and maximum head available for each case. One example calculation, for a minimum head of 45 m is given by:

$$Q_p = \frac{8 * 200\,000 * 0.99 * 0.98 * 0.95}{998.2 * 9.81 * 45} = 3.347\,\mathrm{m^3\,s^{-1}} \qquad Q_t = \frac{8 * 200\,000}{998.2 * 9.81 * 45 * 0.99 * 0.98 * 0.95} = 3.939\,\mathrm{m^3\,s^{-1}}$$

The flow rate in the pump or charging mode is between 1.434 and $3.347\,\mathrm{m^3\,s^{-1}}$ for eight pumps. The flow rate in the turbine or discharging mode is between 1.688 and $3.939\,\mathrm{m^3\,s^{-1}}$ for eight turbines. The flow rates in turbine operation, as mentioned in Table 8, can be verified by comparing them to head-discharge charts for general turbines. Comparing the calculated values to those mentioned in literature shows good agreement [18, 35, 52].

Table 8: Flow rates of the pump Q_p, in the charging mode, and flow rate of the turbine Q_t, in discharging mode for the minimum and maximum head for three cases of the available average hydrostatic head between 50 and 100 m for the buried Ocean Battery. These values are calculated for a single pump-turbine.

Pump-turbines	Average head [m]	Hydrostatic head [m]	Q_p [$\mathrm{m^3\,s^{-1}}$]	Q_t [$\mathrm{m^3\,s^{-1}}$]
8	50	45	3.347	3.939
		55	2.738	3.223
	75	70	2.151	2.533
		80	1.882	2.216
	100	95	1.585	1.866
		105	1.434	1.688

The flow rates mentioned in Table 8 are used as boundary conditions in the COMSOL simulations and as input values for the MATLAB model. To be able to compare results between different values of available hydrostatic head, the pressure loss or head loss is expressed as a fractional loss of the total available hydrostatic pressure or hydrostatic head:

$$P_{L,perc} = \frac{h_L}{h_{hydro}} * 100\% = \frac{\rho g h_L}{\rho g h_{hydro}} * 100\% = \frac{P_L}{P_{hydrostatic}} * 100\%. \tag{42}$$

11.2 3D Comsol model

The 3D COMSOL model of the current design of the buried Ocean Battery is based on the design given in Figure 4 and design specifications given by Marijn van Rooij. The model includes all pipe sections between the rigid and flexible reservoir, excluding these reservoirs themselves. The pump-turbines are very difficult to simulate and would increase the computation time a lot and are therefore not taken into account. As can be seen in the design in Figure 4, reinforcement walls are placed in the large vertical pipe. Adding these in the model would greatly increase the complexity, mainly the meshing, as there are a lot of corners that require a fine mesh and are therefore left out. Also, the connection to the reservoirs is made straight instead of with pipe bends.

Figure 40 shows the COMSOL model of the current design, where the pressure loss analysis is performed separately on the top part and the bottom part. The pump-turbines separate both parts. The top part consists of four pipes that are connected to the flexible reservoirs (1), the large vertical pipe (2) and the conical enlargement (3) below. Eight small vertical pipes (4) will connect the pump-turbines to the top and bottom parts. The collection container (5) at the bottom is connected to the rigid reservoirs by four pipes (6). Both top and bottom parts use half of the pump-turbine connection pipe length (4).

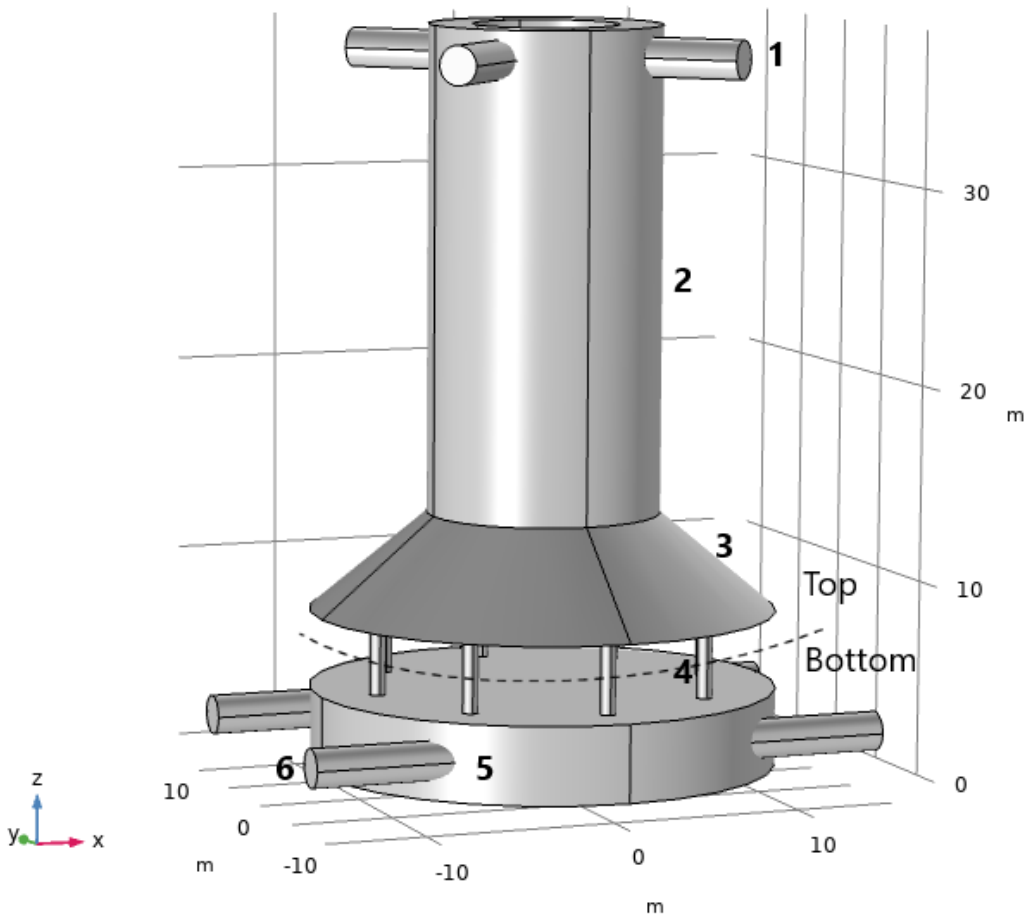

Figure 40: 3D COMSOL model of the current design of the buried Ocean Battery. The design is split up in a top and bottom part, as the pump-turbines are not modelled.

The dimensions of the geometry shown in Figure 40, is shown in Table 9. A user-controlled mesh is applied to the full geometry, where a finer mesh calibrated for fluid dynamics is applied to the vertical pipe such that the connections

to other pipes are properly meshed. A fine mesh is applied to the remainder of the geometry. The mesh parameters can be seen in Table 10. As can be seen, the user is free to choose which mesh is applied to which part of the geometry, however, the mesh parameters itself are not changed. Therefore, some differences are present between both fine meshes, as COMSOL changes these parameters depending on the geometry and physics.

For both parts, a pressure point constraint is used, as only flow rates are used as boundary conditions. The exact location of this constraint does not influence the results, as only the difference in pressures from the simulations is used and not the values themselves. This difference will remain the same if the value or position of the pressure point constraint is varied.

Both the top and the bottom parts will be analysed using the flow rates from Table 8. When using the pump flow rates, the fluid flows from the rigid reservoir to the flexible reservoir. For the bottom part, the inlets are located at the pipe connections to the rigid reservoir (6) in Figure 40 and the outlets at the pump pipe connections (4). For the top part, the flow rates are applied as an inlet boundary condition to the pump pipes. The outlet boundary condition is then applied to the flexible reservoir connection pipes. For the turbine operation, the turbine flow rates are used and the inlet/outlets are reversed.

Table 9: Dimensions of the current design, as used to generate the geometry in the COMSOL model as shown in Figure 40.

Pipe description (number in Figure 40)	Length or height (m)	Diameter (m)
4 pipe connections to flexible reservoir (1)	L = 5	2
Vertical pipe (2)	H = 25	Inner D = 7.5 m, outer D = 12 m
Conical enlargement (3)	H = 5	Top D = 12 m, bottom D = 24 m
8 pump-turbine pipe connections (4)	H = 4	0.8
Collection container (5)	H = 4	24
4 pipe connections to rigid reservoir (6)	L = 7.5	2

Table 10: Mesh parameters of the COMSOL model of the current design, as shown in Figure 40.

Part of model	Calibrated mesh	Maximum element size	Minimum element size	Maximum element growth rate	Curvature factor	Resolution of narrow regions
Top, vertical pipe	Finer	0.888	0.096	1.1	0.4	0.9
Top, remainder	Fine	1.27	0.24	1.13	0.5	0.8
Bottom	Fine	0.636	0.12	1.13	0.5	0.8

11.3 Loss analysis using Comsol

The pressure loss analysis performed with the model from Section 11.2 is discussed in this section. The top and bottom parts of the model are simulated using the aforementioned flow rates, a pressure point constraint is used for convergence and the realizable k-ϵ turbulence model is used. The pressure loss is divided into the losses in the top and bottom parts. To calculate the pressure loss, one cannot simply calculate the pressure difference between the rigid and flexible reservoirs and the pump-turbines, as the diameter of the pipes varies, the fluid velocity and pressure change. Therefore, the pressure and velocity are both calculated using a surface average, as was done before. For the top part, this surface average is taken over the surfaces of the flexible reservoir pipe connections and at a cut plane which is located 1 m below the conical enlargement (through the pump-turbine connection pipes), as can be seen in Figure 41a. For the bottom part, a surface average is taken over a cut plane located 1 m above the collection container. In this way, there is some room for the pump-turbines between the cut planes of the top and bottom parts. The final surface average is taken over the surfaces of the rigid reservoir pipe connections, as can be seen in Figure 41b.

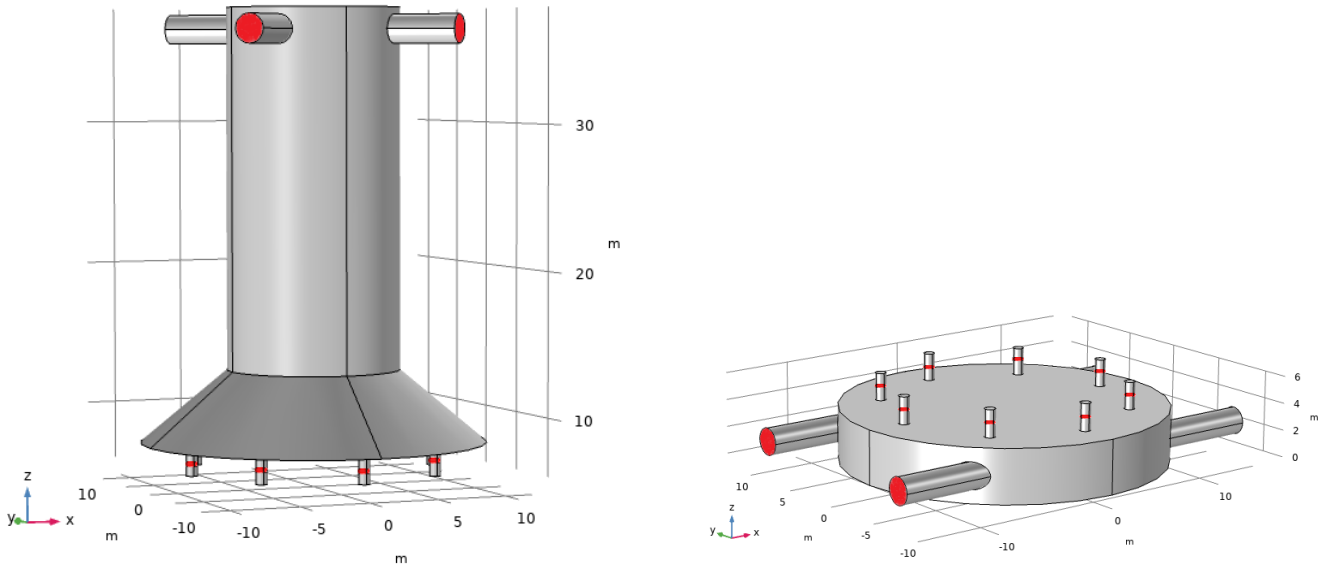

(a) (b)

Figure 41: Surfaces and cut planes over which the velocity and pressure are extracted using a surface average.

When the maximum of 8 pump-turbines are in operation, the flow rates in Table 8 are used as boundary conditions. The flow direction through the Ocean Battery needs to be taken into account in the simulations. An attempt was made to simulate the fluid flow in the charging and discharging mode, using the flow rates of the pump and turbine, respectively. When the fluid flows from the flexible to the rigid reservoir (discharging mode, turbine flow rates), no problems were observed and the models were able to converge to a solution. Unfortunately, the Comsol simulations where the fluid flows from the rigid to the flexible reservoir (charging mode, pump flow rates) were not able to converge. An attempt was made to solve this problem by making the mesh of the whole geometry finer, using a different solver type (direct and fully coupled instead of segregated) and by changing the location of the pressure point constraint. The simulations were performed using the Peregrine high-performance cluster at the University of Groningen, of which a manual is written by E. Neven [53]. None of the proposed solutions has resulted in the convergence of the models. Therefore, the flow rates of the pump and the turbine are all used to model the fluid flow in the turbine operation.

Table 11 shows the calculated total head loss, total pressure loss and total fractional loss of the measurements for the full geometry, where the results of the top and bottom parts have been summed. The raw data of the velocities and pressures calculated at the planes for the separated top and bottom parts are tabulated in Tables 18 and 19 in Appendix C.3. The head loss is calculated using Equation 6, the pressure loss using Equation 9, and the fractional loss with Equation 42. The average head, head and flow rate are extracted from Table 8. As can be seen, as the flow rate decreases, the total loss decreases. This is as expected, because when the flow rate is lower, the fluid velocity through the pipes is lower. Both the major and minor head loss are quadratically dependent on the fluid velocity (Equations 8 and 18, respectively). As also shown, the maximum fractional loss of the total available hydrostatic pressure is only 0.266% for a flow rate of $3.939\,\mathrm{m^3\,s^{-1}}$ for 8 operational turbines. These results show that low losses in the piping system of the current design of the buried Ocean Battery can be obtained. It should be noted, however, that this model is simplified in multiple ways and gives therefore only an indication of the losses. It is expected that the pump and turbine will influence the fluid flow significantly due to the rotary motion inside, which will results in an increase in losses. Another part of the design that was omitted in the simulations are the reinforcement walls in

the large vertical pipe. Due to the addition of this geometry, the fluid is not able to flow freely inside the large vertical pipe and the conical enlargement. Disturbances in the fluid cannot restore the way they can in the simulation.

Table 11: Head loss, pressure loss and loss as a fraction of the total available hydrostatic head for the current design of the buried Ocean Battery. Only simulations for the discharging mode are performed due to convergence problems in the charging mode.

Average head [m]	Head [m]	Q [$m^3 s^{-1}$]	H_L [m]	P_L [Pa]	Fractional loss [%]
50	45	3.939	0.120	1170.9	0.266
	45	3.347	0.086	846.4	0.192
	55	3.223	0.080	785.1	0.146
	55	2.738	0.058	567.3	0.105
75	70	2.533	0.050	485.8	0.071
	70	2.151	0.036	350.8	0.051
	80	2.216	0.038	372.2	0.048
	80	1.882	0.027	268.9	0.034
100	95	1.866	0.027	264.3	0.028
	95	1.585	0.020	191.1	0.021
	105	1.688	0.022	216.5	0.021
	105	1.434	0.016	156.6	0.015

11.4 Loss analysis using Matlab

To analyse the losses using the MATLAB model, as discussed in Section 8, the current design is split up into all separate pipes. All pipes, including their dimensions, are shown in Table 9. Besides these pipes, also exits and entrances should be taken into account. The model then uses the corresponding K-values and the flow rate to calculate the losses. When the flow flows through 4 separate pipes, the flow rate in each pipe is a quarter of the total flow rate. Also, the model is only able to calculate the losses when a fluid flows through the whole pipe. The large vertical pipe of 25 m high and the conical enlargement below are hollow in the middle and can therefore not be analysed using the model, as no K-value is specified for such a geometry. To still include these sections in the analysis, the results of the COMSOL model for these sections is used.

Table 12 gives an overview of all the separate parts that are used as input in the MATLAB model. A pipe roughness of 50 µm is used for all pipes, which resembles stainless steel (see Table 14). For each pipe section, the fraction of the total flow rate through it is denoted.

The head loss is calculated separately for each part for the maximum flow rate of $3.939\,m^3\,s^{-1}$ and also shown in Table 12. The total head loss is 0.63 m, which gives a fractional loss of 1.4%. As can be seen, the contribution of the 8 straight edged entrances and exits connected to the pump-turbine connection pipes largely influences the head loss. These pipes have a much smaller diameter (0.8 m) than the pipe entrances and exits at the top and bottom (2 m), and thus the fluid velocity is much higher, resulting in higher losses.

Table 12: Pipe input for the MATLAB model, in combination with the values mentioned in Table 9. The head loss is calculated separately for the pipes for a flow rate of $3.939\,m^3\,s^{-1}$, which is in total 0.63 m.

Pipe description (top to bottom)	Fraction of total flow rate	Note	Head loss (m)
4 pipe connections to flexible reservoir	0.25		0.00065
4 exits	0.25		0.02004
Vertical pipe	N/A	From Comsol	0.00015
Conical enlargement	N/A	From Comsol	
8 straight edged entrances	0.125		0.19567
8 pump-turbine pipe connections	0.125	L = 1 m	0.00647
8 pump-turbine pipe connections	0.125	L = 1 m	0.00647
8 exits	0.125		0.39133
4 straight edged entrances	0.25		0.01002
4 pipe connections to rigid reservoir	0.25		0.00098

11.5 Comparison of results

Before discussing the differences in results for the current design, we should look at the differences between the MATLAB model and the COMSOL simulations. In the simulations, the geometry is discretized into small cells, which is called meshing. The mesh then defines the number of calculation points [53]. Increasing the number of computation points (making the mesh finer) increases the accuracy, but also increases the computation time. Besides the mesh, also appropriate boundary conditions, such as flow rate and a pressure point constraint are important to get convergence, as well as the solver type. COMSOL uses the RANS equations together with a turbulence model to solve for example the fluid velocity, pressure and energy dissipation. After solving, plots of these quantities in 3D or 2D are available. Also a lot of other plots, such as pressure drop along a pipe section can be made using 1D graphs. Therefore, to thoroughly study effects in fluid flow through pipes, COMSOL provides the user with a lot of options.

In MATLAB, however, a model is developed which is only able to calculate the losses in simple pipe sections. A set of equations is used to do this, and by using the fluid flow rate, pipe length, diameter and roughness, the user can quickly analyse the losses. For the minor losses, the model is highly dependent on the values of the minor loss coefficient K that are mentioned in literature and adapted in the model. In reality, pipe sections that are placed close to each other can influence the flow in such a way that these sections cannot be treated separately. This effect was studied in Section 10.4, but is incorporated into MATLAB.

The results of the head loss and fractional loss of the current design of the buried Ocean Battery show that there are some differences between COMSOL and MATLAB. The head loss was calculated to be 0.12 m and 0.63 m for a flow rate of $3.939\,\mathrm{m^3\,s^{-1}}$ for the COMSOL simulations and MATLAB model, respectively. This means a huge difference in head loss of 0.51 m. The head loss calculated with COMSOL is only 19% of that calculated with the MATLAB model. Possible explanations for this difference have been discussed before. The head loss, calculated with the MATLAB model, is largely influenced by the 8 straight edged entrances and exits connected to the pump-turbine connection pipes. Besides, it cannot yet be concluded if one of the two resembles real-world behaviour better, and to do so, experiments should be conducted to validate the simulated and calculated losses.

The roundtrip efficiency of Ocean Battery can be determined by dividing the output energy by the input energy, but also by multiplying the efficiencies of all components. An overview of the components used in charging and discharging mode can be seen in Figure 3. The final efficiency is thus obtained by multiplying the efficiency of the transformer (99%), the motor (98%), the pump (95%), twice the efficiency of the pipes (99.7% for COMSOL and 98.6% for MATLAB, the turbine (95%), generator (98&) and the final transformer (99%). For the COMSOL model a roundtrip efficiency of 84.5% is obtained, and for the MATLAB model an efficiency of 82.6% is obtained. This is all under the assumption of fixed efficiencies of all components of the Ocean Battery.

12 CFD analysis Ocean Battery Prototype

During the summer of 2021, a prototype of the deep water version of the Ocean Battery has been tested in the harbour of the Eemshaven. Tests with this prototype have shown that the Ocean Battery holds great potential for storing renewable energy. In this section, a COMSOL model will be used to analyse the losses in a pipe section of the prototype. If the experimental results are in line with the simulations, this further supports the use of COMSOL CFD simulations to analyse losses in pipe flow. First, a short introduction is given about the prototype, after which the data gathering, including sensor placement, is discussed.

12.1 Deep water prototype

Figure 42 shows part of the piping system of the Ocean Battery deep water prototype. Only the section between the flexible reservoir and the sensor in front of the turbines (2) is shown, as again, the turbines will not be modelled due to their complexity. There are two sensors that measure the head, which are indicated with a red dot. One sensor is placed right outside the pipe connection to the flexible bladder, at the bottom of the flexible bladder (indicated with transparent plane), as also can be seen in Figure 43. The second one is placed at the pipe wall on the turbine input side.

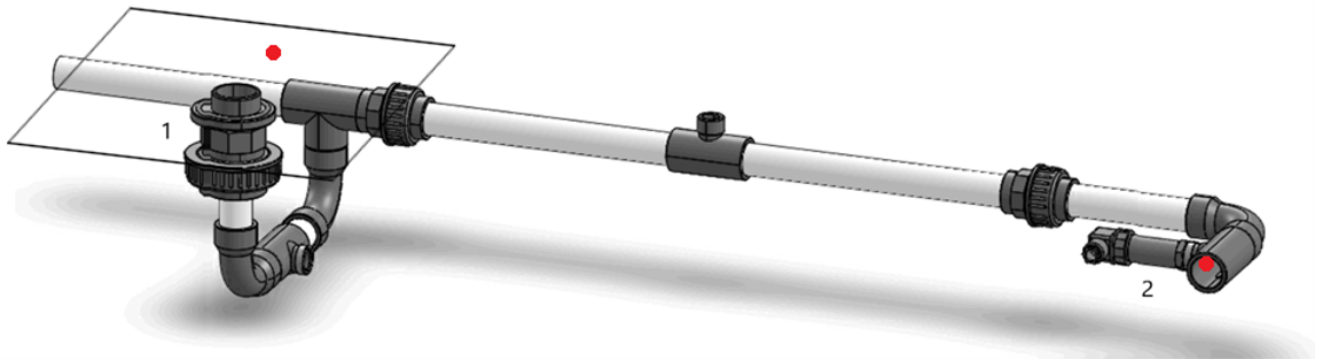

Figure 42: Part of the piping system of the prototype of the deep water version of the Ocean Battery. (1) pipe connection to flexible reservoir (2) turbine input sensor. The red dots indicate the sensor placement in the flexible bladder and at the turbine input side.

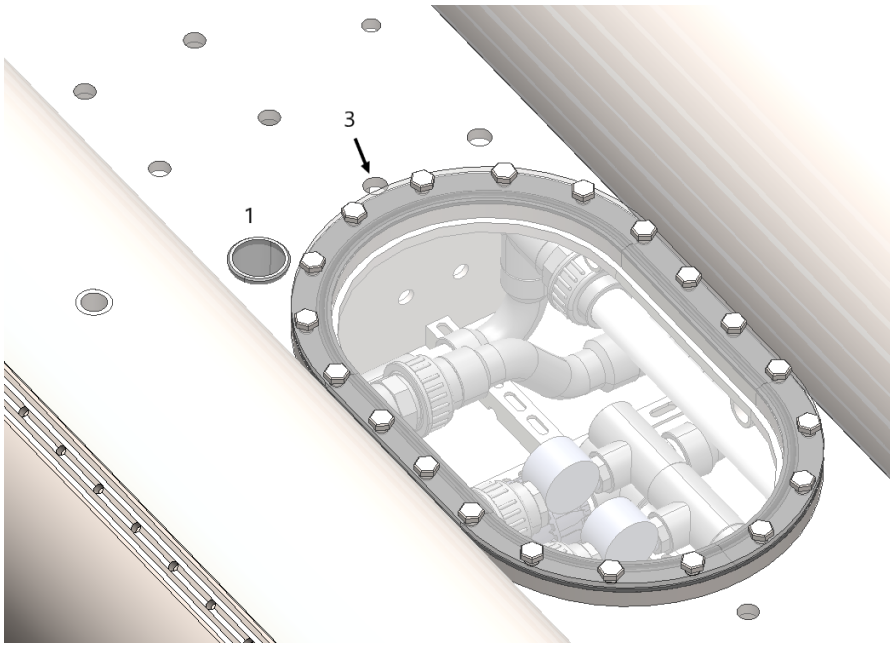

Figure 43: Sensor placement in the flexible reservoir, next to the pipe connection. (1) pipe connection to flexible reservoir (3) sensor.

For the measurements with the prototype in the Eemshaven, a ball valve has been opened around 65 s after the measurements started, such that the fluid flows through the pipes and has been closed again after 675 s. Both sensors have measured the hydrostatic head in [m], and part of the original gatherered data can be seen in Table 20 in Appendix D, where only measurements every 5 s are shown, but the original data set contains measurements every 10 ms.

To calculate the head loss from the measurement with the prototype, Equation 6 can be rewritten into:

$$h_L = Z_{fb} + \frac{P_{fb}}{\rho g} + \frac{V_{fb}^2}{2g} - Z_{turb,in} - \frac{P_{turb,in}}{\rho g} - \frac{V_{turb,in}^2}{2g}, \tag{43}$$

where the subscripts fb and $turb, in$ denote the sensor in the flexible bladder and the turbine input, respectively. The flexible bladder sensor is located 96 mm higher than the turbine input sensor. Therefore, $Z_{turb,in}$ is taken to be the reference level and is therefore 0 m, which puts Z_{fb} at 96 mm. Also, the velocity in the flexible bladder V_{fb} is taken to be 0, as it is such a large volume. Also, the terms including pressure can be rewritten into H_{fb} and $H_{turb,in}$, which denote the hydrostatic head measurements in the flexible reservoir and the turbine input, respectively. Therefore, Equation 43 can be written as:

$$h_L = Z_{fb} + H_{fb} - H_{turb,in} - \frac{V_{turb,in}^2}{2g}. \tag{44}$$

The fluid only flows for part of the measurement and therefore only the measurements between 100 and 600 s are considered. The average flow rate for this part of the data is determined to be $0.000\,297\,\mathrm{m^3\,s^{-1}}$. The average head at the flexible reservoir and turbine inlet are calculated and inserted in Equation 44, which gives an average head loss from the experimental measurements of:

$$h_L = 96 * 10^{-3} + 3.269838 - 3.288865 - \frac{0.000297^2}{(0.25 * \pi * D^2)^2 * 2g} = 0.064\,\mathrm{m}, \tag{45}$$

where $V_{turb,in}$ is calculated using Equation 3 and D denotes a pipe diameter of 0.0272 m. The head loss h_L is therefore calculated to be 0.064 m in the pipe section between the flexible reservoir and the turbine inlet.

12.2 Comsol model

Figure 44 shows the 3D Comsol model of part of the pipe system of the prototype, as was shown in Figure 42. Part of the flexible reservoir is added as a large box on top. The realizable $k - \epsilon$ turbulence model is used with an inlet flow rate of $0.000\,297\,\mathrm{m^3\,s^{-1}}$ at the top of the large box, and the outlet is located at the right. A fine mesh calibrated for fluid dynamics is used on the whole geometry. Also a pressure point constraint is used at the outlet.

The same procedure for calculating the head loss as previously shown is applied here. The pressure and fluid velocity are calculated at the same two measurement points as in the prototype itself. It is estimated from Figure 43 that the sensor in the flexible reservoir is located 10 cm from the pipe inlet. The measurement point at the turbine inlet is placed at the pipe wall. Both measurement points can be seen in Figures 45 in Appendix C.4.

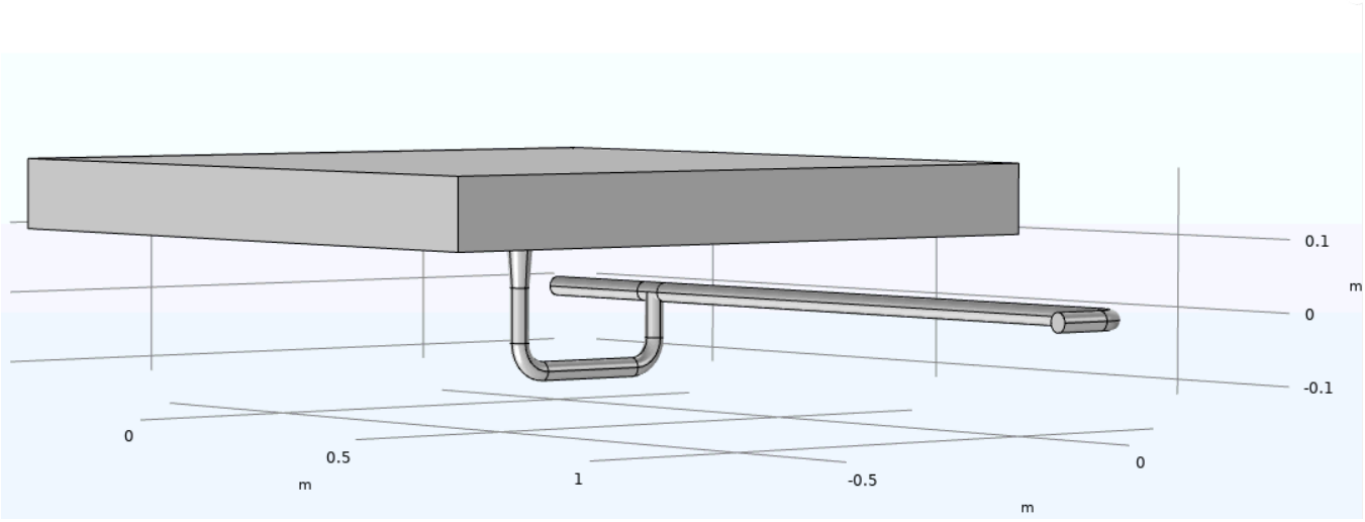

Figure 44: 3D Comsol model of the Ocean Battery deep water version prototype.

The pressure difference between the flexible reservoir and the turbine inlet is calculated to be 745 Pa and the velocity increase is calculated to be $0.375\,\mathrm{m\,s^{-1}}$. The height difference between the measurement points is already accounted for by measuring the pressure at both points as pressure minus hydrostatic pressure. Filling in these numbers into Equation 6 gives the average head loss of:

$$h_L = \frac{745}{(998.2)(9.81)} - \frac{0.375^2}{2(9.81)} = 0.069\,\mathrm{m}. \tag{46}$$

This process shows that an accurate estimation of the head loss can be calculated using a simplified COMSOL model. There is, however, a small difference of 0.005 m, or 7.8%, between the measured average head loss (0.064 m) with the simulated average head loss (0.069 m), which can be attributed to the simplified geometry in the COMSOL model. Also, taking the averages of the measurements with the prototype results in some small deviations, but overall, this shows that CFD simulations can predict the losses with an acceptable error and are a viable tool to analyse the losses before experiments are performed.

13 Discussion

In the theory section, it was observed that the equations to calculate the major losses in pipe flow for both the laminar and turbulent region are around for a few decades now and have proven themselves over time. There are multiple approximations to determine the turbulent friction factor, with the Serghide approximation found to be very accurate over a wide range of surface roughness values and Reynolds numbers. This provides a good basis for the analytical MATLAB model. However, the determination of the minor losses in pipe junctions, where additional turbulence is present due to the pipe shape, is not as straightforward. For almost all pipe junctions, being it a bend, contraction, expansion or pipe inlet or outlet, it was found that there exists no unambiguous value for the minor loss friction factor K or equation to determine the head loss h_L. The K-values used in the MATLAB model highly influence its outcome and the model is therefore highly dependent on their magnitude. In literature, only K-values of simple pipe geometries are mentioned, and more complex pipe geometries can therefore not be analysed using the model.

In this study, the efficiencies of the pump, turbine, motor, generator and transformers are all taken to be constant. Evaluating the pipe flow losses for a single flow rate using constant efficiencies is a viable approach, as the pump and turbine both can be tuned to work optimally for a specific flow rate. However, in the full round trip of the Ocean Battery, also start-up and shutdown effects are present, which results in different flow rates. These effects have not been taken into account to ensure that the computation time of the analytical model is kept short, as otherwise the model becomes more complex and needs to recalculate the volumes of both reservoirs during either charging or discharging mode.

The fluid flow rate is one of the main inputs for the MATLAB model. If a pipe configuration includes branching or a combination of multiple pipes, the total flow rate remains the same. The flow rates in the separate pipes are then a fraction of the total flow rate. These pipe sections should therefore be analysed separately using the appropriate flow rate. In the current design of the buried Ocean Battery this approach is used multiple times, where, for example, the flow in the large vertical pipe is split up into four pipes to the flexible reservoir. The flow rate in each of these pipes is then a quarter of the total flow rate.

Simulating fluid flow using CFD in COMSOL is done by solving the RANS equations in combination with a turbulence model. Each turbulence model has its strengths and weaknesses as was shown, and the final results will depend on the model choice. The realizable $k-\epsilon$ model was chosen as it showed similar results in terms of pressure and velocity as the $k-\omega$ and v2-f models, where the SST model showed some differences. The computation time of the model was 50% of the computation time of the $k-\omega$ model and 33% of the v2-f model, and only 17% of the SST model. It is important to minimise the computation time while retaining the models' quality and accuracy. Also, the realizable $k-\epsilon$ turbulence model includes the option to use wall roughness, resembling real pipes even more.

It was also shown that using the Bernoulli equation for conservation of energy, the head loss or K-value of a pipe section can be calculated. To do so, the pressure and fluid velocity are measured in front and after the pipe section. This approach can be used in experiments, but is applied here to the COMSOL simulations. It was shown that the location of these measurement points within the pipe highly influences the outcome. Therefore, for the COMSOL simulations, instead of using two measurement points, two surface averages are used to mitigate these effects. In reality, however, the pressure and velocity are measured using sensors, which only measure at a specified location. The placement of these sensors is therefore crucial for the outcome.

Using COMSOL, it was studied if and to which extent pipe junctions, and in particular pipe bends, can be treated to be isolated when placed close to each other. The MATLAB model uses the number of pipe bends as an input parameter and then calculates the total head loss as if a bend does not influence the flow in another bend. This study shows that below a specific separation distance, two bends are indeed of influence on each other. For the boundary conditions and geometry presented here, this critical separation distance was found to be 2 m. When two bends are placed closer to each other than this separation distance, the total loss is found to be less than when the two bends are treated to be isolated. It is therefore hypothesised that this critical separation distance is a function of the fluid velocity and pipe diameter, however, no further attempt was made to investigate this.

For a single isolated bend, it was found that the influence of the bend on the fluid flow was present even at ten pipe diameters downstream of the bend. Depending on the fluid velocity and pipe diameter, the distance before the disturbances in the flow are fully restored varies. The secondary flow profile in and after a single bend was studied to show the movement of the fluid before it returns to a fully developed flow. This study follows the conclusions from Sudo et al. [47], which show that the COMSOL simulations presented here correctly show real-world behaviour of pipe flow through bends.

The fluid flow in the current design of the buried Ocean Battery was simulated using a simplified geometry. Real operating conditions were simulated by first calculating the fluid flow rates for the pump and turbine for a specific

hydrostatic head. For the maximum simulated flow rate of $3.939\,\mathrm{m^3\,s^{-1}}$ the head loss was found to be 0.12 m for a system with a hydrostatic head of 45 m. This means that the loss as a fraction of the total available hydrostatic head is 0.266%, which shows that the current design of the Ocean Battery holds great potential for energy storage. Any additional losses due to start-up processes, rotating parts in the turbine and pumps or due to deformation of the flexible bladder are not taken into account. It was also found to hard to get convergence with the COMSOL simulations. There are a lot of options that can be tuned in COMSOL, such as solver type, mesh size and boundary conditions, which all can influence the converge of the model and influence the computation time.

The losses in the current design have also been analysed using the analytical MATLAB model. For the same flow rate of $3.939\,\mathrm{m^3\,s^{-1}}$, the head loss was calculated to be 0.63 m, which results in a loss as a fraction of the total available hydrostatic head of 1.4%. The calculations in the model only take a few seconds and this is many factors less than the computation time of a single simulation in COMSOL, which was found to be around 35 min. It should be noted, however, that the MATLAB model cannot evaluate all pipes of the current design. The large vertical pipe and the pipe enlargement which are both hollow in the middle cannot be evaluated directly as no K-value is present for both geometries. To still evaluate the full design, the losses of both pipe sections are extracted from the COMSOL model and added to the remainder of the losses calculated with the MATLAB model. The head loss calculated from the COMSOL simulations is only 20% of that calculated with the MATLAB model. The losses from the model are largely influenced by the 8 straight edged entrances and exits connected to the pump-turbine connection pipes, which only have a diameter of 0.8 m. The model is highly dependent on the values of the minor loss coefficient K that are mentioned in literature and this influences the outcome of the loss analysis.

Finally, a CFD analysis using COMSOL was performed for a pipe section of the deep water prototype of the Ocean Battery. It was shown that using a simplified geometry and an average flow rate from the experiments of $0.000\,297\,\mathrm{m^3\,s^{-1}}$, the head loss was calculated to be 0.069 m. The experimentally determined average head loss of 0.064 m differs only by 0.005 m, meaning a 7.8% difference. This shows that CFD simulations can predict the losses with an acceptable error and are a viable tool to analyse the losses before experiments are performed.

14 Conclusion

In order to make an estimation of the roundtrip efficiency of the buried Ocean Battery, an analysis of the losses in pipe flow is required. The roundtrip efficiency is best analysed using full-sized experiments with the buried Ocean Battery. Unfortunately, this is not possible, yet, due to the huge dimensions of the system, but also because the design is not yet finalised. The goal of this thesis was to develop a validated model that can aid the design of the buried Ocean Battery based on the efficiency of different pipe configurations. This process is supported by studying the hydrodynamic behaviour and the mechanics that influence the fluid flow through these pipes. Additional research was performed using Comsol simulations of separate pipe sections, in which loss coefficients were extracted and compared to theoretical values. Also the current design of the buried Ocean Battery is analysed using Comsol simulations and using the Matlab model. Finally, a 3D Comsol model is made to analyse the head loss in a pipe section of the deep water prototype to further support the use of Comsol CFD simulations to analyse losses in pipe flow.

First, it was studied how fluid flow and losses can be modelled using a set of equations. Losses in pipe flow are subdivided into major and minor losses, where the former deals with frictional losses due to the interaction of the fluid with the pipe walls, and the latter deals with additional turbulence in a fluid due to the pipe shape. The energy that resides in the turbulence is generally lost as heat. Major losses, and especially the Darcy friction factor, can be calculated accurately as was shown in literature. Minor losses can be calculated if the minor loss friction factor K of that pipe section is known. For a specific pipe junction, it was found that, in literature, there exists no unambiguous value for the minor loss friction factor K or equation to determine the head loss h_L. As such, the K-values used in the Matlab model highly influence its outcome and the model is therefore highly dependent on these values.

Comsol simulations of separate pipe sections were analysed to determine to what extent the minor loss coefficients are comparable between literature and the simulations. It was found that the CFD simulations underestimate the theoretical K-values somewhat, and as these theoretical values are based on experiments, it can be concluded that the simulations underestimate real losses. If preferred, experiments on pipe sections can be performed to support this hypothesis. Overall, fluid flow through pipes can be complex, however, the mechanics behind fluid flow through a bend is studied in more detail. It was found that due to the redirection of the flow by the bend, more turbulence is present in the flow. A secondary flow is imposed on the primary flow which results in two counter-rotating vortices. This behaviour is not only present within the bend but can be observed even at ten pipe diameters after the bend.

The analytical Matlab model is based on a set of equations that calculates the losses in a pipe configuration for a specified flow rate and water temperature. The flow rate is determined based on the hydrostatic head, i.e. the sea depth and buried depth, and the efficiencies of the pump, turbine, generator, motor and transformer. The main parameters that will influence the losses in the pipes deal with the pipe geometry, thus pipe length, diameter and roughness. For bends the bend angle and radius over diameter, thus sharpness of the bend, are important. The main parameter that influences the magnitude of the losses is the fluid velocity, which is determined by the fluid flow rate and the pipe diameter. The Matlab model calculates the losses for a specified number of pipe sections by treating every pipe section as it is isolated. In this study, also the interaction of pipe sections, and in particular the interaction of two bends, is studied with Comsol. This study shows that below a specific separation distance, two bends are indeed of influence on each other. For the boundary conditions and geometry presented here, this critical separation distance was found to be 2 m. When two bends are placed closer to each other than this separation distance, the total loss is found to be less than when the two bends are treated to be isolated. It is hypothesised that this critical separation distance is a function of the fluid velocity and pipe diameter.

The current conception of the losses in the buried Ocean Battery design is that these will remain low. As the pipe diameters are very large, the fluid velocity remains low in all pipes. A low velocity means low frictional losses between the working fluid and the pipe walls. This expectation is supported by both the Comsol simulations and the outcome of the Matlab model. The simulations show a maximum loss of 0.266% of the available hydrostatic head for a flow rate of $3.939\,\mathrm{m^3\,s^{-1}}$. The Matlab model gives a loss of 1.4% for that flow rate. There are some differences between both, however, it shows that the buried Ocean Battery holds great potential for storing energy. The difference can be explained by looking at the way both calculate the losses. The analytical model uses a set of equations with input parameters and fixed friction coefficients, the K-values. It can occur that complex geometries, such as present in this design, cannot accurately be described by the equations given in literature and cannot be evaluated using the Matlab model. Comsol simulations provide more freedom, but this comes at a cost of a much higher computation time, where the analytical model calculates losses within a couple of seconds and the simulations easily take up more than half an hour.

An important design consideration of the analytical model is that it does not only work for the current design, but also when the design changes. Input parameters can be changed such that different pipe configurations can quickly

be analysed, but also the hydrostatic head, water temperature and flow rate can be changed in the model.

In this study, some things have been left out of the scope of the project or are taken as an assumption. First of all, no pump or turbine was modelled in COMSOL as fluid flow and behaviour is very complex, not only within but also after a pump or turbine. Previous studies have shown that a reversible Francis pump-turbine is an appropriate choice and future studies can look into the effects of a pump-turbine on the disturbances in the flow, but also if the speed or size of the propeller shows any effects on the flow. Also, it should be investigated if a draft tube is necessary for a pump-turbine combination. A draft tube is generally used behind a turbine to increase the pressure to mitigate the effects of back flow of the fluid.

Also, the current design of the buried Ocean Battery was analysed using a constant flow rate, but no attempt was made to simulate a full roundtrip of the battery, where startup and shutdown effects play a role and the flow rate varies in time. This would increase the complexity of both the MATLAB model and the COMSOL simulations.

After this research, it became clear that MATLAB is not as powerful as COMSOL in analysing fluid flow through more complex geometries. A trade-off should therefore be made for future studies, as a MATLAB model can quickly analyse a pipe system, but is limited to what is denoted in theory, whereas the COMSOL model has much more options, which do come at a cost of higher computation time and possible convergence issues. These COMSOL models can be studied again in future research to solve the problem of convergence, as COMSOL provides so much more tools to analyse flows not only through pipes, but also through pump-turbines and reservoirs.

To support further development of the Ocean Battery as a product it is advised to use rounded edges for pipe connections. As was shown in the current design, all pipes are connected by straight-edged entrances, which have a higher K-value and thus higher loss than a rounded edge. Also, the transition of a smaller diameter pipe to a larger pipe or container (or the other way around) can be made more gradual, as losses for sudden enlargements and contractions are higher than for their gradual equivalents.

Finally, for future research, when the Ocean Battery is deployed on a location within a sea, usually tides are present that cause the rise and fall of the sea water level. This leads to a change in hydrostatic head on the battery, increasing or decreasing the hydrostatic pressure. For the operation of the battery, this behaviour should also be taken into account, as the energy storage capacity depends on the hydrostatic pressure. A high tide means higher hydrostatic pressure and higher energy storage, and also lead to a lower flow rate of the turbine, which then decreases the losses within the pipes.

References

[1] M. S. Javed, T. Ma, J. Jurasz, and M. Y. Amin, "Solar and wind power generation systems with pumped hydro storage: Review and future perspectives," *Renewable Energy*, vol. 148, pp. 176–192, 4 2020.

[2] N. Mousavi, G. Kothapalli, D. Habibi, M. Khiadani, and C. K. Das, "An improved mathematical model for a pumped hydro storage system considering electrical, mechanical, and hydraulic losses," *Applied Energy*, vol. 247, pp. 228–236, 2019.

[3] T. van Kessel, "Simulation of the energy flow of an offshore energy storage system," January 2020, Bachelor Project IEM.

[4] G. Notton, M.-L. Nivet, C. Voyant, C. Paoli, C. Darras, F. Motte, and A. Fouilloy, "Intermittent and stochastic character of renewable energy sources: Consequences, cost of intermittence and benefit of forecasting," *Renewable and Sustainable Energy Reviews*, vol. 87, pp. 96–105, 2018.

[5] M. Simao and H. M. Ramos, "Hybrid pumped hydro storage energy solutions towards wind and pv integration: Improvement on flexibility, reliability and energy costs," *Water*, vol. 12, no. 9, 2020.

[6] Ocean Grazer, "Storing Renewable Energy at Sea, Info Flyer."

[7] J. Bromlewe, "Optimization of the flow and efficiency model for the Ocean Battery," January 2021, Bachelor Integration Project.

[8] M. M. Rahman, A. O. Oni, E. Gemechu, and A. Kumar, "Assessment of energy storage technologies: A review," *Energy Conversion and Management*, vol. 223, p. 113295, 2020.

[9] M. Mahmoud, M. Ramadan, A.-G. Olabi, K. Pullen, and S. Naher, "A review of mechanical energy storage systems combined with wind and solar applications," *Energy Conversion and Management*, vol. 210, p. 112670, 2020.

[10] Rehman, S., Al-Hadhrami, L. M., and Alam, M. M., "Pumped hydro energy storage system: A technological review." Renewable and Sustainable Energy Reviews, 44:586–598, January 2015.

[11] J. S. R. Groenenberg, J. Koornneef *et al.*, "Large-Scale Energy Storage in Salt Caverns and Depleted Fields (LSES) – Project Findings," Online, 10 2020, TNO Report. [Online]. Available: https://repository.tno.nl/islandora/object/uuid:668d330c-1abe-4fc3-b191-d2741a2e6a78

[12] Ocean Grazer B.V. company, "Ocean Battery." [Online]. Available: https://oceangrazer.com/

[13] ——, "Ocean Grazer - Ocean Battery - A scalable, reliable, and ecofriendly energy storage solution." [Online]. Available: https://www.youtube.com/watch?v=S7pY3i9UJxc

[14] S. van Rijn, "Designing and modelling the performance of Ocean Grazer battery prototype B," June 2020, Master Thesis EES.

[15] M. Been, "CFD Analysis Rigid Reservoir," March 2021.

[16] L. Pasqualini, "Comparison of Different Engagement and Dispatch Protocols applied to the Units Responsible of Charging and Discharging an Ocean Battery System: Simulation-based Study to Evaluate the Efficiency and Performance of the System," January 2021, Master Thesis TU Delft.

[17] K. Niekolaas, "Revenue maximization of distributed Ocean Battery systems through Model Predictive Control," March 2020, Master Thesis.

[18] N. M. Serrat, "Design and analysis of the Engine Reservoir of the Buried Ocean Battery," University of Groningen, December 2020, Master Design Project ME.

[19] D. C. Rennels and H. M. Hudson, "Pipe flow: a Practical and Comprehensive Guide," New Jersey: John Wiley Sons, 2012.

[20] Munson, B. R., Young, D. F., Okiishi, T. H, "Fundamentals of Fluid Mechanics," Hoboken, NJ: J. Wiley Sons, 2013.

[21] E. S. Menon, "Piping Calculations Manual," New York: McGraw-Hill, 2004.

[22] E. F. Brater, H. W. King, J. E. Lindell, and C. Y. Wei, "Handbook of Hydraulics," New York: McGraw-Hill, 1996.

[23] F. M. White, “Fluid mechanics, 8th edition,” New York: McGraw-Hill, 2016.

[24] P. Ellenberger, “Piping and Pipeline Calculations Manual Second Edition,” Amsterdam: Butterworth-Heinemann, 2014.

[25] R. P. Benedict, “Fundamentals of pipe flow,” New York: Wiley, 1980.

[26] L.F. Moody, “An approximate formula for pipe friction factors,” *Transactions of the ASME*, vol. 69, pp. 1005–1006, 1947.

[27] S.E. Haaland, “Simple and explicit formulas for the friction factor in turbulent pipe flow,” *Transactions of the ASME*, vol. 105, no. 1, pp. 89–90, 1983.

[28] Neutrium, “Pressure loss in pipe,” accessed on 26-3-2021. [Online]. Available: https://neutrium.net/fluid-flow/pressure-loss-in-pipe/

[29] J. Nikuradse, “Strömungsgesetze in rauhen Rohren,” *Forschg. Arb. Ing.-Wes*, no. 361, 1933, in German.

[30] COMSOL Multiphysics, “CFD Module User’s Guide,” 2018, v. 5.4, COMSOL AB, Stockholm, Sweden.

[31] E. S. Menon and P. S. Menon, “Working Guide to Pump and Pumping Stations,” Gulf Professional Publishing, 11 2009.

[32] H. Ito, “Pressure Losses in Smooth Pipe Bends,” *Journal of Basic Engineering*, vol. 82, no. 1, pp. 131–140, 3 1960.

[33] Crane Co., “Flow of fluids through valves, fittings, and pipe, Metric Edition,” New York: Crane Co, 1982.

[34] KSB Group, “Turbine mode,” Accessed on July 15, 2021. [Online]. Available: https://www.ksb.com/centrifugal-pump-lexicon/turbine-mode/328156/

[35] M. van Rooij, “Ocean Battery Efficiëntie,” Ocean Grazer BV, 12 2020.

[36] COMSOL Multiphysics, v. 5.5, COMSOL AB, Stockholm, Sweden. [Online]. Available: www.comsol.com

[37] W. Frei, “Which Turbulence Model Should I Choose for My CFD Application?” 7 2017, COMSOL Blog. [Online]. Available: https://www.comsol.com/blogs/which-turbulence-model-should-choose-cfd-application/

[38] G. Homicz, “Computational Fluid Dynamic Simulations of Pipe Elbow Flow,” 08 2004, sAND2004–3467.

[39] E. Fontes, “Why Should I Use Automatic Wall Treatment for My CFD Modeling?” 6 2017, COMSOL Blog. [Online]. Available: https://www.comsol.com/blogs/why-should-i-use-automatic-wall-treatment-for-my-cfd-modeling/

[40] P. Lyu, “Simulating Turbulent Flow in COMSOL Multiphysics,” 2016, COMSOL Webinar. [Online]. Available: https://www.comsol.com/video/simulating-turbulent-flow-in-comsol-multiphysics

[41] J. Hiller, “What Is A Pressure Point Constraint? When Is It Used?” 10 2019, COMSOL Discussion Forum. [Online]. Available: https://www.comsol.nl/forum/thread/244582/what-is-a-pressure-point-constraint-when-is-it-used

[42] A. Straccia, “How to Assign Fluid Pressure in CFD Simulations,” 12 2016, COMSOL Blog. [Online]. Available: https://www.comsol.com/blogs/how-to-assign-fluid-pressure-in-cfd-simulations/

[43] Gibson, A. H., “On the flow of water through pipes and passages having converging or diverging boundaries,” *Transactions of the Royal Society, London, Series A*, no. 86, pp. 366–378, 3 1910.

[44] N.M. Crawford, G. Cunningham and S.W.T. Spence, “An experimental investigation into the pressure drop for turbulent flow in 90° elbow bends,” *Proceedings of the Institution of Mechanical Engineers, Part E: Journal of Process Mechanical Engineering*, vol. 221, no. 2, pp. 77–88, 2007.

[45] B. T. Petersen, J. M. Gorman, and E. M. Sparrow, “Pressure losses for turbulent flow through bends in series,” *International Journal of Fluid Mechanics Research*, vol. 45, no. 2, pp. 105–128, 2018.

[46] A. Kalpakli Vester, R. Örlü, and P. H. Alfredsson, “Turbulent Flows in Curved Pipes: Recent Advances in Experiments and Simulations,” *Applied Mechanics Reviews*, vol. 68, no. 5, 2016.

[47] K. Sudo, M. Sumida, and H. Hibara, "Experimental investigation on turbulent flow in a circular-sectioned 90-degree bend," *Experiments in Fluids*, vol. 25, pp. 42–49, 1998.

[48] M. Ayala, O. Ayala, and O. Ayala, "Numerical study of the secondary flow formation of a fluid passing through a 90° elbow with square cross section," pp. 1083–1092, 01 2019, 4th Thermal and Fluids Engineering Conference (TFEC).

[49] W.R. Dean, "Note on the Motion of Fluid in a Curved Pipe," *Philosophical Magazine*, vol. 4, no. 20, pp. 208–223, 1927.

[50] S. Sami and J. Cui, "Numerical Study of Pressure Losses in Close Coupled Fittings," *HVAC&R Research*, vol. 10, no. 4, pp. 539–552, 2004.

[51] J. Rahmeyer, "Pressure loss coefficients for close-coupled pipe ells," *ASHRAE Transactions*, vol. 108, no. 1, pp. 390–406, 2002.

[52] Litostroj Power, "Francis Turbine Brochure," 1 2018. [Online]. Available: https://www.litostrojpower.com/files/default/2018-articles/Brochures/Francis_Turbines_Litostroj_Power_Product_Sheet_2018-03-21_Press.pdf

[53] E. Neven, "CFD study on the Ocean Grazer Wave Energy Converter," 6 2021, Master Research Project.

A General Tables

A.1 Physical Properties of Water (SI units)

Table 13: Physical properties of water in SI units. Table adapted from Ref. [20].

Temperature [°C]	Density [kg m^{-3}]	Dynamic viscosity [N s m^{-2}]	Kinematic viscosity [m^2 s^{-1}]
0	999.9	1.787E-03	1.787E-06
5	1000	1.519E-03	1.519E-06
10	999.7	1.307E-03	1.307E-06
20	998.2	1.002E-03	1.004E-06
30	995.7	7.975E-04	8.009E-07
40	992.2	6.529E-04	6.580E-07
50	988.1	5.468E-04	5.534E-07
60	983.2	4.665E-04	4.745E-07
70	977.8	4.042E-04	4.134E-07
80	971.8	3.547E-04	3.650E-07
90	965.3	3.147E-04	3.260E-07
100	958.4	2.818E-04	2.940E-07

A.2 Surface Roughness

Table 14: Surface roughness [mm] for typical pipe materials.

Surface roughness [mm]					
Material	White [23]	King [22]	Menon [21]	Rennels [19]	Comsol [30]
Steel	0.05	0.06-0.01	0.045	0.045	0.05
Cast iron	0.26	N/A	0.26	0.26	0.25
Drawn tubing	0.002	N/A	0.0015	0.0015	0.0015
Concrete, smooth	0.04	0.06	0.3	0.3	0.3
Concrete, rough	2	0.9	3	3	3
Wood, stave	0.5	0.3	0.18-0.9	0.18-0.9	0.5

B Turbulence model simulations

The following tables give an overview of the computation time, wall treatment, pressure and velocity plots and the pressure drop along the center line (pipe axis) and the wall resolution (in viscous units) for four selected turbulence models. These models include the k-ω, realizable k-ϵ, SST and v2-f models, of which information regarding wall treatment and (dis)advantages are tabulated in Table 2.

Table 15: Turbulence model simulations

Turbulence Model	**K-ω**	**Realizable k-ε**
Computation time (min)	27	13
Wall treatment	Wall functions	Wall functions
Pressure plot	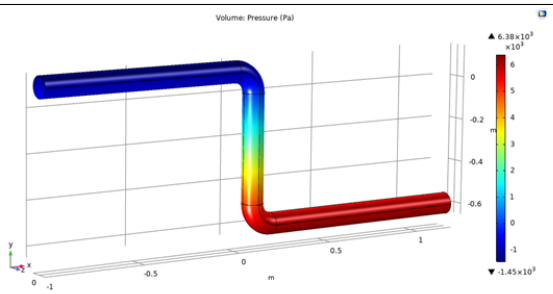	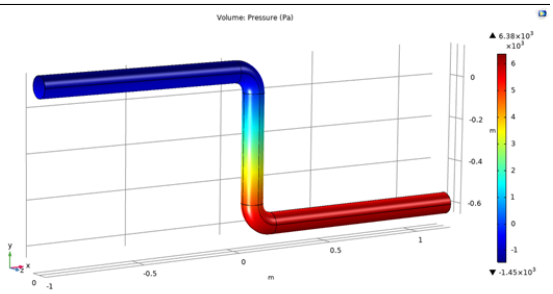
Velocity streamlines	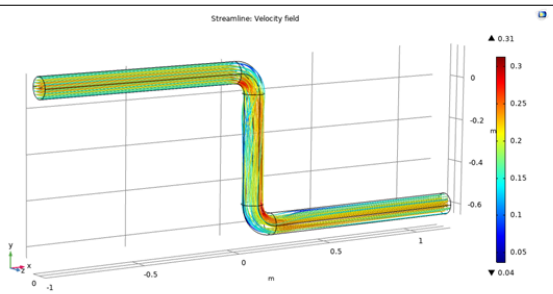	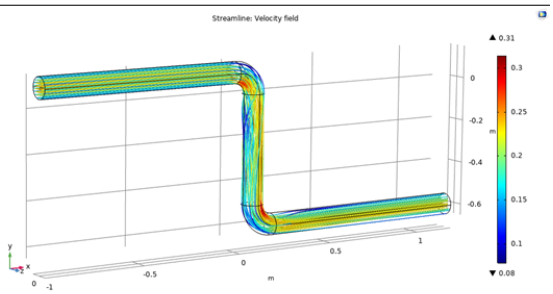
Pressure drop along center line	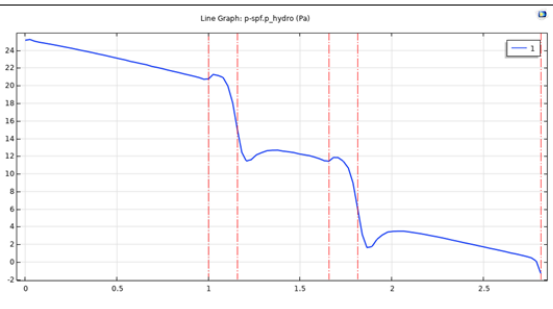	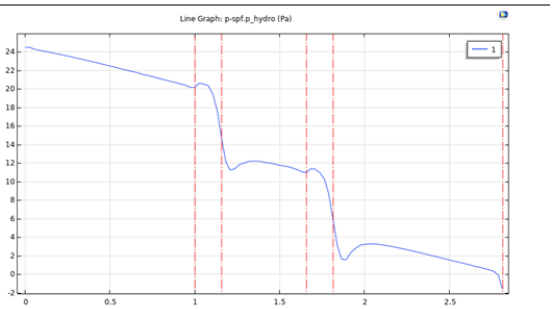
Wall resolution	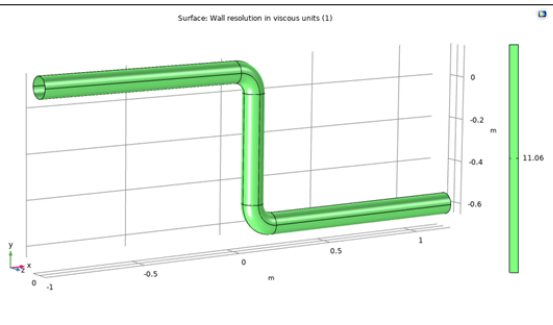	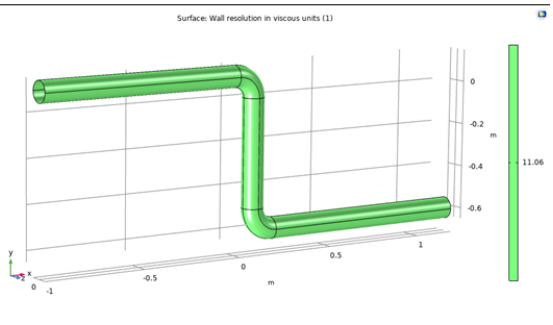

Table 15 continued from previous page

Turbulence Model	SST	v2-f
Computation time (min)	78	44
Wall treatment	Automatic	Automatic
Pressure plot	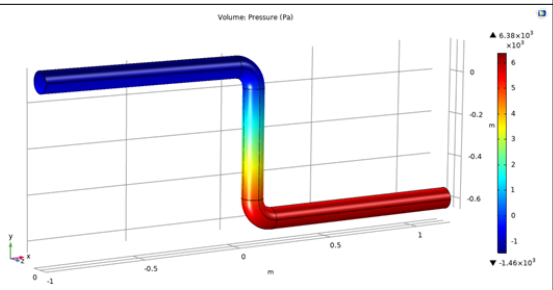	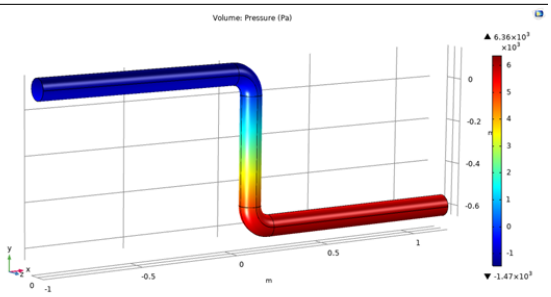
Velocity streamlines	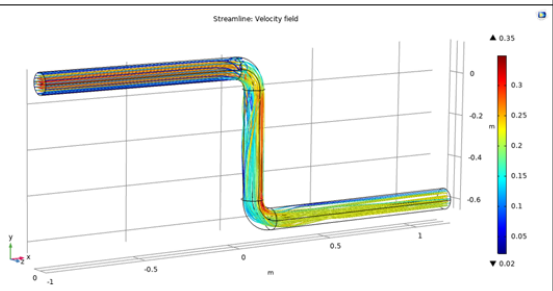	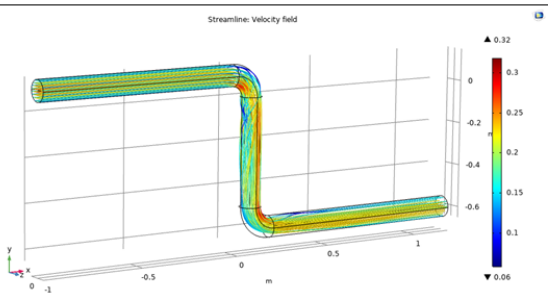
Pressure drop along center line	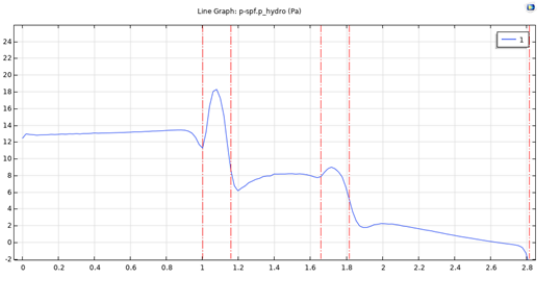	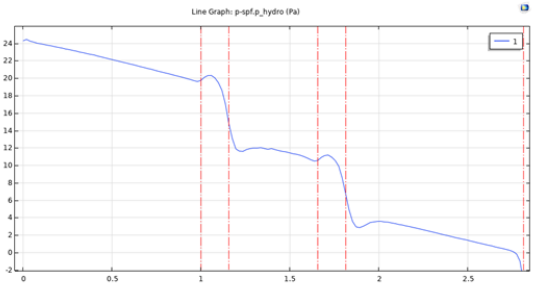
Wall resolution	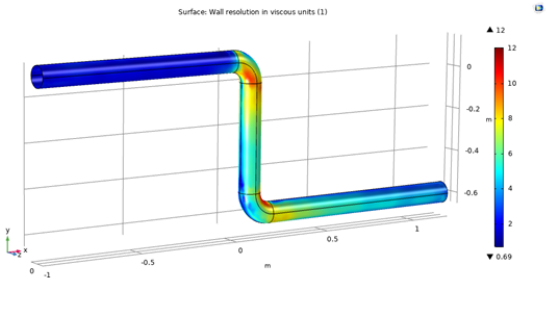	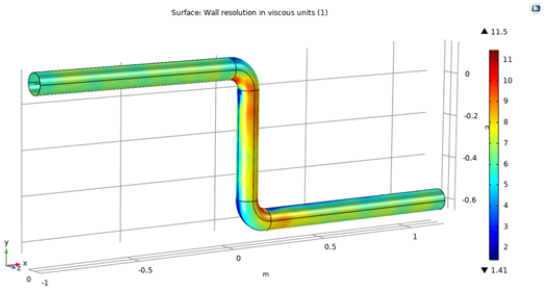

C Simulated Results Comsol

C.1 Single 90° bend

Table 16: Measured pressure and velocity as surface average at planes 1 and 2. The K-value from the Comsol simulations is calculated using Equation 19. The theoretical K-values of Ito [32] and Rennels [19] can be calculated using the equations from Table 1. The Reynolds number is calculated to be 20 000 using Equation 1 and the friction factor f is 0.029, using $\epsilon/d = 0.0005$ and Figure 7.

	Plane A		Plane B			Comsol	Ito	Rennels
R/d	Pressure [Pa]	Velocity [$\mathrm{m\,s^{-1}}$]	Pressure [Pa]	Velocity [$\mathrm{m\,s^{-1}}$]	$P_{decrease}$ [Pa]	K-value	K-value	K-value
1	12.90	0.200	-3.10	0.200	16.00	0.281	0.387	0.448
2	10.04	0.200	-3.90	0.200	13.94	0.177	0.269	0.206
3	10.32	0.200	-3.31	0.200	13.63	0.162	0.265	0.250
4	10.60	0.200	-3.33	0.200	13.93	0.177	0.287	0.294
5	11.24	0.200	-3.22	0.200	14.46	0.203	0.317	0.338
6	12.63	0.200	-3.55	0.200	16.18	0.289	0.351	0.382
8	14.11	0.200	-2.19	0.200	16.30	0.296	0.423	0.470
10	15.16	0.200	-2.39	0.200	17.55	0.359	0.504	0.558
15	16.84	0.200	-2.85	0.200	19.69	0.466	0.727	0.778

C.2 Pipe Enlargement

Table 17: Theoretical K-values for a conical pipe enlargement (diffuser) from 0.2 to 0.4 m for varying cone angles using equations and tables as mentioned under the Gradual Enlargement section in Table 1. The calculations for Rennels and White are done using $Re = 1 \times 10^6$, $\epsilon/d = 0.0002$ and f and $f_{avg} = 0.015$, where Rennels only calculates K up to a maximum cone angle of 20°. The length of the diffuser L, as used by White, can be calculated using trigonometry.

Theoretical K-values				
θ [°]	King [22] & Menon [31]	Menon [21]	Rennels [19]	White [23] & Crane [33]
4	0.04	0.056	0.064	0.051
6	0.04	0.072	0.060	0.077
8	0.05	0.087	0.070	0.102
10	0.07	0.102	0.086	0.127
15	0.16	0.216	0.148	0.191
20	0.29	0.389	0.234	0.254
30	0.46	0.610	N/A	0.379

C.3 Pressure loss analysis

Table 18: Pressure and velocity measurements on the **top** part of the COMSOL model of the buried Ocean Battery. The pressures and velocities in plane 1 are measured at the flexible bladder pipes and the pressures and velocities in plane 2 are measured at the pump-turbine pipes, as shown in Figure 41a.

Average head [m]	Head [m]	Q [$m^3 s^{-1}$]	P_1 [Pa]	V_1 [$m s^{-1}$]	P_2 [Pa]	V_2 [$m s^{-1}$]	H_L [m]	P_L [Pa]	Fractional loss [%]
50	45	3.939	-1.745	0.328	-962.84	1.026	0.050	489.90	0.111
	45	3.347	-1.197	0.279	-695.17	0.871	0.036	353.78	0.080
	55	3.223	-1.096	0.269	-644.61	0.839	0.034	328.06	0.061
	55	2.738	-0.747	0.228	-465.19	0.713	0.024	236.80	0.044
75	70	2.533	-0.621	0.211	-398.13	0.659	0.021	202.69	0.030
	70	2.151	-0.419	0.179	-287.11	0.560	0.015	146.21	0.021
	80	2.216	-0.450	0.185	-304.72	0.577	0.016	155.17	0.020
	80	1.882	-0.302	0.157	-219.83	0.490	0.011	111.99	0.014
100	95	1.866	-0.296	0.156	-216.11	0.486	0.011	110.10	0.012
	95	1.585	-0.197	0.132	-156.02	0.413	0.008	79.56	0.009
	105	1.688	-0.230	0.141	-176.90	0.439	0.009	90.17	0.009
	105	1.434	-0.152	0.120	-127.80	0.373	0.007	65.23	0.006

Table 19: Pressure and velocity measurements on the **bottom** part of the COMSOL model of the buried Ocean Battery. The pressures and velocities in plane 1 are measured at pump-turbine pipes and the pressures and velocities in plane 2 are measured at the rigid reservoir pipes, as shown in Figure 41b.

Average head [m]	Head [m]	Q [$m^3 s^{-1}$]	P_1 [Pa]	V_1 [$m s^{-1}$]	P_2 [Pa]	V_2 [$m s^{-1}$]	H_L [m]	P_L [Pa]	Fractional loss [%]
50	45	3.939	215.5	1.005	-15.37	0.328	0.070	680.98	0.155
	45	3.347	156.6	0.854	-11.12	0.279	0.050	492.62	0.112
	55	3.223	145.4	0.822	-10.32	0.269	0.047	457.01	0.085
	55	2.738	105.6	0.698	-7.46	0.228	0.034	330.47	0.061
75	70	2.533	90.6	0.646	-6.39	0.211	0.029	283.11	0.041
	70	2.151	65.8	0.549	-4.62	0.179	0.021	204.58	0.030
	80	2.216	69.7	0.565	-4.90	0.185	0.022	217.05	0.028
	80	1.882	50.6	0.480	-3.54	0.157	0.016	156.88	0.020
100	95	1.866	49.8	0.476	-3.48	0.156	0.016	154.24	0.017
	95	1.585	36.1	0.404	-2.52	0.132	0.011	111.52	0.012
	105	1.688	40.9	0.431	-2.86	0.141	0.013	126.38	0.012
	105	1.434	29.7	0.366	-2.07	0.120	0.009	91.40	0.009

C.4 Deep water prototype measurement points

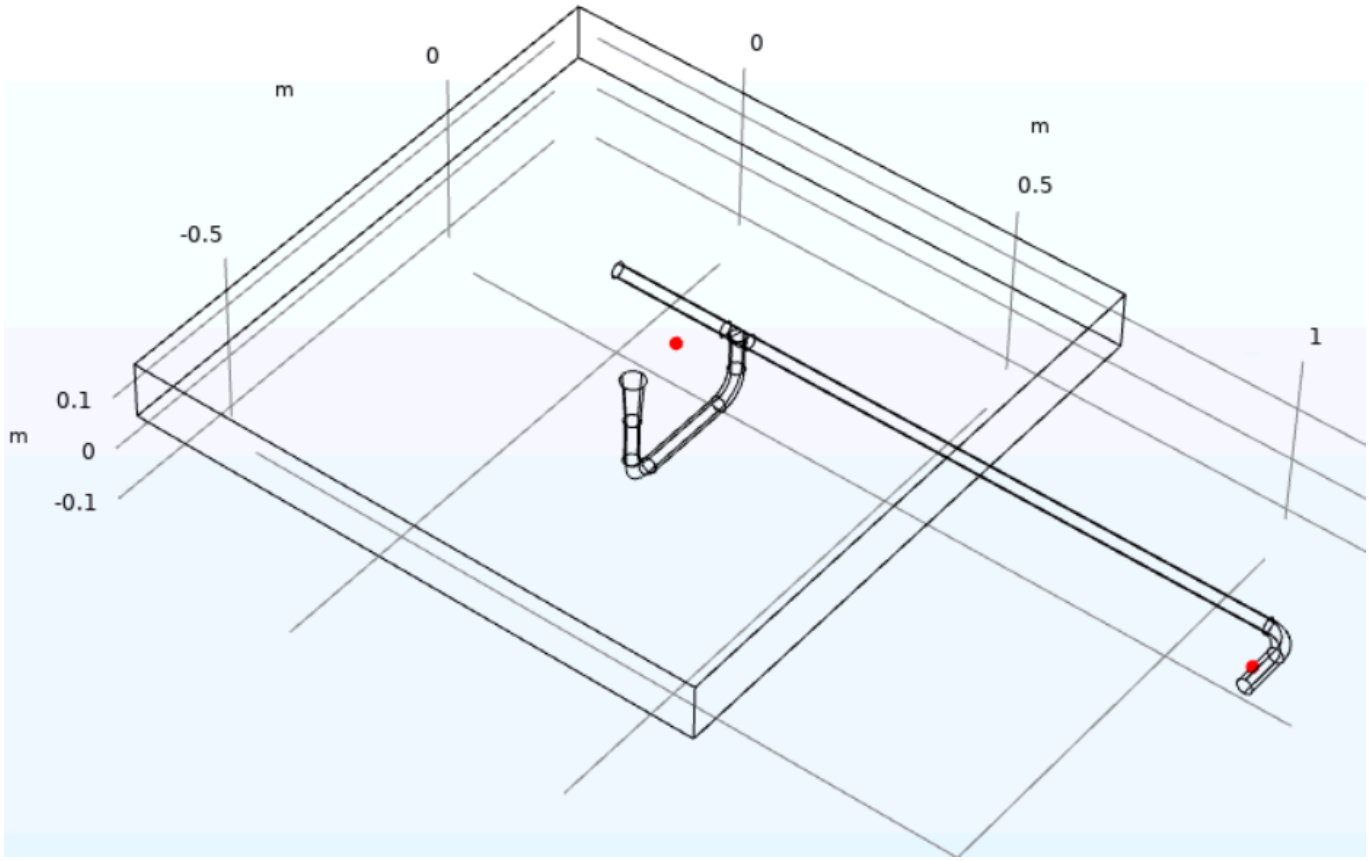

Figure 45: Points in the 3D Comsol model at which the pressure and fluid velocity are measured. These points represent the locations of the sensors in the prototype.

D Experimental data deep water Prototype

Table 20: Partial data set of the experimental measurements with the deep water prototype of the Ocean Battery. T is time of a measurement in [s], Q the flow rate in [$m^3 s^{-1}$], Bl the head on the flexible bladder in [m] and Tu the head on the turbine inlet [m].

T [s]	Q [$m^3 s^{-1}$]	Bl [m]	Tu [m]	T [s]	Q [$m^3 s^{-1}$]	Bl [m]	Tu [m]	T [s]	Q [$m^3 s^{-1}$]	Bl [m]	Tu [m]
0	1.11E-06	3.396	3.339	265	2.96E-04	3.255	3.273	530	2.96E-04	3.281	3.306
5	1.03E-06	3.264	3.364	270	2.96E-04	3.261	3.277	535	2.96E-04	3.295	3.311
10	1.06E-06	3.274	3.356	275	3.03E-04	3.262	3.278	540	2.96E-04	3.277	3.300
15	1.18E-06	3.267	3.346	280	2.96E-04	3.270	3.272	545	3.03E-04	3.282	3.310
20	1.10E-06	3.273	3.355	285	3.03E-04	3.273	3.292	550	2.96E-04	3.275	3.308
25	1.09E-06	3.249	3.343	290	2.96E-04	3.265	3.273	555	2.96E-04	3.266	3.312
30	1.12E-06	3.276	3.357	295	2.96E-04	3.237	3.277	560	2.89E-04	3.287	3.314
35	1.09E-06	3.269	3.342	300	2.96E-04	3.280	3.291	565	2.96E-04	3.280	3.313
40	1.15E-06	3.271	3.350	305	2.96E-04	3.264	3.279	570	2.96E-04	3.306	3.339
45	1.08E-06	3.288	3.355	310	3.03E-04	3.261	3.282	575	2.96E-04	3.274	3.312
50	1.12E-06	3.253	3.341	315	3.03E-04	3.266	3.292	580	2.96E-04	3.284	3.306
55	1.12E-06	3.270	3.366	320	2.96E-04	3.262	3.281	585	2.96E-04	3.268	3.302
60	1.07E-06	3.250	3.349	325	2.96E-04	3.262	3.280	590	2.96E-04	3.293	3.307
65	1.84E-04	3.285	3.277	330	2.96E-04	3.285	3.302	595	2.89E-04	3.269	3.315
70	2.89E-04	3.258	3.266	335	2.96E-04	3.272	3.292	600	2.96E-04	3.262	3.308
75	3.03E-04	3.262	3.263	340	2.96E-04	3.261	3.286	605	2.89E-04	3.275	3.314
80	3.03E-04	3.251	3.270	345	2.89E-04	3.267	3.273	610	2.96E-04	3.302	3.316
85	3.03E-04	3.262	3.261	350	2.96E-04	3.216	3.275	615	2.96E-04	3.282	3.314
90	3.03E-04	3.256	3.277	355	2.89E-04	3.269	3.279	620	2.96E-04	3.276	3.297
95	3.03E-04	3.253	3.256	360	2.89E-04	3.271	3.287	625	3.03E-04	3.270	3.318
100	2.89E-04	3.251	3.266	365	2.89E-04	3.272	3.295	630	2.89E-04	3.272	3.322
105	3.03E-04	3.263	3.263	370	2.96E-04	3.287	3.310	635	2.96E-04	3.275	3.300
110	3.03E-04	3.251	3.250	375	2.96E-04	3.263	3.288	640	2.89E-04	3.302	3.321
115	2.96E-04	3.248	3.263	380	3.03E-04	3.285	3.294	645	2.96E-04	3.285	3.325
120	3.03E-04	3.250	3.258	385	2.96E-04	3.278	3.297	650	2.89E-04	3.274	3.312
125	3.03E-04	3.253	3.270	390	2.96E-04	3.279	3.293	655	2.89E-04	3.269	3.318
130	2.96E-04	3.273	3.280	395	2.96E-04	3.267	3.299	660	2.96E-04	3.290	3.324
135	3.03E-04	3.253	3.263	400	2.96E-04	3.288	3.316	665	2.96E-04	3.276	3.336
140	2.96E-04	3.254	3.279	405	3.03E-04	3.271	3.292	670	1.55E-04	3.292	3.389
145	3.03E-04	3.264	3.284	410	2.96E-04	3.261	3.286	675	1.17E-06	3.290	3.411
150	3.03E-04	3.258	3.267	415	2.96E-04	3.277	3.281	680	1.04E-06	3.266	3.409
155	2.96E-04	3.253	3.288	420	3.03E-04	3.255	3.286	685	1.06E-06	3.273	3.398
160	2.96E-04	3.246	3.274	425	2.96E-04	3.270	3.296	690	1.11E-06	3.294	3.407
165	2.96E-04	3.260	3.264	430	2.89E-04	3.272	3.317	695	1.06E-06	3.271	3.379
170	3.03E-04	3.256	3.259	435	2.96E-04	3.269	3.295	700	1.10E-06	3.297	3.408
175	3.03E-04	3.270	3.296	440	2.96E-04	3.261	3.290	705	1.07E-06	3.270	3.409
180	2.96E-04	3.271	3.284	445	2.96E-04	3.275	3.304	710	1.16E-06	3.295	3.407
185	2.89E-04	3.259	3.274	450	2.96E-04	3.288	3.298	715	1.09E-06	3.281	3.395
190	2.96E-04	3.257	3.275	455	2.89E-04	3.314	3.310	720	1.13E-06	3.283	3.396
195	2.96E-04	3.253	3.267	460	2.96E-04	3.270	3.292	725	1.13E-06	3.262	3.412
200	3.03E-04	3.260	3.265	465	3.03E-04	3.267	3.289	730	1.08E-06	3.275	3.379
205	2.96E-04	3.263	3.269	470	2.89E-04	3.277	3.306	735	1.09E-06	3.272	3.403
210	2.96E-04	3.251	3.271	475	2.96E-04	3.273	3.311	740	1.19E-06	3.275	3.394
215	2.96E-04	3.274	3.290	480	2.96E-04	3.253	3.288	745	1.19E-06	3.270	3.394
220	2.89E-04	3.279	3.281	485	2.89E-04	3.273	3.290	750	1.06E-06	3.265	3.391
225	2.96E-04	3.255	3.275	490	2.89E-04	3.273	3.290	755	1.11E-06	3.285	3.389
230	3.03E-04	3.260	3.275	495	2.89E-04	3.273	3.282	760	1.06E-06	3.292	3.409
235	3.03E-04	3.247	3.265	500	2.96E-04	3.276	3.308	765	1.14E-06	3.273	3.373
240	3.03E-04	3.273	3.294	505	2.89E-04	3.283	3.301	770	1.11E-06	3.274	3.390
245	3.03E-04	3.263	3.283	510	2.96E-04	3.283	3.304	775	1.14E-06	3.277	3.385
250	2.96E-04	3.257	3.283	515	3.03E-04	3.283	3.302	780	1.16E-06	3.271	3.397
255	3.03E-04	3.270	3.280	520	3.03E-04	3.289	3.311	785	1.10E-06	3.209	3.389
260	2.96E-04	3.268	3.271	525	2.96E-04	3.287	3.305	790	1.14E-06	3.284	3.372

The full data set with the prototype measurements can be found in this attachment, which can be opened by opening this thesis in Adobe Acrobat: 

E Matlab model code

An overview of the MATLAB Live Script that is created to calculate and analyse the losses in pipe flow for the buried Ocean Battery is shown on the next pages.

Pipe flow losses in the buried Ocean Battery

In this Matlab Live Script the head loss for a certain set of pipes of the buried Ocean Battery of the Ocean Grazer BV is calculated. First, some general parameters need to be specified within the script. Some additional parameters regarding the length, diameter and roughness of straight pipes and junctions needs to be specified within the InputValues Excel file. Then, the head loss is divided into major loss for straight pipe sections and minor losses for pipe junctions. The output is stored again in a separate tab of the InputValues Excel file.

The model calculates the head loss separately for each pipe section, without taking into consideration the interaction between pipe sections. Also, the model uses the minor loss friction factors, or K-values, from literature but these values can be modified according to preference.

The thesis 'Development and validation of an analytical flow model for the buried Ocean Battery' by W.J. Stegenga provides more information about the flow model, the equations used to calculate the losses and general information about fluid flow in pipe systems.

General parameters

In this section, the general parameters of the system are defined. The depth of the surrounding sea water, the height of the rigid reservoir and the buried depth are defined, as well as the efficiencies of the pump, transformer, motor, turbine and generator. Also the charging or discharging operating mode, including the power of the pump or turbine are defined.

```
Head = 45;                          % Hydrostatic head [m]
Pump_eff = 0.95;                      % Pump efficiency
Trans_eff = 0.99;                     % Transformer efficiency
Motor_eff = 0.98;                     % Motor efficiency
Turb_eff = 0.95;                      % Turbine efficiency
Gen_eff = 0.98;                       % Generator efficiency
T_w = 20;                           % Water temperature [deg Celsius]
g = 9.81;                                       % Gravitational acceleration [m/s^2]
PT = 1;                            % Charging mode (pump active) or discharging mode (turbine active)
N_PT = 8;                          % Number of operational pumps or turbines
Power = 200000;                         % Power of a single pump or turbine (depending on mode) [W]
```

Density of working fluid, dynamic and kinematic viscosity

The density of the working fluid, assumed to be water, and the dynamic and kinematic viscosity are extracted from the WaterTemp Excel file, as these values depend on the temperature of the water. Data from Fundamentals of Fluid Mechanics by Munson et al.

```
WaterTemp = importfileWaterTemp('WaterTemp.xlsx');
rho = WaterTemp{WaterTemp.TemperatureCelsius==T_w,2}; % Density water   [kg/m^3]
mu = WaterTemp{WaterTemp.TemperatureCelsius==T_w,3};  % Dynamic-Viscosity water  [Pa*s]
nu = WaterTemp{WaterTemp.TemperatureCelsius==T_w,4};  % Kinematic-Viscosity water  [m^2/s]
```

Flow rate calculation

The flow rate of the fluid is determined for either the charging mode (pump in operation) or discharging mode (turbine in operation). Also, a manual flow rate can be specified.

```
if PT == 0
    Q = N_PT.*Power.*Pump_eff.*Trans_eff.*Motor_eff./(rho.*g.*Head);  % Pump Flow rate [m^3/s]
else
    Q = N_PT.*Power./(Turb_eff.*Trans_eff.*Gen_eff.*rho.*g.*Head);    % Turbine Flow rate [m^3/s]
end
Q
```

```
Q = 3.9395
```

Major losses

First, the input values from the Excel table are imported, after which the losses are calculated using a for loop. This principle is also used to calculate all other losses. The major losses are tabulated in Table 'Datastraight'.

```
SPtable = importfileSP('InputValues.xlsx', 'StraightPipe');
% Import data for straight pipes from Excel using a function, discard empty entries
D_pipe = table2array(SPtable(:,"D_pipe"));                      % Create arrays for table columns
L_pipe = table2array(SPtable(:,"L_pipe"));
eps_pipe = table2array(SPtable(:,"eps_pipe"));
Datastraight = struct();                                        % Create empty data structure
for i = 1:length(L_pipe)                                        % Calculate major losses for every straight pipe section
    Datastraight(i).D = D_pipe(i);                              % Assign each value to the data structure, diameter pipe [m]
    Datastraight(i).L_pipe = L_pipe(i);                         % Length pipe [m]
    Datastraight(i).eps_pipe = eps_pipe(i);                     % Roughness (epsilon) of pipe material [m]
    Datastraight(i).Q = Q;                                      % Fluid flow rate [m^3/s]
    Datastraight(i).A = 0.25.*pi.*D_pipe(i).^2;                 % Area cross-section pipe [m^2]
    Datastraight(i).v = Q./Datastraight(i).A;                   % Fluid velocity [m/s]
    Datastraight(i).Re = Datastraight(i).v.*Datastraight(i).D./nu;  % Calculation of Reynolds number
    if Datastraight(i).Re < 2000                                % Classification of flow
        Datastraight(i).Region = 'Laminar';
    elseif Datastraight(i).Re > 4000
        Datastraight(i).Region = 'Turbulent';
    else
        Datastraight(i).Region = 'Transition';
    end
    if  strcmp(Datastraight(i).Region,'Laminar')                % Calculate major loss when flow is laminar
        Datastraight(i).flam = 64./(Datastraight(i).Re);        % Laminar friction factor is 64/Re
        Datastraight(i).Maj_loss = Datastraight(i).flam.*(Datastraight(i).L_pipe./Datastraight(i).D).*...
            (Datastraight(i).v.^2)./(2.*g);
        % Head loss [m]
```

```
    else
        Datastraight(i).fturb = Serghide(Datastraight(i).eps_pipe, Datastraight(i).D, Datastraight(i).Re,Datastraight(i).v);
        % Turbulent friction factor from Serghide approximation (separate function file)
        Datastraight(i).Maj_loss = Datastraight(i).fturb.*(Datastraight(i).L_pipe./Datastraight(i).D).*...
            (Datastraight(i).v.^2)./(2.*g);
        % Head loss [m]
    end
end
if i ~= 0
    Total_Major_loss = sum([Datastraight(:).Maj_loss]);             % Total major loss for all straight pipe sections
else
    Total_Major_loss = 0;
end
fprintf('Total Major Loss  = %f m',Total_Major_loss)
```

```
Total Major Loss  = 0.000000 m
```

```
for i = 1:length(L_pipe)
    Datastraight(i).Perc = (Datastraight(i).Maj_loss./Total_Major_loss)*100;
    % Contribution of each straight pipe section to total major loss
end
```

Minor losses

Bends

The results are tabulated in Table 'Databend'.

```
Bendtable = importfileBends('InputValues.xlsx', 'Bends');       % Import data for bends from Excel file
Ang = table2array(Bendtable(:,"Ang"));                          % Bend angle in degrees
R_D = table2array(Bendtable(:,"R_D"));                          % Radius over diameter of bend
D_bend = table2array(Bendtable(:,"D_bend"));                    % Diameter pipe bend
Databend = struct();                                            % Create empty data structure
for ij = 1:length(R_D)                                          % Calculate minor losses for every bend
    Databend(ij).D_bend = D_bend(ij);                           % Assign each value to the data structure
    Databend(ij).R_D = R_D(ij);
    Databend(ij).Ang = Ang(ij);
    Databend(ij).Q = Q;
    Databend(ij).A = 0.25.*pi.*D_bend(ij).^2;
    Databend(ij).v = Q./Databend(ij).A;
    Databend(ij).check = Databend(ij).v<14;
    Databend(ij).Re = Databend(ij).v.*Databend(ij).D_bend./nu;
    if Databend(ij).Re < 2000                                   % Classification of flow
        Databend(ij).Region = 'Laminar';
    elseif Databend(ij).Re > 4000
        Databend(ij).Region = 'Turbulent';
    else
        Databend(ij).Region = 'Transition';
    end
    Databend(ij).Min_loss = BendLoss(Databend(ij).Ang, Databend(ij).R_D,Databend(ij).Re).*(Databend(ij).v.^2)/(2.*g);
    % Head loss [m] from bends based on functions by Ito (separate function file)
end
if ij ~= 0
    Total_Bend_loss = sum([Databend(:).Min_loss]);              % Total minor loss for all bends
else
    Total_Bend_loss = 0;                                        % If there are no bends, bend loss is zero
end
fprintf('Total Bend Loss  = %f m',Total_Bend_loss)
```

```
Total Bend Loss  = 0.000000 m
```

```
for ij = 1:length(R_D)
    Databend(ij).Perc = (Databend(ij).Min_loss./Total_Bend_loss)*100;    % Contribution of each bend to total minor loss
end
```

Inlets and exits

The results are tabulated in Table 'DataIO'.

```
DataIO = importfileIO('InputValues.xlsx', 'InletOutlet');    % Import data for inlets/exits from input Excel file
```

Rounded entrances

```
RO = struct();
RO.RD = [0.03, 0.03];                       % Specify the radius over diameter value of each rounded entrance
RO.D = [1, 1];                              % Specify the pipe diameter connected to each rounded entrance
if DataIO.Amount(5) == 0
    RO.H = 0;
elseif DataIO.Amount(5) ~= 0
    for ik = 1:DataIO.Amount(5)
    if length(RO.RD) ~= DataIO.Amount(5)
       disp('Number of elements in RO_RD should equal amount of rounded entrances')
        DataIO.K_val(5) = NaN;
    elseif length(RO.D) ~= DataIO.Amount(5)
       disp('Number of elements in RO_D should equal amount of rounded entrances')
        DataIO.K_val(5) = NaN;
    end
    RO.lambda(ik) = 1+0.622.*(1-0.3.*sqrt(RO.RD(ik)) - 0.7.*RO.RD(ik)).^4;              % Equation 31 from thesis
```

```
    RO.K(ik) = 0.0696.*(1-0.569.*RO.RD(ik)).*(RO.lambda(ik).^2)+(RO.lambda(ik)-1).^2;   % Equation 32 from thesis
    RO.v(ik) = Q./(0.25.*pi.*RO.D(ik).^2); % Velocity in inlet
    RO.H(ik) = RO.K(ik).*(RO.v(ik).^2)./(2.*g);
    end
end
```

Remaining inlets and exits

```
DataIO.H_loss = zeros(5,1);
DataIO.H_loss(1) = (DataIO.K(1)*(DataIO.Amount(1))).*((Q./(0.25.*pi.*DataIO.D_IO(1).^2)).^2)./(2.*g);
DataIO.H_loss(2) = (DataIO.K(2)*(DataIO.Amount(2))).*((Q./(0.25.*pi.*DataIO.D_IO(2).^2)).^2)./(2.*g);
DataIO.H_loss(3) = (DataIO.K(3)*(DataIO.Amount(3))).*((Q./(0.25.*pi.*DataIO.D_IO(3).^2)).^2)./(2.*g);
DataIO.H_loss(4) = (DataIO.K(4)*DataIO.Amount(4)).*((Q./(0.25.*pi.*DataIO.D_IO(4).^2)).^2)./(2.*g);
DataIO.H_loss(5) = sum(RO.H);

Total_IO_loss = sum([DataIO.H_loss]);  % Total minor loss for all inlet and outlets [m]
fprintf('Total Input/Output Loss  = %f m',Total_IO_loss)
```

```
Total Input/Output Loss  = 0.000000 m
```

```
for ik = 1:length(DataIO.H_loss)
    DataIO.Perc(ik) = (DataIO.H_loss(ik)./Total_IO_loss)*100;    % Contribution of each inlet/exit to total minor loss
end
```

Enlargements

The results are tabulated in Table 'DataEnl'.

Sudden Enlargements

```
SudEnltable = importfileSudEnl('InputValues.xlsx', 'Enlargement');  % Import data for sudden enlargements from Excel file
D_1_Sud_Enl = table2array(SudEnltable(:,"D1"));                     % Diameter of smaller pipe
D_2_Sud_Enl = table2array(SudEnltable(:,"D2"));                     % Diameter of larger pipe
DataEnl = struct();                                        % Create empty data structure
if length(D_1_Sud_Enl) == 0                                %#ok<ISMT>
    il = 0;
else
    for il = 1:length(D_1_Sud_Enl)                             % Calculate minor losses for every sudden enlargement
    DataEnl(il).D_1 = D_1_Sud_Enl(il);
    DataEnl(il).D_2 = D_2_Sud_Enl(il);
    DataEnl(il).Q = Q;
    DataEnl(il).Sud_Grad = 'Sudden';                       % Label it as a sudden enlargement
    DataEnl(il).A = 0.25.*pi.*DataEnl(il).D_1.^2;
    DataEnl(il).v1 = DataEnl(il).Q./DataEnl(il).A;
    DataEnl(il).CA = 90;
    DataEnl(il).Min_loss = ((1-(DataEnl(il).D_1./DataEnl(il).D_2).^2).^2).*(DataEnl(il).v1.^2)/(2.*g);  % Equation 33 from thesis
    end
end
```

Gradual Enlargements

```
GradEnltable = importfileGradEnl('InputValues.xlsx', 'Enlargement');    % Import data for gradual enlargements from Excel file
D_1_Grad_Enl = table2array(GradEnltable(:,"D3"));                       % Diameter of smaller pipe
D_2_Grad_Enl= table2array(GradEnltable(:,"D4"));                        % Diameter of larger pipe
Eps_enl = table2array(GradEnltable(:,"Eps_enl"));
CA_grad_Enl = table2array(GradEnltable(:,"ConeAngle"));
if length(D_1_Grad_Enl) == 0                                %#ok<ISMT>
    im = 0;
else
    for im = 1:length(D_1_Grad_Enl)                             % Calculate minor losses for every gradual enlargement
    DataEnl(im+il).D_1 = D_1_Grad_Enl(im);                  % Put data of gradual enlargement below sudden enlargement in structure
    DataEnl(im+il).D_2 = D_2_Grad_Enl(im);
    DataEnl(im+il).Q = Q;
    DataEnl(im+il).Sud_Grad = 'Gradual';                        % Label it as a gradual enlargement
    DataEnl(im+il).A = 0.25.*pi.*DataEnl(im+il).D_1.^2;
    DataEnl(im+il).v1 = DataEnl(im+il).Q./DataEnl(im+il).A;
    DataEnl(im+il).CA = CA_grad_Enl(im);
    DataEnl(im+il).Min_loss = ((8.30.*(tand(DataEnl(im+il).CA./2)).^(1.75)).*((1-(DataEnl(im+il).D_1./DataEnl(im+il).D_2).^2).^2)...
        +((Serghide(Eps_enl(im),DataEnl(im+il).D_1,(DataEnl(im+il).v1.*DataEnl(im+il).D_1./nu),DataEnl(im+il).v1)).*...
        (1-(DataEnl(im+il).D_1./DataEnl(im+il).D_2).^4)/(8.*sind(DataEnl(im+il).CA./2)))).*...
        (DataEnl(im+il).v1.^2)/(2.*g);                          % Equation 34 from thesis
    end
end

if il ~= 0 || im ~= 0
    Total_Enl_loss = sum([DataEnl(:).Min_loss]); % Total minor loss for all enlargements
else
    Total_Enl_loss = 0;
end
fprintf('Total Enlargement Loss  = %f m',Total_Enl_loss)
```

```
Total Enlargement Loss  = 0.000000 m
```

```
for ip_e = 1:(im+il)
    DataEnl(ip_e).Perc = (DataEnl(ip_e).Min_loss./Total_Enl_loss)*100;    % Contribution of each enlargement to total minor loss
end
```

Contractions

The results are tabulated in Table 'DataCon'.

Sudden Contractions

```
SudContable = importfileSudCon('InputValues.xlsx', 'Contraction');  % Import data for sudden contractions from Excel file
D_1_Sud_Con = table2array(SudContable(:,"D1"));                     % Diameter of smaller pipe
D_2_Sud_Con = table2array(SudContable(:,"D2"));                     % Diameter of larger pipe
DataCon = struct();                                                 % Create empty data structure
if length(D_1_Sud_Con) == 0                                    %#ok<ISMT>
    in = 0;
else
    for in = 1:length(D_1_Sud_Con)                                      % Calculate minor losses for every contraction
    DataCon(in).D_2 = D_2_Sud_Con(in);
    DataCon(in).D_1 = D_1_Sud_Con(in);
    DataCon(in).Q = Q;
    DataCon(in).Sud_Grad = 'Sudden';                                    % Label it as a sudden contraction
    DataCon(in).A = 0.25.*pi.*DataCon(in).D_1.^2;                       % Area of smaller pipe D1
    DataCon(in).v1 = DataCon(in).Q./DataCon(in).A;                      % Velocity in smaller pipe
    DataCon(in).CA = 90;                                                % Cone angle is 90 deg for sudden contractions
    DataCon(in).beta = (DataCon(in).D_1./DataCon(in).D_2);
    DataCon(in).lambda = 1+0.622.*(1-(0.215.*DataCon(in).beta.^2)-0.785.*(DataCon(in).beta.^5)); % Equation 36 from thesis
    DataCon(in).Min_loss = ((0.0696.*(1-DataCon(in).beta.^5)).*...
        (DataCon(in).lambda.^2)+((DataCon(in).lambda-1).^2)).*(DataCon(in).v1.^2)/(2.*g); % Equation 35 from thesis
    end
end
```

Gradual Contractions

```
GradContable = importfileGradCon('InputValues.xlsx', 'Contraction');    % Import data for gradual contractions from Excel file
D_1_Grad_Con = table2array(GradContable(:,"D4"));                       % Diameter of smaller pipe
D_2_Grad_Con = table2array(GradContable(:,"D3"));                       % Diameter of larger pipe
CA_grad_Con = table2array(GradContable(:,"ConeAngle"));
if length(D_1_Grad_Con) == 0                                     %#ok<ISMT>
    io = 0;
else
    for io = 1:length(D_1_Grad_Con)                                         % Calculate minor losses for every gradual contraction
    DataCon(io+in).D_2 = D_2_Grad_Con(io);
    DataCon(io+in).D_1 = D_1_Grad_Con(io);
    DataCon(io+in).Q = Q;
    DataCon(io+in).Sud_Grad = 'Gradual';                                % Label it as a gradual contraction
    DataCon(io+in).A = 0.25.*pi.*DataCon(io+in).D_1.^2;                 % Area of smaller pipe D1
    DataCon(io+in).v1 = DataCon(io+in).Q./DataCon(io).A;
    DataCon(io+in).CA = CA_grad_Con(io);
    DataCon(io+in).beta = (DataCon(io+in).D_1./DataCon(io+in).D_2);
    DataCon(io+in).lambda = 1+0.622.*(sind(DataCon(io+in).CA./180).^(4/5)).*(1-(0.215.*DataCon(io+in).beta.^2)-0.785.*...
        (DataCon(io+in).beta.^5)); % Equation 38 from thesis
    DataCon(io+in).Min_loss = ((0.0696.*sind(DataCon(io+in).CA./2).*(1-DataCon(io+in).beta.^5)).*...
        (DataCon(io+in).lambda.^2)+((DataCon(io+in).lambda-1).^2)).*(DataCon(io+in).v1.^2)/(2.*g); % Equation 37 from thesis
    end
end
if in ~= 0 || io ~= 0
    Total_Con_loss = sum([DataCon(:).Min_loss]);  % Total minor loss for all contractions
else
    Total_Con_loss = 0;
end
fprintf('Total Contraction Loss  = %f m',Total_Con_loss)
```

```
Total Contraction Loss  = 0.037802 m
```

```
for ip_c = 1:(io+in)
    DataCon(ip_c).Perc = (DataCon(ip_c).Min_loss./Total_Con_loss)*100;    % Contribution of each bend to total minor loss
end
```

Total head loss in pipe system

The results are tabulated in Table 'DataTotal', in which the fractional loss of the total head loss is shown for each loss type. A more in-depth analysis can be found in the corresponding tables for each loss type.

```
Total_Head_loss = Total_Major_loss + Total_Bend_loss + Total_IO_loss + Total_Enl_loss + Total_Con_loss;
% Sum of all contributions to head loss
fprintf('Total Head Loss  = %f m',Total_Head_loss)
```

```
Total Head Loss  = 0.037802 m
```

```
loss_type = {'Major loss'; 'Bend loss'; 'Input/output loss'; 'Enlargement loss'; 'Contraction loss'; 'Total loss'};
loss_value = [Total_Major_loss; Total_Bend_loss; Total_IO_loss; Total_Enl_loss; Total_Con_loss; Total_Head_loss];
fraction = 100*[Total_Major_loss./Total_Head_loss; Total_Bend_loss./Total_Head_loss; Total_IO_loss./Total_Head_loss;
    Total_Enl_loss./Total_Head_loss; Total_Con_loss./Total_Head_loss; 1];
DataTotal = table(loss_type,loss_value,fraction);
filename = 'InputValues.xlsx';  % Write to InputValues Excel file
writetable(DataTotal,filename,'Sheet','Output') % Write results to sheet. if error: check if file is open > close it
```